UNIVERSITY OF OKLAHOMA

GRADUATE COLLEGE

IMPROVING HIGH-RESOLUTION TROPICAL CYCLONE PREDICTION USING A CYCLED, GSI-BASED HYBRID ENSEMBLE-VARIATIONAL DATA ASSIMILATION SYSTEM FOR HWRF WITH VORTEX SCALE OBSERVATIONS

A DISSERTATION

SUBMITTED TO THE GRADUATE FACULTY

in partial fulfillment of the requirements for the

Degree of

DOCTOR OF PHILOSOPHY

By

XU LU

Norman, Oklahoma

2019

IMPROVING HIGH-RESOLUTION TROPICAL CYCLONE PREDICTION USING A CYCLED, GSI-BASED HYBRID ENSEMBLE-VARIATIONAL DATA ASSIMILATION SYSTEM FOR HWRF WITH VORTEX SCALE OBSERVATIONS

A DISSERTATION APPROVED FOR THE

SCHOOL OF METEOROLOGY

BY THE COMMITTEE CONSISTING OF

Dr. Xuguang Wang, Chair

Dr. Prakash Vedula

Dr. Michael Biggerstaff

Dr. Naoko Sakaeda

Dr. Louis Wicker

Acknowledgements

First and foremost, I'm greatly grateful for the guidance of my advisor, Dr. Xuguang Wang. Her expertise and patience have placed me in a position to successfully achieve my research goals. I am also appreciative for my committee members – Drs. Michael Biggerstaff, Naoko Sakaeda, Louis Wicker, and Prakash Vedula – for their support. Special thanks to the help from my friends and also the members or ex-members of the Multiscale data Assimilation and Prediction (MAP) lab: Yongzuo Li, Yongming Wang, Bo Huang, Sam Degelia, and Hristo Chipilski. Thanks also goes to the collaborators from Environmental Modeling Center (EMC), Developmental Testbed Center (DTC), Tropical Cyclone Intensity Experiment (TCI) and Hurricane Intensity Forecasting Experiment (IFEX). I would like to acknowledge for the support from the projects provided by the National Oceanic and Atmospheric Administration (NOAA) Hurricane Forecast Intensity Program (HFIP) and the Office of Naval Research (ONR) TCI. The dissertation was supported by the project grants NA12NWS4680012, NA14NWS4830008, NA14NWS4680021, NA16NWS4680028, N000141410125, and N000141712111. The experiments were performed on the supercomputers Jet from NOAA and Schooner from the University of Oklahoma.

On a more personal note, I would like to thank the support, tolerance and scarifies from my wonderful wife Ting. And of course, special thanks to my dear baby daughter Zoey, who brings me lots of joys besides her occasionally wake-up-and-cuddle-me-or-I-cry in the middle of the night. I would like to thank my parents, Guangshun and Min, for their endless love and support. Without the support and encouragement from these dear family members, the research would not have been possible.

Table of Contents

Acknowledgements iv

List of Tables vii

List of Figures viii

Abstract xiii

Chapter 1: Introduction and overview 1
1.1 Background and motivation 1
1.2 Overview of the dissertation 6

Chapter 2: Methodologies and System Description 8
2.1 Overview of the GSI-based, continuously cycled, dual-resolution hybrid ensemble-variational (EnVar) DA system for HWRF 8
2.2 GSI based dual-resolution hybrid EnVar 10
2.3 EnKF 11
2.4 Directed moving nest strategy 12
2.5 Integrating vortex relocation (VR) and modification (VM) with DA 14

Chapter 3: GSI-Based, Continuously Cycled, Dual-Resolution Hybrid Ensemble–Variational Data Assimilation System for HWRF: Experiments with Edouard (2014) 16
3.1 Introduction 16
3.2 Experiment Design 21
3.2.1 HWRF model configuration 21
3.2.2 Experiment setup 22
3.3 Results 26
3.3.1 Impact of incorporating the higher resolution control analysis through dual-resolution DA 26
3.3.2 Impact of vortex initialization (VI) and ensemble relocation 31
3.3.3 Impacts of 4DEnVar for vortex scale observation assimilation 34
3.3.4 Investigation of intensity forecast improvement over the operational HWRF 39
3.4 Summary and Conclusion 43

Chapter 4: What is Missing to Capture the Rapid Intensification of Hurricane Patricia (2015) when HWRF is already Initialized with a More Realistic Analysis? 47
4.1 Introduction 47
4.2 Methodology, Data and Experiment Design 53
4.2.1 System Description 53
4.2.2 HWRF Model Configuration 55
4.2.3 Experiment Design 57
4.3 Why more persistent TC spin-down exists with the more realistic analyses produced by DA? 60
4.3.1 Differences between VM and DA on TC analyses and forecasts 60

4.3.2 Why did more persistent spin-down occur with a more realistic DA analysis? 66
4.4 Can Modified Model Physics Alleviate the spin-down issue? 75
4.4.1 Impacts of model physics parameterization modifications on TC analyses and intensity forecasts 75
4.4.2 How can the modified model physics parameterizations alleviate spin-down? 78
4.5 How does model resolution impact on the TC intensity forecast? 79
4.6 Summary and Discussions 81

Chapter 5: Observation Impacts on the Analysis and Prediction of Patricia (2015) 85
5.1 Introduction 85
5.2 Model, Data and Experiment Design 89
5.2.1 Model description 89
5.2.2 Observations and preprocessing 91
5.2.3 Experiment Design 93
5.3 Results 95
5.3.1 Evolution of Patricia observed from various platforms 95
5.3.2 Analysis and forecast from NoDA 105
5.3.3 Impact of the operational HWRF observations 108
5.3.4 Impacts of CIMSS AMV observations 112
5.3.5 Impact of SFMR observations 113
5.3.6 Impact of FL observations 115
5.3.7 Impacts of TDR observations 116
5.3.8 Impact of HDSS dropsonde observations 119
5.3.9 Impacts of all observations 121
5.4 Summary and Discussion 123

Chapter 6: Summary and Future Plans 126
6.1 General Summary 126
6.2 Future Plans 128

References 130

List of Tables

Table 3.1 List of experiments and their descriptions. 22

Table 3.2 List of observations assimilated in each domain. 23

Table 3.3 Percentage of absolute vorticity variance explained by each wavenumber averaged over 1.5 RMW radius during the intensifying period from 1200 UTC 13 September 2014 to 0600 UTC 15 September 2014. 43

Table 4.1 List of experiments and their descriptions. 56

Table 5.1 List of experiments and their descriptions. 89

Table 5.2 Correlation coefficients calculated against the 3D HRD radar composite for the 24-hour forecasted storm structure from each experiment. 111

List of Figures

Figure 2.1 Flow chart of GSI based EnKF-Variational hybrid data assimilation system for HWRF (adapted from Wang et al. 2013). 8

Figure 2.2 Sea-level pressure field at (a) +00:00, (b) +03:00, (c) +06:00 for the original HWRF moving strategy (dashed contour with thin box) and the directed moving strategy (solid contour with thick box) for ensemble member #1 (red & orange) and #2 (blue & cyan). Note that large areas of solid and dashed contours are overlain and indistinguishable due to the almost identical forecast fields. 13

Figure 3.1 Domain configuration example for hurricane Edouard. 22

Figure 3.2 Wind (shading and vectors) and pressure (contours) at 1km height for (a) HRD radar wind composite, (b) 3DEV analysis, (c) 3DEV-9kmS analysis, (d) 3DEV-NVRM analysis, and (e) 3DEV-NEVR analysis for the second TDR mission valid at 1800 UTC 15 September 2014. Black dot is the best track position from NHC. Red line denotes the corresponding cross-sections to be presented in Figure 3.3. 27

Figure 3.3 Wind speed (shading), potential temperature (black contours) and relative humidity (white contours) analysis of the south to north vertical section for (a) HRD radar wind analysis, (b) 3DEV, (c) 3DEV-9kmS, (d) 3DEV-NVRM, and (e) 3DEV-NEVR for the second TDR mission valid at 1800 UTC 15 September 2014. The values in Fig. 5b-e are the spatial correlation coefficients between the analyzed three-dimensional wind speed field and the HRD radar wind composite. 28

Figure 3.4 (a) Mean absolute track forecast error, (b) mean absolute RMW forecast error, (c) mean absolute MSLP forecast error and (d) mean absolute 10m Vmax forecast error for 32 missions of Edouard 2014 for 3DEV (turquoise), 3DEV-9kmS (green), 3DEV-NVRM (yellow) and 3DEV-NEVR (purple). The corresponding MSLP and Vmax forecast error bias, or mean error, are also given in (e) and (f). The green, yellow and purple histograms below (a), (b), (c) and (d) are the bootstrap significance levels where 3DEV is statistically different from 3DEV-9kmS (A: "3DEV" minus B: "3DEV-9kmS"), 3DEV-NVRM (A: "3DEV" minus B: "3DEV-NVRM") and 3DEV-NEVR (A: "3DEV" minus B: "3DEV-NEVR"), respectively. The black histograms denote the bootstrap significance levels where 3DEV-NEVR is statistically different from 3DEV-NVRM (A: "3DEV-NEVR" minus B: "3DEV-NVRM"). The significance levels of 80% (solid) and 20% (dotted) for each pair are given as red lines in the histograms to indicate where A is significantly better or worse than B, respectively. The significance levels between 20% and 80% indicate that there is no statistically significant difference between A and B. The significance level of 50% is also shown with red dashed lines to indicate if A is better (>50%) or worse (<50%) than B. The numbers in the brackets under x-axis are the number of cases at each lead time. 30

Figure 3.5 Horizontal plots of (a~c) wind (shading and vectors) and pressure (contours) at 1km height as well as west to east cross-sections of (d~f) wind speed (shading), potential temperature

(black contours) and relative humidity (white contours) for the HRD radar wind composite (first column), 3DEV (second column), and 4DEVTR (third column) for the fourth TDR-involved cycle valid at 1200 UTC 17 September 2014. The west to east vertical cross-sections in (d~f) are denoted by the corresponding red lines in (a~c). The blue line in (a~c) denotes the flight track when TDR data was available between 1258-1417 UTC, and the turquoise line in (a) denotes the flight track when TDR data is available between 1617-1708 UTC. Due to the data distribution, the HRD radar composite is valid at 1500 UTC 17 September 2014. 35

Figure 3.6 As in Figure 3.4 but for 3DEV (turquoise), 4DEVTR (blue) and the operational HWRF (red). The orange histograms below (a), (b), (c) and (d) are the bootstrap significance levels where 3DEV is statistically different from the operational HWRF (A: "3DEV" minus B: "Oper.HWRF"). The red and blue histograms denote the bootstrap significance levels where 4DEVTR is statistically different from the operational HWRF (A: "4DEVTR" minus B: "Oper.HWRF") and 3DEV (A: "4DEVTR" minus B: "3DEV"). 38

Figure 3.7 (a) MSLP and (b) Vmax forecasts for all missions during Edouard for the operational HWRF (red), 4DEVTR (blue) and best track (black). The dashed lines denote the forecasts initialized from each DA cycle and the solid lines denote the multi-forecast average valid at the same time. The (c) MSLP and (d) Vmax forecast error bias during the intensifying period (Vmax change > 20kt $24h^{-1}$) between 1200 UTC 13 September 2014 to 0600 UTC 15 September 2014 are given. The (e), (g) MSLP and (f), (h) Vmax forecast for 10th cycle at 0000 UTC (third row) and 11th cycle at 0600 UTC (fourth row) 14 September 2014 are also given. 40

Figure 3.8 Mean azimuth mean inertial stability (shading; $\boldsymbol{10^{-6}s^{-2}}$), radial wind (purple contours; dashed for inflow, solid for outflow; $\boldsymbol{ms^{-1}}$) and tangential wind (black contours; $\boldsymbol{ms^{-1}}$) averaged over intensifying period (8 cycles in total from 1200 UTC 13 September 2014 to 0600 UTC 15 September 2014) for 4DEVTR (first row) and the Operational HWRF (second row) and valid at 00h (first column), 06h (second column), and 12h (third column). 42

Figure 4.1 An example of the normalized vertical diffusivity profile for the original HWRF (blue) and modified turbulent mixing (red) PBL parameterization scheme. These profiles are for the eyewall. 52

Figure 4.2 Flowchart of the GSI-based EnVar hybrid DA system for HWRF [adapted and upgraded from Fig. 2.1]. VI is a combination of VM and VR. 54

Figure 4.3 (a)~(f) Wind (shading and vectors, ms^{-1}) and pressure (contours, hPa) at 10-m height for (a) SFMR observations, (b) NoDA analysis, (c) VM analysis, (d) DA analysis, (e) DA-HD analysis and (f) DA-HDVD analysis for the third TCI mission valid at 1800 UTC, 22 Oct 2015. The black dot is the best track position from NHC. (g)~(l) is the corresponding wind (shading and vectors) at 3-km height for (g) HRD radar composite, (h) NoDA analysis, (i) VM analysis, (j) DA analysis, (k) DA-HD analysis and (l) DA-HDVD analysis. Note, the SFMR and HRD radar composite are centered around 1739 UTC, 22 Oct 2015. There are no wind vectors in (a) SFMR observations and there are no pressure contours in both (a) SFMR and (g) TDR observations. 61

Figure 4.4 Radius-height cross-section of the isopleths of the azimuthal mean NRF (m s^{-1} s^{-1}) for (a), (d) NoDA, (b), (e) VM and (c), (f) DA analysis at 1800 UTC 22 Oct 2015. (a)~(c) is a zoom-in plot for (d)~(f) below 700 hPa and within 90 km radii. The sum of Centrifugal Force and Coriolis Force (m s^{-1} s^{-1}) at 1-km height are also given for (g) NoDA, (h) VM, (i) DA, and (j) HRD radar composite. 63

Figure 4.5 (a) 10-m Vmax forecast, (b) MSLP forecast, (c) track forecast and (d) track forecast error for NoDA (dotted navy), VM (dashed blue), DA (solid cyan) and best track (solid black) during Patricia initialized from 1800 UTC 22 Oct 2015. The numbers in (c) indicates the corresponding forecast lead time for each track forecast..... 65

Figure 4.6 2-hour evolution of (a) 10-m Vmax, (b) MSLP and (c) NMASPT for NoDA (black), VM (green), DA (cyan) and DA-HDVD (red) initialized from 1800 UTC 22 Oct 2015. The output are plotted every 2 minutes..... 67

Figure 4.7 Time evolution of the azimuthal mean radial wind (shading, m s^{-1}) and secondary circulation (vectors, m s^{-1}) for (a)~(e) NoDA-warm, (f)~(j) NoDA, (k)~(o) VM, (p)~(t) DA and (u)~(y) DA-HDVD for the (a), (f), (k), (p), (u) initial analysis; (b), (g), (l), (q), (v) 2-min forecast; (c), (h), (m), (r), (w) 4-min forecast; (d), (i), (n), (s), (x) 30-min forecast; and (e), (j), (o), (t), (y) 60-min forecast. Red arrows are added to illustrate the evolution of secondary circulations..... 68

Figure 4.8 Radius-time Hovmoller plots of the 500 hPa azimuthal mean vertical velocity (shading, m s^{-1}) and 900 hPa tangential wind (contour, m s^{-1}, 4 m s^{-1} interval) for (a) NoDA-warm, (b) NoDA, (c) VM, (d) DA and (e) DA-HDVD for the first 6 hours. The RMW from the best track is given as solid black line..... 70

Figure 4.9 Same as Fig. 4.7 except the shading for azimuthal mean total condensate (kg kg^{-1}) for (a)~(e) NoDA, (f)~(j) VM, (k)~(o) DA and (p)~(t) DA-HDVD for the (a), (f), (k), (p) initial analysis; (b), (g), (l), (q) 2-min forecast; (c), (h), (m), (r) 4-min forecast; (d), (i), (n), (s) 30-min forecast; and (e), (j), (o), (t) 60-min forecast. 73

Figure 4.10 Same as Fig. 4.5 except for DA (cyan), DA-HD (purple), DA-HDVD (red) and best track (black). 77

Figure 4.11 Same as Fig. 4.5 except for DA (solid cyan), DA-Hi (dashed blue), DA-HDVD (solid red), DA-HDVDHi (dashed orange) and best track (solid black). 81

Figure 5.1 An example of the (a) Temporal, (b) horizontal and (c) vertical distribution of the observations. (b) and (c) are the wind observations assimilated in the innermost domain valid at 1800 UTC 22 Oct 2015 during Patricia. Best is short for the best track data form NHC. Note, the x-axis in Fig. 5.1c is in log space..... 86

Figure 5.2 Wind (shading and vectors, m s-1) and pressure (contours, hPa) at 10-m height for (a) SFMR observations onboard NOAA P-3 aircraft centered around 1739 UTC 22 Oct 2015, (b) NoDA analysis, (c) OperH analysis, (d) CIMSS_Only analysis, (e) SFMR_Only analysis, (f) FL_Only analysis, (g) TDR_Only analysis, (h) HDSS_Only analysis and (i) All analysis valid at

1800 UTC 22 Oct 2015 during Patricia. The black dots denote the best track position valid at 1800 UTC 22 Oct 2015. 97

Figure 5.3 Same as Fig. 5.2 except for the 3-km horizontal wind (shading and vectors, m s^{-1}) in verification with (a) the HRD radar composite. The blue lines in (a) denote the flight track of WB-57 and the blue lines in (b)~(i) denote corresponding southeast to northwest cross-section to be plotted in Fig. 5.4 and Fig. 5.6. 98

Figure 5.4 Same as Fig. 5.2 except for the Radial wind (shading, m s-1) analysis of the southeast to northwest vertical section in verification with (a) the HDSS dropsonde observations centered around 1820 UTC 22 October 2015. Positive (warm color) indicates outflow and negative (cold color) indicates inflow. 99

Figure 5.5 Same as Fig. 5.2 except for 150 hPa radial wind (shading, m s-1) and horizontal wind (vectors, m s-1) in verification with (a) the CIMSS AMV observations. The red star in (a) and the black dots in (b)~(i) denote the best track position and the blue dots in (b)~(i) denote the analyzed storm center at the surface. Note, the black and blue dots are very close to each other for each experiment due to the vortex relocation. 100

Figure 5.6 Same as Fig. 5.4 except for the warm-core anomaly analysis of the southeast to northwest vertical section in verification with (a) the HDSS dropsonde observations centered around 1820 UTC 22 October 2015. The Jordan annual mean profile is used as the environmental sounding for all experiments for consistency. 101

Figure 5.7 Same as Fig. 5.2 except for the 4-hour forecasted brightness temperature (K) in verification with (a) GOES-13 band 4 valid at 2200 UTC 22 Oct 2015 during Patricia. The red dots denote the satellite-derived storm position at this time. 102

Figure 5.8 Same as Fig. 5.6 except for the 8-hour forecasted brightness temperature (K) valid at 0200 UTC 23 Oct 2015 during Patricia. 103

Figure 5.9 Same as Fig. 5.2 except for the 24-hour forecasted surface wind (shading and vectors, m s^{-1}) valid at 1800 UTC 23 Oct 2015 in verification with (a) HIRAD (Hurricane Imaging Radiometer) observations centered at 2000 UTC 23 Oct 2015 during Patricia. The domain size is the same in (a)-(i). The black dots denote the best track position at 1800 UTC 23 Oct 2015. 104

Figure 5.10 Same as Fig. 5.2 except for the 24-hour forecasted 3-km wind (shading and vectors, m s^{-1}) in verification with (a) HRD radar composite valid at 1733 UTC 23 Oct 2015 during Patricia. The black dots denote the best track position valid at 1800 UTC 23 Oct 2015. 105

Figure 5.11 (a), (e), (i) MSLP forecast, (b), (f), (j) Vmax forecast, (c), (g), (k) track forecast and (d), (h), (l) track forecast errors for NoDA (blue), OperH (green), CIMSS_Only (yellow), SFMR_Only (purple), FL_Only (red), TDR_Only (orange), HDSS_Only (gold), All (cyan) and best track (black) initialized from 1800 UTC 22 Oct 2015 during Patricia. 107

Figure 5.12 The co-located 150 hPa radial wind increment (shading, m s^{-1}) by subtracting NoDA from (a) OperH analysis, (b) CIMSS_Only analysis, (c) SFMR_Only analysis, (d) FL_Only

analysis, (e) TDR_Only analysis, (f) HDSS_Only analysis and (g) All analysis valid at 1800 UTC 22 Oct 2015 during Patricia. The vectors are the 150 hPa horizontal wind from NoDA as a reference. 109

Figure 5.13 Root-Mean-Square-Fit (RMSF) of different types of observation verifications for each experiment. The colors denote the percentage of RMSF changes relative to NoDA for the independent verifications. The warmer the colors, the larger the relative RMSF. 110

Abstract

A Gridpoint Statistical Interpolation analysis system (GSI)-based, continuously cycled, dual-resolution hybrid ensemble-variational (EnVar) data assimilation (DA) system is developed for the Hurricane Weather Research and Forecasting (HWRF) Model. The newly developed DA system is then used in this dissertation to address a few scientific and technical challenges in assimilating the vortex-scale observations to improve the numerical prediction of TCs.

In the dissertation, the newly developed DA system is described first. Then, the next part addresses how various data assimilation configurations impact the vortex scale observation assimilation and the subsequent prediction using the DA system. It is found that (1) dual-resolution EnVar DA improves the analyzed storm structure and short-term maximum wind speed (Vmax) and minimum sea level pressure (MSLP) forecasts compared to coarser, single-resolution EnVar DA, but track and radius of maximum wind (RMW) forecasts do not improve. (2) Additionally, applying vortex relocation (VR) and vortex modification (VM) on the control background before DA improves the analyzed storm, overall track, RMW, MSLP, and Vmax forecasts. Further applying VR on the ensemble background improves the analyzed storm and forecast biases for MSLP and Vmax. (3) Also, using four-dimensional (4D) EnVar to assimilate tail Doppler radar (TDR) data improves the analyzed storm and short-term MSLP and Vmax forecasts compared to three-dimensional (3D) EnVar although 4DEnVar slightly degrades the track forecast. (4) Finally, a diagnostic on why advanced DA can improve the TC intensity forecast for Edouard (2014) is provided.

In the third part, using the further upgraded DA system, the deficiency of the numerical model physics was discussed. Although the DA produces realistic 3D analyses to initialize the model, persistent Vmax spin-down is found during the rapid intensification of hurricane Patricia

(2015). Diagnostics reveal that the spin-down issue is likely attributed to the deficient HWRF model physics which are unable to maintain the realistic 3D structures from the DA analysis. The horizontal diffusion is too strong to maintain the realistically observed vertical oscillation of radial wind near the eyewall region. The vertical diffusion profile cannot produce a sufficiently strong secondary circulation connecting the realistically elevated upper-level outflow produced in the DA analysis. Further investigations with different model physics parameterizations demonstrate that spin-down can be alleviated by modifying model physics. In particular, a modified turbulent mixing parameterization scheme together with a reduced horizontal diffusion is found to significantly alleviate the spin-down issue and to improve the intensity forecast. Additional experiments show that the peak simulated intensity and rapid intensification (RI) rate can be further improved by increasing the model resolution. But the model resolution is not as important as model physics in the spin-down alleviation.

The last part of the dissertation explores the relative impact of various vortex scale observations on the analysis and prediction of hurricane Patricia (2015). In comparing the impacts of assimilating each dataset individually, results suggest that: (1) The assimilation of 3D observations produces better TC structure analysis than the assimilation of two-dimensional (2D) observations; (2) The analysis from assimilating observations collected from platforms that only sample momentum fields produces a less improved forecast with either short-lived impacts or slower intensity spin-up as compared to the forecast produced after assimilating observations collected from platforms that sample both momentum and thermal fields; (3) The structure forecast tends to benefit more from the assimilation of inner-core observations than the corresponding intensity forecast, which implies better verification metrics are needed for future TC forecast evaluation.

Chapter 1: Introduction and overview

Multiple portions of this dissertation are direct excerpts of Lu et al. (2017; © Royal Meteorological Society), Lu et al. (2017; © American Meteorological Society) and Lu and Wang (2019; © American Meteorological Society). This includes parts of Chapters 1, 2, 3, 4 and 5.

1.1 Background and motivation

The tropical cyclones (TCs), usually originated from the warm tropical oceans, spend most of their lifetime in the open ocean. But when TCs move toward or even around the continent, they can be devastating to the corresponding coastal areas (Pielke et al. 2008). It is thus crucial to have an accurate prediction of the track and strength of these potential hazards. According to the error statistics from the National Hurricane Center (NHC), the track forecast of TCs has been greatly improved as compared to that 20 years ago (Zhang and Weng 2015). Compared to the track forecast improvement, the improvements in the intensity forecast of TCs are much smaller over the decades (Rogers et al. 2006, 2013a). Such a discrepancy between the track and intensity forecast improvements is not surprising: TC tracks are largely affected by the large-scale environmental flows, which can be better analyzed from the improving global models (Zhang and Weng 2015); In comparison to the track, the intensity variation of TCs is largely governed by the inner-core processes. Although satellites provide a great number of observations over the ocean, our utilization of satellite observations in the inner-core regions is still immature due to the contaminations of heavy precipitation (Bauer et al. 2010, 2011; Yang et al. 2016; Zhang et al. 2016; Zhu et al. 2018; Geer et al. 2017, 2018; Wu et al. 2019). The challenges in the application of satellite observations restrict our options for inner-core observations to the sporadically sampled airborne-based in-situ observations when the TCs are away from continents. These

finite in-situ inner-core observations are limited in the temporal and spatial coverage, and therefore limit our understanding of the inner-core processes. Consequently, TC intensity prediction of the Numerical Weather Prediction (NWP) systems becomes difficult without sufficiently accurate inner-core initial conditions and model physics. Hence, to improve the TC intensity prediction, (1) a better data assimilation (DA) system to utilize the existing data, (2) model physics parameterizations or schemes that are more consistent with the reality and (3) more in-situ observations sampling the inner-core regions are needed.

Since 2005, the Intensity Forecasting Experiment (IFEX) program from the National Oceanic and Atmospheric Administration (NOAA) has deployed the WP-3D aircraft to collect various kinds of in-situ inner-core observations by penetrating hurricanes (Rogers et al. 2006, 2013a). For instance, the Stepped Frequency Microwave Radiometer (SFMR), flight-level (FL) and tail doppler radar (TDR) observations were all collected onboard the NOAA WP-3D aircraft during the field program. These types of observations provided valuable information to improve our understanding of the structure evolution of hurricanes (Marks and Houze 1984, 1987; Reasor et al. 2000; Willoughby and Rahn 2004; Rogers and Uhlhorn 2008a; Powell et al. 2009; Chen et al. 2011; Rogers et al. 2013b). More recently, more and more flights were deployed to penetrate or circle around the TCs by different field campaigns. Such as the WB-57 aircraft from the Tropical Cyclone Intensity (TCI) program supported by the Office of Naval Research (ONR) (Doyle et al. 2017), and the unmanned-aircraft Global Hawk from the Hurricane and Severe Storm Sentinel (HS3) program supported by the National Aeronautics and Space Administration's (NASA) (Braun et al. 2016). These relatively new field programs utilized more advanced techniques and instruments, like the High-Definition Sounding System (HDSS; Black et al. 2017) dropsondes and the Hurricane Imaging Radiometer (HIRAD; Black et al. 2017), to

sample the inner-core or near-inner-core-environment information of TCs. With the increasing vortex-scale TC observations available, how to make good use of these existing data becomes important.

Early studies have demonstrated the promise of using ensemble covariances for vortex-scale data assimilation (DA) in TC predictions. In these studies, the ensemble covariances were adopted either through the use of the ensemble Kalman filter (EnKF, e.g., Zhang et al. 2009a; Aksoy et al. 2012; Weng and Zhang 2012; Poterjoy and Zhang 2014a,b; Poterjoy et al. 2014) or the ensemble-variational (EnVar) method (Li et al. 2012; Wang and Lei 2014; Li 2015; Lu et al. 2017a). It was found that such ensemble-based covariances during DA can improve the TC track and intensity forecasts due to the superior analyses of the TC environment (Poterjoy and Zhang 2014b; Zhang and Weng 2015), TC vortex and inner-core structures (Li et al. 2012; Weng and Zhang 2012; Lu et al. 2017a).

In the United States' operational Hurricane Weather Research and Forecasting (HWRF) modeling and prediction system, a Gridpoint Statistical Interpolation (GSI) based hybrid three-dimensional (3D) EnVar DA method was adopted since 2013. Using this operational HWRF DA system, the assimilation of high-resolution inner-core observations was found to improve the overall track and intensity forecast of TCs (Tong et al. 2018). However, Tong et al. (2018) also showed that the improvement in the intensity forecast was primarily at later lead-times and for the weak storms. The short-term intensity forecast, especially in strong storms, was often degraded due to a spin-down issue. Tong et al. (2018) suggested that the spin-down, a short-term but significant Vmax decrease after HWRF initialization, is likely related to the deficiencies in the model and DA configurations. For example, the operational HWRF uses the ensemble covariance from the Global Forecast System (GFS) during the 3DEnVar DA. But our early

study (Lu et al. 2017a) showed that a HWRF self-consistent ensemble should be used instead of the global ensemble to improve the TC analysis and intensity predictions for the assimilation of vortex-scale observations.

Therefore, in this dissertation, a new GSI-based hybrid EnVar DA system for HWRF is developed to investigate the optimal way to digest vortex-scale observations. The new DA system is developed with multiple capabilities to perform end-to-end, continuous DA and forecast cycles for the entire life of a TC. The details about this DA system and the corresponding methodologies will be documented in Chapter 2.

Based on but more advanced than the operational HWRF, the newly developed DA system aims at addressing a few scientific and technical challenges in assimilating the vortex-scale observations to improve the numerical prediction of TCs. For example, (1) the dual-resolution DA is a popular method to maintain the benefit of high-resolution background at convection-allowing model resolution, while reducing computational cost by running the ensemble at a coarser resolution (Gao and Xue 2008; Buehner et al. 2010; Hamill et al. 2011; Clayton et al. 2013; Kuhl et al. 2013; Schwartz 2016). However, such a method has not been examined for the convection-allowing model resolution in the hurricane predictions; (2) Studies have suggested that the vortex initialization (VI) method prior to DA used by the operational HWRF (Liu et al. 2000, 2006; Tallapragada et al. 2015) can be unnecessary when having the advanced inner-core DA (Torn and Hakim 2009a; Xiao et al. 2009; Zhang et al. 2009b, 2011; Li et al. 2012; Weng and Zhang 2012; Aksoy et al. 2013; Schwartz et al. 2013; Lu et al. 2017a). Nevertheless, it is unknown how the VI should be integrated with DA in a continuously cycled DA system when the inner-core observations are only irregularly available; And (3) TCs can be fast-evolving, especially during the rapid intensification or eyewall replacement processes. Therefore, the

three-dimensional (3D) EnVar DA may not be enough to properly update the state at the analysis time in such scenarios (Wang and Lei 2014). These scientific challenges then trigger the investigations on the optimal DA and system configurations to assimilate the vortex-scale inner-core observations in Chapter 3. With some of the results presented in this dissertation (e.g. the self-cycled background error covariances to be discussed in Chapter 3), the new system has been partially implemented into the operational HWRF since 2017 (Tong et al. 2018).

The spin-down has been a well-known issue for the HWRF model for almost a decade (Bernardet et al. 2015; Zhou et al. 2015a,b; Pu et al. 2016; Tong et al. 2018). Some early studies attributed the issue to the unrealistic initial analysis (Bernardet et al. 2015; Zhou et al. 2015b; Pu et al. 2016), and some other studies associated the issue with the insufficient model physics (Vukicevic et al. 2013; Tong et al. 2018). Nevertheless, these studies were based on a DA and system configuration similar or equivalent to the operational HWRF. Hence, the unrealistic initial conditions can be a result of lacking efficient DA configuration and may complicate the factors for the spin-down issue. Therefore, it is worthy of further investigations on the issue with a more realistic initial analysis produced through our advanced DA system. It will be shown in Chapter 4.3 that the spin-down is more likely to be related to the model physics deficiencies given a realistic DA analysis. Then, Chapter 4.4 and Chapter 4.5 explores how can we improve the TC intensity prediction by improving the model physics and model resolution, respectively.

Although there are increasing numbers of types of in-situ inner-core observations sampled by various field campaigns, the chance for the co-existence of multiple datasets from different field campaigns is rare. Thus, even with early studies focusing on some of the datasets individually or in small sub-sets (Weng and Zhang 2012; Aksoy et al. 2012, 2013; Poterjoy et al. 2014; Wu et al., 2014, 2015; Lu et al. 2017a), we are lacking a thorough understanding of the

relative importance for each type of observations. During Hurricane Patricia in 2015, the coordination between IFEX and TCI field campaigns provides an unprecedented chance to sample the same storm with a great number of independent instruments simultaneously and intensively (Doyle et al. 2017). Such a scarce case allows us to utilize the advanced DA system to explore the relative impacts of various types of observations on the analysis and forecast of a same hurricane in Chapter 5. Instead of drawing statistically robust conclusions from the investigation with only one case study, the goal of Chapter 5 in this dissertation is to provide a reference for future observation sampling strategies and follow-on DA studies.

1.2 Overview of the dissertation

This dissertation first describes the newly developed HWRF DA system and related methodologies in Chapter 2. Using the advanced HWRF DA system, the optimal way to utilize the vortex-scale observations to improve TC intensity predictions is studied in the rest of this dissertation. Specifically, the following three scientific questions are addressed: (i) Would using a more advance data assimilation system to assimilate vortex-scale observations help improve the TC analysis and intensity prediction? (ii) Is a realistic DA analysis produced by the advanced DA system sufficient to improve TC intensity prediction? And (iii) What's the relative impact of various in-situ vortex-scale observations on TC prediction?

A detailed study with Hurricane Edouard (2014) to investigate the optimal DA configuration is documented first in Chapter 3. As part of the investigation, detailed diagnostics are also performed in this chapter to explore the potential of this newly developed DA system to improve the intensity prediction of TCs over the operational HWRF by comparing the TC analysis and forecast. Next in Chapter 4, the dissertation investigates the reason why a more realistic DA analysis cannot produce an improved intensity forecast over the more unrealistic Vortex

Modification (VM) analysis during Hurricane Patricia (2015). A hypothesis about the incompatibility between the realistic DA and unrealistic model physics has been proposed, and experiments with improved model physics are conducted in this chapter to support the hypothesis. Additionally, experiments with model resolution changes are also conducted to explore the impact of model resolution in the intensification and peak intensity prediction of TCs. Finally, Chapter 5 explores the relative impacts of various vortex-scale observations on the analysis and prediction of Patricia. A general summary and future plans are given in Chapter 6.

Chapter 2: Methodologies and System Description

2.1 Overview of the GSI-based, continuously cycled, dual-resolution hybrid ensemble-variational (EnVar) DA system for HWRF

Following the early development in Lu et al. (2017a), a GSI-based hybrid EnKF-Var DA system for HWRF is further developed in this study to integrate with VI and to include the continuously cycling, dual-resolution 3DEnVar and 4DEnVar capabilities. Figure 2.1 shows an example of the flow chart of the newly developed system, and a detailed description follows below.

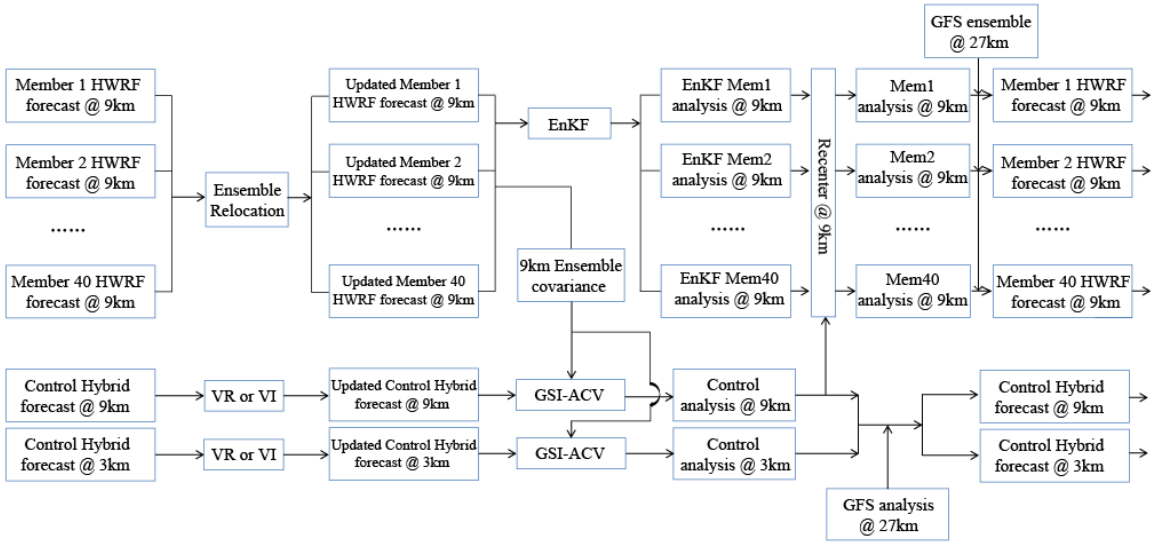

Figure 2.1 Flow chart of GSI based EnKF-Variational hybrid data assimilation system for HWRF (adapted from Wang et al. 2013).

For the first cycle of a storm, a 40-member HWRF ensemble is initialized by the ensemble analyses from the National Centers for Environmental Prediction (NCEP) operational GFS hybrid DA system (Wang et al. 2013). In the meantime, a single deterministic HWRF spin-up forecast is initialized by the control analysis from the same GFS system. Using the Tropical Cyclone Vitals (TCVital) database and following Liu et al. (2000, 2006), vortices in the 6-hour

ensemble forecast are relocated, while vortices in the control forecast valid at 3, 6 and 9 hours are both relocated and modified before meeting the requirement of First Guess at Appropriate Time (FGAT[1]; see Trahan and Sparling 2012). The modified control forecast is then used as the control background for EnVar DA on 3- and 9-km grids, while the relocated ensemble forecast is used as the background ensemble for the EnKF on the 9-km grid and for EnVar DA on both the 3- and 9-km grids. Further details regarding VR and VM procedures are discussed in Section 2.5. During the continuously cycled ensemble and control background forecasts, a newly developed directed moving nest strategy is adopted. A detailed description of the directed moving nest strategy will be discussed in Section 2.4.

At the DA and state update stage, four steps are involved. First, the 40-member relocated HWRF background forecast is updated by the EnKF to produce a 40-member analysis on the 9-km domain. Next, the control analysis on the 3- and 9-km domains is produced with GSI EnVar DA using the 40-member relocated HWRF ensemble and the augmented control vector (ACV) method in GSI variational minimization (GSI-ACV; Wang et al. 2013). Since the assimilation window is 6 hours, FGAT is applied for the EnVar DA. Then the EnKF analysis on the 9-km domain is then re-centered around the 9-km EnVar analysis (i.e., the EnKF mean is replaced with the EnVar analysis). Finally, the 27-km HWRF outermost domain is replaced by the GFS control and ensemble analyses without undergoing DA. The DA is not performed on the outermost domain following the operational HWRF, a configuration chosen due to limited benefits from using a regional analysis instead of the global analysis for the large-scale TC environment (Tallapragada et al. 2014).

[1] First Guess at Appropriate Time (FGAT) interpolates the background forecast to the observation time so that the observation priors in the innovation corresponds to the "appropriate" observation time. To perform the FGAT interpolation, background forecasts at 3, 6 and 9 h are used for a 6-hour DA time window centered at 6 h.

After the analyses are produced from the above four steps, the background forecasts are produced to prepare for the next DA cycle. In particular, the EnVar analysis is used to initialize a 9-hour short-term deterministic forecast on the 27/9/3-km grid, and a 6-hour 40-member ensemble background forecasts on the 27/9-km grids is initialized from the re-centered HWRF EnKF analysis. The same directed moving nest strategy, VR and VM procedures as applied for the spin-up background forecasts are then adopted before applying the next DA steps. This cycling of DA and forecasts continues through the end of the storm.

Finally, to evaluate various DA methods, a single deterministic 120-h free forecast is initialized by the EnVar analysis for each DA cycle. This forecast is independent of the 9-h control forecast that uses directed moving nests and instead employs HWRF's original vortex following strategy.

2.2 GSI based dual-resolution hybrid EnVar

This section describes the general dual-resolution 4DEnVar form implemented in the GSI. Similar notations for dual-resolution EnVar can be found in Schwartz et al. (2015), Kleist and Ide (2015a,b), and Schwartz (2016). The description of the hybrid 4DEnVar formula mirrors those in Wang (2010) and Wang and Lei (2014). The analysis increment $\mathbf{x}'_t$ at time *t* within a DA window for the dual-resolution hybrid 4DEnVar is defined as:

$$\boldsymbol{x}'_t = \boldsymbol{x}'_1 + \boldsymbol{D}\sum_{k=1}^{K}(\boldsymbol{a}_k \circ (\boldsymbol{x}^e_k)_t), \tag{2.1}$$

where $\mathbf{x}'_1$ denotes the increment from the GSI static covariance, **D** denotes the operator that maps the fields from the coarser ensemble grids to the finer control grids, $\mathbf{a}_k$ denotes the augmented control vectors for the kth ensemble member, $(\boldsymbol{x}^e_k)_t$ denotes the kth ensemble perturbation at time *t* normalized by $(\mathrm{K}-1)^{1/2}$, K is the ensemble size, and the symbol ° denotes the Schur product.

The cost function remains the same as in single-resolution hybrid 4DEnVar (Wang and Lei 2014):

$$J(\boldsymbol{x}_1', \boldsymbol{a}) = \frac{1}{2}\beta_1(\boldsymbol{x}_1')^T \boldsymbol{B}_1^{-1}(\boldsymbol{x}_1') + \frac{1}{2}\beta_2(\boldsymbol{a})^T \boldsymbol{A}^{-1}(\boldsymbol{a}) + \frac{1}{2}\sum_{t=1}^{L}(\boldsymbol{y}_t^{o\prime} - \boldsymbol{H}_t\boldsymbol{x}_t')^T \boldsymbol{R}_t^{-1}(\boldsymbol{y}_t^{o\prime} - \boldsymbol{H}_t\boldsymbol{x}_t') \quad (2.2)$$

where $\mathbf{B}_1$ denotes the static covariance, **a** is a vector that concatenates $\mathbf{a}_k$, k=1, K, **A** denotes the matrix that defines the localization applied to the ensemble covariance, L is the length of the DA window, and $\boldsymbol{R}_t$, $\boldsymbol{y}_t^{o\prime}$ and $\mathbf{H}_t$ refer to the observation error covariance, innovation vector and linearized observation operator valid at time period *t*, respectively. β_1 and β_2 are the weights assigned for the static and ensemble covariance, respectively, where $\frac{1}{\beta_1} + \frac{1}{\beta_2} = 1$ (Wang et al. 2008ab).

The major difference between dual-resolution and single-resolution hybrid 4DEnVar is the incorporation of the operator **D**, which allows the coarser resolution ensemble to be projected to the finer control background. In other words, dual-resolution 4DEnVar formula returns to the single-resolution formula when the operator **D** is an identity matrix. Additionally, since the 4DEnVar is a temporal extension of 3DEnVar (Wang and Lei 2014), equations (2.1) and (2.2) become dual-resolution 3DEnVar if a single time *t* is considered in the DA window.

2.3 EnKF

As mentioned in the previous Section 2.2, the GSI-based hybrid EnVar DA system for HWRF includes the HWRF EnKF component to provide ensemble background covariance during the continuous DA cycling. Following Lu et al. (2017a), the EnKF component adopts the ensemble square root filter (EnSRF; Whitaker and Hamill 2002). As described in Lu et al. (2017a), this EnKF code has been interfaced with HWRF and uses the observation pre-processing, quality control and forward operators provided by GSI. The cutoff radius for the

covariance localization adopted by the EnKF is similar to that used by the EnVar component. Additionally, the Relaxation To Prior Spread (RTPS) multiplicative inflation algorithm developed by Whitaker and Hamill (2012) is adopted.

2.4 Directed moving nest strategy

As stated in Section 2.1, a directed moving nest strategy is developed and applied to produce the first guess forecasts during the DA cycling. The primary objective of this development is to solve the issue associated with non-overlapped ensemble domains for storm-following moving nests without needing DA code changes. In the traditional storm following moving nest, the center of the nest for each ensemble member will follow the center of its own simulated TC. At the end of the first guess simulations, the ensemble nest locations diverge, which introduces complications for ensemble-based DA. In the new moving nest strategy, rather than letting the center of the domain follow its own simulated storm, the center of the domains for both the ensemble and the control background are moved to the same prescribed locations during model integration by adding a piece of code to the HWRF model. This moving nest strategy has flexibility to determine the prescribed locations as well as the flexibility to prescribe a specific time period to move during the first guess forecast. For example, in order to implement FGAT or 4DEnVar from hours 3 to 9, the domains can move for the first 3 hours and stay in the same position during the remaining 6 hours of model integration. This directed moving nest strategy is simple to implement without requiring changes in the DA code.

As described earlier, this newly developed directed moving nest strategy has the flexibility to choose the source of the prescribed locations. The prescribed locations determine the movement of the directed domains. Therefore, it is important to explore the sensitivity of this new directed moving nest strategy to the different sources of the prescribed locations. Additional experiments

have been conducted with 3h prescribed locations produced from interpolating and extrapolating TCVital, GFS forecasts, and blending the GFS forecast with extrapolated TCVitals. The locations produced by these methods are similar except for slight differences at the early stage of Edouard when the storm is relatively weak and disorganized (not shown). Given the limited differences in the prescribed locations from different sources, sensitivity experiments showed they also produce reasonably similar DA and forecast results with the different prescribed positions (not shown). This study uses interpolated TCVital for illustration, though extrapolated TCVital, 3h global forecast or the combination of the two can all be applied in operational settings.

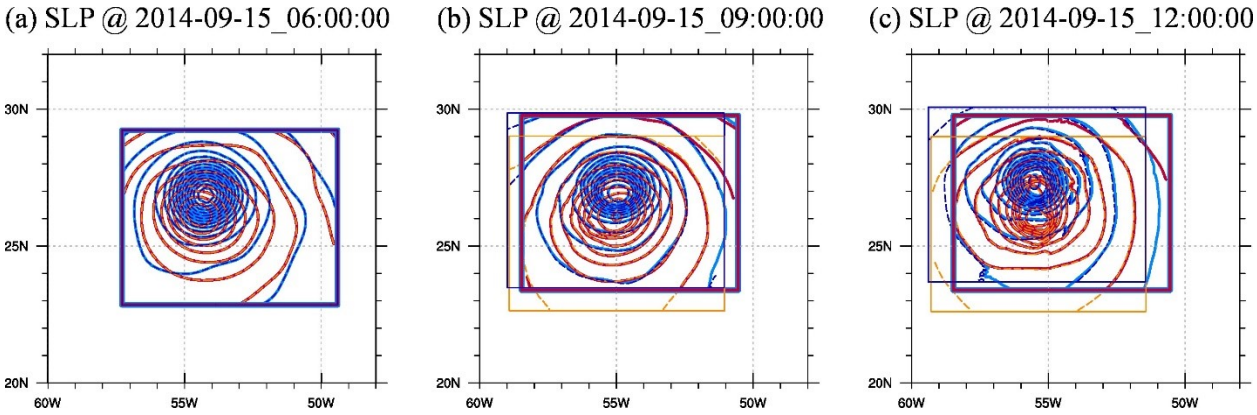

Figure 2.2 Sea-level pressure field at (a) +00:00, (b) +03:00, (c) +06:00 for the original HWRF moving strategy (dashed contour with thin box) and the directed moving strategy (solid contour with thick box) for ensemble member #1 (red & orange) and #2 (blue & cyan). Note that large areas of solid and dashed contours are overlain and indistinguishable due to the almost identical forecast fields.

Figure 2.2 illustrates the details of this directed moving nest strategy. At the initial time on September 15th, 2014, all the domains overlap (Fig. 2.2a). After three hours of integration (Fig. 2.2b), the nests of ensemble members using the storm-following moving nest strategy start to diverge, while the nests using directed moving nest strategy move toward the same location. Six hours later (Fig. 2.2c), the ensemble members using the storm-following strategy move farther apart, but those using the directed moving strategy remain in the same location. Although this

strategy differs from that used by the operational HWRF, the forecast fields after six hours of integration with each strategy are nearly identical, suggesting the directed moving nest method reconciles with the model integration as well as the storm following moving nest.

2.5 Integrating vortex relocation (VR) and modification (VM) with DA

In the operational HWRF system, vortex initialization (VI) procedure is used and primarily contains two components: a) storm location correction and b) storm size and intensity correction (Liu et al. 2000, 2006). Hereafter, in this manuscript, the "vortex relocation" (VR) refers to only the location correction and the "vortex modification" (VM) refers to the storm size and intensity correction.

The average location error in a 6-h background forecast is around 15~40 km (Trahan and Sparling 2012; Tong et al. 2014), which can be detrimental to assimilating of inner core observations using ensemble based DA that adopts the Gaussian error distribution assumption (Chen and Snyder 2007; Yang et al. 2013; Lu et al. 2017a). Therefore, in the fully cycled DA system, for each DA cycle as described in Section 2.1, both the background ensemble and control forecasts are relocated before being updated by the EnKF or EnVar. Before VR, the locations toward which the background forecasts will move are determined first. The locations are determined by applying the EnSRF method (Whitaker and Hamill 2002) to a single-variable problem as follows:

1) Update the ensemble mean location:

$$\bar{\boldsymbol{x}}^a = \bar{\boldsymbol{x}}^b + \boldsymbol{K}(\boldsymbol{y} - \boldsymbol{H}\bar{\boldsymbol{x}}^b) \,, \qquad (2.3)$$

where $\bar{\boldsymbol{x}}^a$ denotes the updated ensemble mean location, $\bar{\boldsymbol{x}}^b$ is the mean of the first guess locations, and **K** the traditional Kalman gain, which is computed as $\boldsymbol{K} = \boldsymbol{P}^b\boldsymbol{H}^T(\boldsymbol{H}\boldsymbol{P}^b\boldsymbol{H}^T + \boldsymbol{R})^{-1}$. Note that eq. (2.3) is applied on a scalar system so $\boldsymbol{P}^b$ is the location error variance estimated by

the ensemble, **H** is a unit operator because the background ensemble contains only positions of hurricanes, **y** is the location observations obtained from TCVital, and **R** is the error variance of the TCVital locations. The standard error of the TCVital locations is estimated to be 10-km in this study. This estimation is based on and adapted from Trahan and Sparling (2012).

2) Update the location perturbations

$$\boldsymbol{x'}_k^a = (\boldsymbol{I} - \widetilde{\boldsymbol{K}}\boldsymbol{H})\boldsymbol{x'}_k^b, \tag{2.4}$$

where $\widetilde{\boldsymbol{K}} = \left(1 + \sqrt{\frac{\boldsymbol{R}}{\boldsymbol{HP}^b\boldsymbol{H}^T + \boldsymbol{R}}}\right)^{-1} \boldsymbol{K}$ denotes the reduced Kalman gain, $\boldsymbol{I}$ is the identity matrix and $\boldsymbol{x'}_k^b$ are the deviation of the kth first guess location from the mean location and $\boldsymbol{x'}_k^a$ is the corresponding updated location perturbation.

3) Combine eq. (2.3) and eq. (2.4) to get the updated ensemble of locations:

$$\boldsymbol{x}_k^a = \bar{\boldsymbol{x}}^a + \boldsymbol{x'}_k^a \tag{2.5}$$

where $\boldsymbol{x}_k^a$ is the kth analyzed location.

After the locations are determined, the following relocation procedures are modified based on the HWRF VR procedure (Liu et al. 2000, 2006; Tallapragada et al. 2014) and are applied to relocate both the control and ensemble background. The HWRF forecast vortex is separated from its environment and placed in the location determined by either Eq. (2.3) or Eq. (2.5). The VM procedure is applied to the control vortices by adjusting the HWRF vortex size and intensity before putting it back into the HWRF environment. Due to the incongruences between VM and inner core DA in updating the vortex size and intensity (Zhou et al. 2015b), VM is only applied to the control background for the DA cycles when no inner-core observations (e.g. TDR data) are available.

Chapter 3: GSI-Based, Continuously Cycled, Dual-Resolution Hybrid Ensemble–Variational Data Assimilation System for HWRF: Experiments with Edouard (2014)

3.1 Introduction

An accurate estimation of the background error covariance is required to effectively assimilate observations to initialize numerical predictions of TCs. Early studies have suggested that the ensemble-based error covariance can be promising for TC DA (Zhang et al. 2009b; Torn 2010; Wang et al. 2011; Li et al. 2012; Weng and Zhang 2012; Schwartz et al. 2013, 2015; Poterjoy and Zhang 2014a; Wang and Lei 2014; Li 2015; Lu et al. 2017a).

Starting from 2013, the GSI based hybrid DA method was implemented for the operational HWRF model following the successful implementation of the hybrid DA system for the operational GFS (Wang et al. 2013; Wang and Lei 2014; Kleist and Ide 2015a,b). In this operational HWRF 3DEnVar DA system, the ensemble covariances were from either the GFS ensemble forecast or an HWRF ensemble initialized from GFS analyses (Tong et al. 2018). However, these ensembles are inherently inconsistent with the errors in the HWRF background forecast since the GFS analyses and forecasts are produced from a different model with a different resolution and assimilate different sets of observations. Therefore, these ensembles are not able to accurately estimate the error covariances associated with the higher resolution HWRF TC background forecast initialized from its own DA. We hypothesize that this inconsistency significantly degrades HWRF forecasts[2].

To investigate the hypotheses, a GSI-based hybrid EnVar DA system that uses the self-consistent HWRF EnKF ensemble was developed for HWRF (Lu et al. 2017a). As an initial

[2] Starting in 2017, the operational HWRF has implemented the capability for the self-cycled background error covariances using a new system based on that presented here (personal communication with J. Sippel, 2017).

effort, the system used a fixed, single nest domain and covered only a small period of the TC life that was surveyed by the TDR observations. Lu et al. (2017a) found that the corrections of the wind and mass fields by this hybrid DA system were dynamically and thermodynamically consistent. The self-consistent HWRF EnKF ensemble was superior to the GFS ensemble when ingested by the hybrid system for improving both the analyzed structures and forecasts of the TCs. In addition, the self-consistent hybrid system for HWRF exhibited the most benefits of assimilating airborne radar data.

In this study, the HWRF hybrid DA system is further developed to address both the scientific and technical challenges to perform end-to-end, continuous DA and forecast cycles for the entire life of a TC, and assimilating all operational observations in addition to TDR. Triply nested domains with movable inner nests are adopted during the continuous DA and forecast cycles. A remaining challenge is that the locations of the inner nests will diverge in the background ensemble if the storm-center-following moving nests are adopted. The current ensemble DA system developed based on GSI is not able to provide state updates in areas where the background ensemble nests are not co-located. A directed moving nest strategy is developed in this study to address this issue.

The positive impact of using a high-resolution NWP model in TC prediction has been found in numerous studies over the past decade (Davis and Bosart 2002; Zhu et al. 2004; Davis et al. 2010; Chen et al. 2011; Zhang et al. 2011; Dong and Xue 2013). Early studies suggested that model grid that is at least convection-allowing is required to resolve the convective scale features such as the moist convection and eyewall's dynamics (Houze et al. 2007; Zhang et al. 2011). While the operational HWRF has become convection-allowing (Tallapragada et al. 2014),

running all ensemble members at convection-allowing resolution for ensemble DA still poses challenges due to limited computing resources available at the operational centers.

Some recent studies (e.g., Li 2015; Schwartz et al., 2015) have implemented a "dual-resolution" hybrid DA method for hurricane analysis and forecast. Using the dual-resolution method, the control background forecast is run at higher resolution than the ensemble members that form the background error covariances. This approach both resolves the convective scale structures and reduces the computational cost. Schwartz et al. (2015) showed that dual-resolution hybrid DA can efficiently reduce the computational cost with minimal degradation relative to full resolution ensemble DA. However, Schwartz et al. (2015) only explored the impact of dual-resolution configuration in a coarse-resolution scenario where the control background and analysis were still at convection-parameterizing resolution. Later, Schwartz (2016) applied the dual resolution DA method to precipitation forecasts over the conterminous United States (CONUS). In their dual-resolution DA settings, a control background used 4-km convection-allowing horizontal grid spacing while the ensembles used 20-km convection-parameterizing horizontal grid spacing. The dual-resolution DA was found to improve the precipitation forecasts for the first 12 hours upon the single-resolution DA where both control background and ensembles are at 20-km convection-parameterizing horizontal grid spacing. The dual-resolution configuration has not been examined for hurricane prediction, and this study is the first to extend the capability with the newly developed HWRF hybrid DA system. In particular, the control analysis and background is run at the convection-allowing 3-km horizontal grid spacing whereas the ensemble background is run at the 9-km convection-parameterizing horizontal grid spacing. Using an experiment where all control and the ensemble are run at the

9-km horizontal grid spacing reveals the impact of introducing a convection-allowing control analysis and background for hurricane prediction.

While satellites provide the majority of observations over the open ocean, effective utilization of cloud contaminated satellite observation in DA still remains a challenge (Bauer et al. 2006, 2011; Yang et al. 2016; Zhang et al. 2016). Although various field campaigns provide unprecedented and valuable inner core observations of TCs over the open water [e.g. IFEX field campaign (Rogers et al. 2013a); Sensing Hazards with Operational Unmanned Technology (SHOUT) field campaign (Kenul et al. 2018); and TCI field campaign (Doyle et al. 2017)], it is unusual to have routine sampling of the inner-core of a TC for its entire lifetime. To partly solve this issue, early studies used bogus vortex methods to initialize vortex position and structure based on limited vortex information (Kurihara and Bender 1990; Kurihara et al. 1993, 1995; Thu and Krishnamurti 1992; Bender 1993; Pu and Braun 2001; Liu et al. 2000, 2006; Tallapragada et al. 2014). In the operational HWRF system, a similar VI procedure is used (Liu et al. 2000, 2006). In the meantime, recent studies showed that advanced DA methods can effectively extrapolate observation information without relying on the typically used VI when the inner-core observations are available (Torn and Hakim 2009a; Xiao et al. 2009; Zhang et al. 2009b, 2011; Li et al. 2012; Weng and Zhang 2012; Aksoy et al. 2013; Schwartz et al. 2013; Lu et al. 2017a). Schwartz et al. (2013) showed that when "bogus" inner-core observations are assimilated efficiently and continuously in a convection-parameterizing horizontal grid spacing (45-km) with a cycled, hybrid DA system, VR does not improve the hybrid DA for typhoon track forecasts. This study explores the extent that VI is still necessary in a fully cycled convection-allowing DA system where inner core observations are only partially available and how the VI can be integrated with the DA.

In the operational HWRF, observations are assimilated using fixed error covariances that do not evolve over the 6-hour DA window. When storms are rapidly changing, such as going through Rapid Intensification (RI) and eyewall replacement, DA methods that account for the temporal evolution of the error covariances within the 6-hour window are likely needed. Additionally, while the analysis is valid at the center of the 6-hour DA window, the inner-core observations are usually not valid at the analysis time but rather distributed over the 6-hour window depending on the aircraft flight times. In such case, using a four-dimensional error covariance will properly update the state at the analysis time. Wang and Lei (2014) illustrated in the GFS model that the GSI-based 4DEnVar can effectively resolve temporal evolution of the error covariances for hurricane analysis. However, impact of 4DEnVar in the context of convection-allowing inner-core DA has not been explored. Therefore, a 4DEnVar capability is further implemented to the HWRF hybrid system to address this question.

This chapter first describes experiments designed to assess the impact of a) introducing a high-resolution control analysis and forecast through dual-resolution DA; b) Integrating VI with DA; and c) Accounting for the temporal evolution of the error covariance with 4DEnVar (Section 3.2). Section 3.3 discusses the results associated with these experiments. In addition, as part of evaluating and understanding the performance of the newly developed system, Section 3.3 also explores the potential of the newly developed HWRF hybrid DA system to further improve intensity forecast by diagnosing the analyzed storm structure and comparing the intensity forecast with the operational HWRF. Section 3.4 concludes the Chapter. As a first step of evaluating the newly developed system and to address the aforementioned scientific and technical challenges, the cycling DA and forecast experiments were conducted for hurricane Edouard (2014). Systematic experiments are planned in the future.

3.2 Experiment Design

3.2.1 HWRF model configuration

The HWRF model has been developed by the Environmental Modeling Center (EMC) in collaboration with the Geophysical Fluid Dynamics Laboratory (GFDL) and the University of Rhode Island (URI) since 2002 (Tallapragada et al. 2014). A nominal horizontal grid spacing of 0.18/0.06/0.02 degrees (approximately 27/9/3-km) for the outermost /intermediate /innermost domains are used in this study, which is similar to that used in the 2014 operational HWRF. In this study, the intermediate and innermost domains adopt the strategies outlined in Section 2.2, while the outermost domain remains unmoved during the entire life of the storm. The outermost, intermediate, and innermost domains are configured with 216×432 horizontal grid points (approximately 80×80 degrees), 232×454 horizontal grid points (approximately 30×30 degrees) and 181×322 horizontal grid points (approximately 7×7 degrees), respectively (Figure 3.1). There are 61 vertical levels, and the model top is at 2hPa following Lu et al. (2017a). The physics parameterization schemes used in HWRF model follow those used in the 2014 operational HWRF except that the ocean coupling is turned off. Specifically, Ferrier microphysics (Ferrier 2005) as modified in HWRF for tropical applications, upgraded Simplified Arakawa-Schubert (SAS) cumulus parameterization (Han and Pan 2011), HWRF surface layer parameterization, the GFDL slab scheme (Tuleya 1994), the HWRF PBL parameterization (Hong and Pan 1996), and Eta GFDL short wave (Lacis and Hansen 1974) and long wave (Fels and Schwarzkopf 1975; Schwarzkopf and Fels 1991) radiation schemes are used to parameterize the microphysical, cumulus, surface layer, land surface, planetary boundary layer and radiation processes. The cumulus scheme is not used in the innermost domain since the 3-km horizontal

grid spacing is convection-allowing. More details about these parameterization schemes can also be found in the HWRF scientific document (Tallapragada et al. 2014).

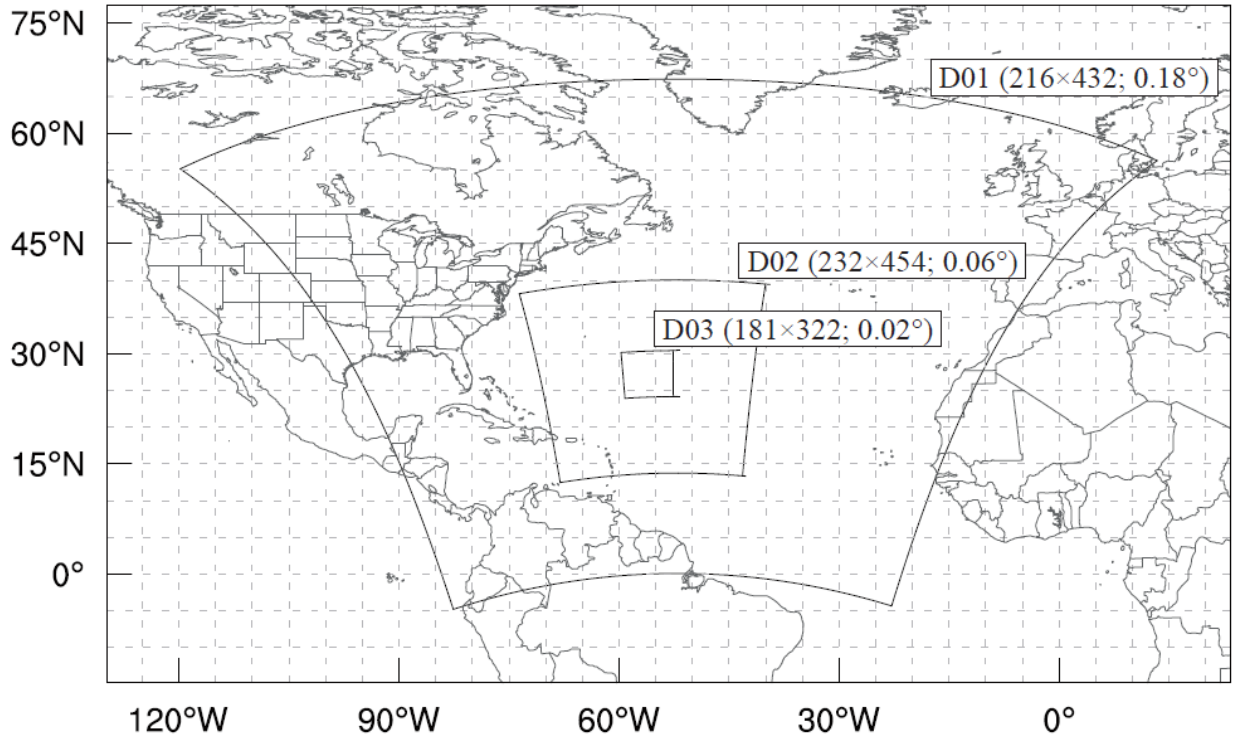

Figure 3.1 Domain configuration example for hurricane Edouard.

3.2.2 Experiment setup

Table 3.1 List of experiments and their descriptions.

Experiment name	General Features	Ensemble VR	Control VM for Non-TDR	Control VR	Dual-resolution	4DEnVar for TDR cycles
3DEV	6-hourly continuous end-to-end cycling, 3DEnVar with FGAT, directed moving nest strategy	Yes	Yes	Yes	Yes	No
3DEV-9kmS		Yes	Yes	Yes	No	No
3DEV-NEVR		No	Yes	Yes	Yes	No
3DEV-NVRM		No	No	No	Yes	No
4DEVTR		Yes	Yes	Yes	Yes	Yes

In order to address the scientific questions proposed in Section 3.1, five experiments denoted as “3DEV”, “3DEV-9kmS”, “3DEV-NVRM”, “3DEV-NEVR” and “4DEVTR” are conducted (see descriptions in Table 3.1). Details for each experiment are described as below.

3DEV is the baseline experiment, which performs 6-hourly, continuously cycled DA using 3DEnVar with FGAT following Fig. 2.1 and Section 2.1. The newly developed directed moving nest strategy is adopted as introduced in Section 2.4. 3DEV starts on 1200 UTC 11 September 2014 when Edouard (2014) developed into a tropical depression. The first DA cycle starts on 1800 UTC 11 September 2014 after 6 hours of spin-up forecast initialized from the GFS analyses. The initial 6-h ensemble is initialized from the GFS ensemble as stated in Section 2.2. The DA experiment ends on 1800 UTC 19 September 2014 when Edouard became a low pressure system. Thirty-two DA cycles are performed in total.

Table 3.2 List of observations assimilated in each domain.

Data Type \ Domain			Outermost Domain (d01)	Intermediate Domain (d02)	Innermost Domain (d03)
Conventional observations	Radiosondes		No observations are assimilated	Y	Y
	Dropwindsondes			Y	Y
	Aircraft Reports			Y	Y
	Surface Ship and Buoy Observations			Y	Y
	Surface Observations over Land			Y	Y
	Pibal Winds			Y	Y
	Wind Profilers			Y	Y
	Radar-derived Velocity Azimuth Display Wind			Y	Y
	WindSat Scatterometer Winds			Y	Y
	Integrated Precipitable Water derived from the Global Positioning System			Y	Y
Tail Doppler Radar Observation			Initialized from GFS	Y	Y
Satellite Derived Wind				Y	Y
Satellite radiances	IR	HIRS		Y	No radiances are assimilated
		AIRS		Y	
		IASI		Y	
		GOES		Y	
	MW	AMSU-A		Y	
		MHS		Y	
		ATMS		Y	

Assimilated observations include radial velocity from TDRs onboard the NOAA P-3 aircraft (when available) in addition to conventional observations and clear-sky radiances from geostationary and polar orbiting satellites (Tallapragada et al. 2014). A description of these observations assimilated for each HWRF domain is given in Table 3.2. The general distribution and preprocessing for the TDR data can be found in Gamache (2005) and Lu et al. (2017a). Although the satellite-derived wind and some in-situ observations such as dropsonde, surface ship, buoy observations are also assimilated, when it is available the TDR data plays a dominant role in sampling the inner-core region. Specifically, the TDR data is available at the 16th, 17th, 21th, 24th and 25th DA cycles valid on 1200 UTC October 15, 1800 UTC October 15, 1800 UTC October 16, 1200 UTC October 17 and 1800 UTC October 17, respectively. The major difference between assimilation on the 3- and 9-km domains is that satellite radiances are not assimilated on the innermost domain. The bias corrections for the satellite radiances are estimated from the corresponding Global Data Assimilation System (GDAS) forecast.

Following Lu et al. (2017a), an inflation factor of 0.9 is applied to the posterior ensemble variance to relax upon the prior ensemble variance during the DA cycling as proposed by Whitaker and Hamill (2012). For both the 3- and 9-km control analyses, the full ensemble error covariance is used in this study. This choice is motivated by the findings in Lu et al. (2017a) that blending the static and flow-dependent ensemble covariance does not improve upon using the full ensemble covariance. This finding is consistent with Schwartz (2016), who found that blending the covariances may be detrimental when the resolution between static and ensemble error covariances is inconsistent. The horizontal and vertical localizations adopted in this study follow the configurations in Lu et al. (2017a). For the innermost and intermediate domains, 450-

km and 1 scale-height cut-off distances (Gaspari and Cohn 1999) are respectively used for the horizontal and vertical localizations.

The 3DEV-9kmS experiment is identical to 3DEV except there is no 3-km innermost domain during DA. In other words, both the control analysis and the ingested ensemble use the 9-km horizontal grid spacing. The purpose of this experiment is to reveal the impact of introducing the 3-km horizontal grid spacing nest through dual-resolution DA in 3DEV. In order to isolate such impact, like 3DEV, 3DEV-9kmS still runs the 120h free forecast with a 27/9/3-km triply nested configuration that is achieved by interpolating the 9-km domain analysis to the innermost 3-km domain.

Experiments 3DEV-NEVR and 3DEV-NVRM examine the impacts of vortex initialization in this new DA system. 3DEV-NEVR is similar to 3DEV except that VR for the background ensemble is not performed. This experiment is meant to explore the necessity of doing VR for the ensemble background in the cycling DA system. 3DEV-NVRM follows the same procedures as 3DEV-NEVR, and the primary difference is that 3DEV-NVRM further removes the VR and VM procedures for the control background. In other words, 3DEV-NVRM performs neither VR nor VM for the control and ensemble backgrounds. The goal of this experiment is to investigate the necessity of doing VR or VM for the control member in the cycling DA system. Inter-comparison among 3DEV, 3DEV-NEVR and 3DEV-NVRM will reveal the relative importance of performing ensemble VR and VR/VM on the control member.

4DEVTR is identical to 3DEV in the DA cycles where TDR data are not available. In the cycles when TDR are available, 4DEnVar is applied in 4DEVTR for both the intermediate and innermost domains. The hourly control background and ensemble are provided for the 4DEnVar DA in this experiment following Wang and Lei (2014). The 4DEnVar is not applied to all the

cycles due to the computational constraint. The primary goal of this experiment is to explore the impact of 4DEnVar for the inner core DA.

3.3 Results

3.3.1 Impact of incorporating the higher resolution control analysis through dual-resolution DA

As stated earlier in Section 3.1, in comparison with the configuration where all ensemble members are run at a high resolution, the dual resolution configuration can save computational cost. In such a dual resolution configuration, only the control member is run at high resolution, and the rest of the ensemble members are still run at coarser resolution. Schwartz (2016) suggested the improvement of introducing a convection allowing control member through dual resolution DA for precipitation forecast over CONUS. Would introducing a single control member at a convection-allowing resolution improve the analysis and subsequent forecasts for hurricanes as well? Experiments 3DEV and 3DEV-9kmS are compared to address this question.

The vortex-scale wind structures in both the horizontal and vertical cross-sections produced by the 3DEVand 3DEV-9kmS analyses are verified against the radar wind composite of Edouard by HRD. Figure 3.2 shows the model-derived wind and the corresponding verification at the 1-km height valid at 1800 UTC 15 September 2014. The verification is derived from the quality-controlled TDR radial velocity data by HRD (Gamache, 2005; HRD radar wind data can be found: http://www.aoml.noaa.gov/hrd/Storm_pages/edouard2014/radar.html). The major difference in the analyses among 3DEV and 3DEV-9kmS is the depiction of the inner-core structures. In general, 3DEV fits the HRD composite better than 3DEV-9kmS. Specifically, 3DEV can capture the dominant wind maximum in the northeastern quadrant present in the HRD composite (Fig. 3.2a and Fig. 3.2b). In comparison, the dominant wind maximum in 3DEV-

9kmS is located in the southeastern quadrant. While 3DEV shows a circular structure consistent with the verifying wind analysis, the vortex in 3DEV-9kmS is more elliptical elongating along the northwest-southeast axis. The size of the storm is also larger in 3DEV-9kmS in comparison with the verification and 3DEV. In addition, the TC center as identified by the wind and pressure fields in 3DEV is more consistent with the best track center as compared with 3DEV-9kmS.

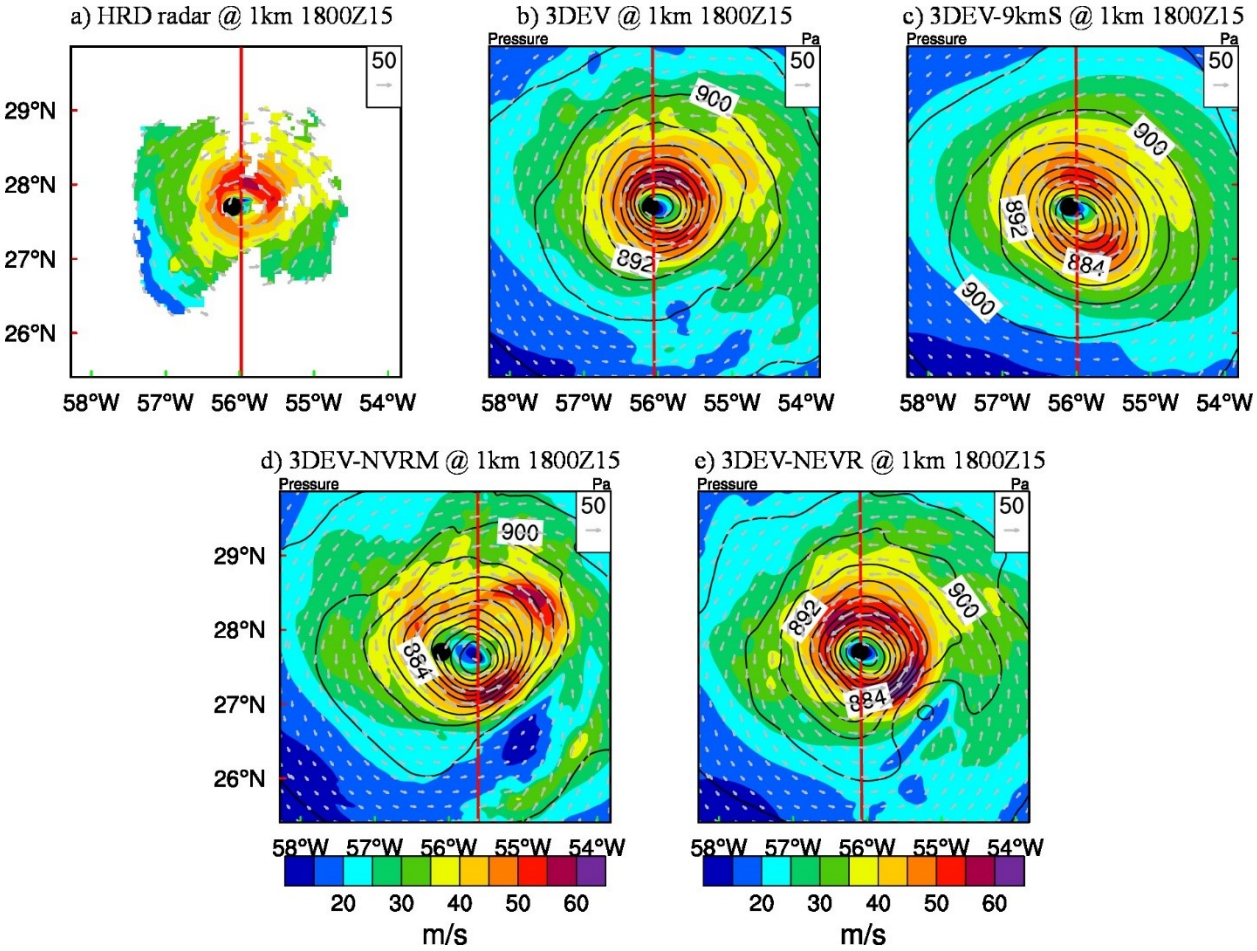

Figure 3.2 Wind (shading and vectors) and pressure (contours) at 1km height for (a) HRD radar wind composite, (b) 3DEV analysis, (c) 3DEV-9kmS analysis, (d) 3DEV-NVRM analysis, and (e) 3DEV-NEVR analysis for the second TDR mission valid at 1800 UTC 15 September 2014. Black dot is the best track position from NHC. Red line denotes the corresponding cross-sections to be presented in Figure 3.3.

Figure 3.3 shows a corresponding south-north vertical cross-section of horizontal wind speed verification. The inner-core structure in 3DEV is again more consistent with the HRD radar

wind composite than 3DEV-9kmS. Specifically, though both 3DEV and 3DEV-9kmS capture the wind maximum peaks between 1~2km in the northern side of the cross section, the overall wind maximum is stronger in 3DEV than 3DEV-9kmS. For example, the 50 m s^{-1} contour extends to 3.8 km in 3DEV, which is closer to the verification, whereas the contour only extends to 2 km in 3DEV-9kmS. In the southern side of the cross section, the wind maximum in 3DEV-9kmS is smoother and shallower compared to the HRD radar wind composite. In comparison, 3DEV shows greater spatial detail such as the narrowed peak of the 40 m s^{-1} contour above 3 km to the south, consistent with the HRD wind composite. Fig. 3.3 also reveals a stronger and narrower warm core in 3DEV than 3DEV-9kmS.

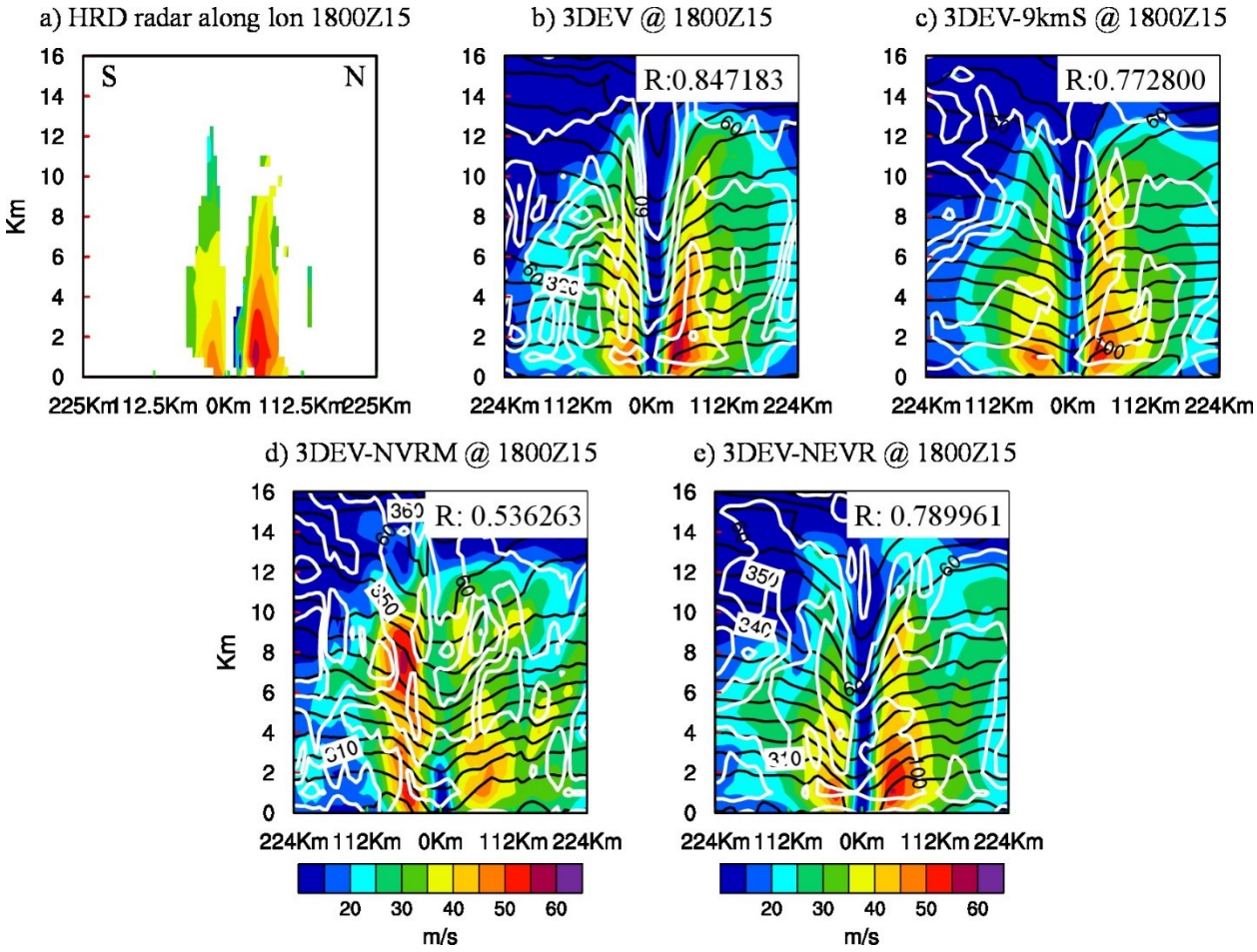

Figure 3.3 Wind speed (shading), potential temperature (black contours) and relative humidity (white contours) analysis of the south to north vertical section for (a) HRD radar wind analysis, (b) 3DEV, (c)

3DEV-9kmS, (d) 3DEV-NVRM, and (e) 3DEV-NEVR for the second TDR mission valid at 1800 UTC 15 September 2014. The values in Fig. 5b-e are the spatial correlation coefficients between the analyzed three-dimensional wind speed field and the HRD radar wind composite.

Additionally, the spatial correlation coefficient between the analyzed three-dimensional (3D) wind speed field and the HRD radar wind composite has been calculated and shown in Fig. 3.3 to provide a quantitative comparison following Lu et al. (2017)[3]. The higher correlation coefficient value in 3DEV (~0.85) suggests a better analyzed storm inner core structure as compared with 3DEV-9kmS (0.77). The average correlation coefficient for all the TDR cycles in 3DEV is 0.77, and 3DEV-9kmS it is 0.72 (Not shown). In summary, Fig. 3.2 and Fig. 3.3 show that the analyzed storm structure in 3DEV better agrees with the HRD composite than 3DEV-9kmS, suggesting the advantage of incorporating a finer resolution control analysis in the DA step through the dual-resolution EnVar capability.

In addition to the verification of the analyzed storm structures, the track, RMW, MSLP and Vmax forecasts from all of Edouard's 32 cycles from 1200 UTC 11 September to 1200 UTC 19 September 2014 for Edouard (2014) are verified against the best track data (Figure 3.4). Considering the limited samples collected from the 32 cycles, the statistical significance of the differences between the experiments is assessed using a bootstrap resampling method following Davis et al. (2010). In this bootstrap resampling method, the resampling is performed on the differences of the absolute errors between a given pair of experiments from all 32 cycles of forecasts with replacement. 10,000 resamples were formed. The statistical significance level for each pair is defined as the rank where the resampled distribution crosses zero. The significance levels of 80%, 50% and 20% are marked with red lines in Fig. 3.4a-d.

[3] The correlation coefficient is not to draw a statistically significant conclusion but to aid subjective interpretation of the analysis difference between the experiments.

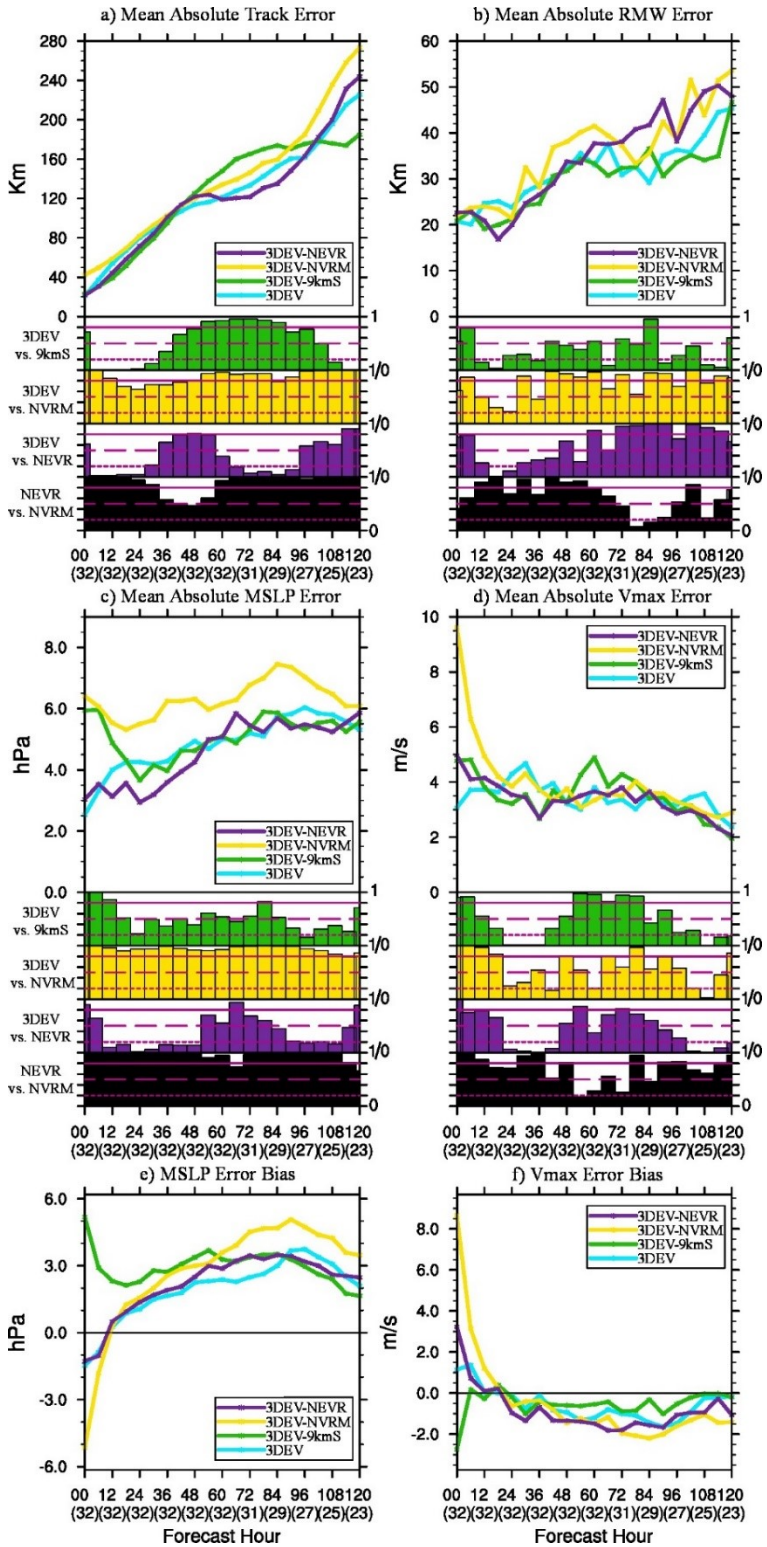

Figure 3.4 (a) Mean absolute track forecast error, (b) mean absolute RMW forecast error, (c) mean absolute MSLP forecast error and (d) mean absolute 10m Vmax forecast error for 32 missions of Edouard 2014 for 3DEV (turquoise), 3DEV-9kmS (green), 3DEV-NVRM (yellow) and 3DEV-NEVR (purple). The corresponding MSLP and Vmax forecast error bias, or mean error, are also given in (e) and (f). The green, yellow and purple histograms below (a), (b), (c) and (d) are the bootstrap significance levels where 3DEV is statistically different from 3DEV-9kmS (A: "3DEV" minus B: "3DEV-9kmS"), 3DEV-NVRM (A: "3DEV"

minus B: "3DEV-NVRM") and 3DEV-NEVR (A: "3DEV" minus B: "3DEV-NEVR"), respectively. The black histograms denote the bootstrap significance levels where 3DEV-NEVR is statistically different from 3DEV-NVRM (A: "3DEV-NEVR" minus B: "3DEV-NVRM"). The significance levels of 80% (solid) and 20% (dotted) for each pair are given as red lines in the histograms to indicate where A is significantly better or worse than B, respectively. The significance levels between 20% and 80% indicate that there is no statistically significant difference between A and B. The significance level of 50% is also shown with red dashed lines to indicate if A is better (>50%) or worse (<50%) than B. The numbers in the brackets under x-axis are the number of cases at each lead time.

According to Fig. 3.4, the profound difference between 3DEV and 3DEV-9kmS lies in the MSLP and Vmax forecasts at early lead times, and the experiments are overall comparable for both the track and RMW forecasts. For the mean absolute errors (Fig. 3.4c-d), 3DEV improves the MSLP and Vmax for the first 12-18 hours compared to 3DEV-9kmS. The smaller MSLP and Vmax forecast errors at early lead times in 3DEV are direct results of more realistically analyzed inner-core structures than 3DEV-9kmS as revealed by Fig. 3.2 and Fig. 3.3. In terms of error biases (mean error; Fig. 3.4e and Fig. 3.4f), 3DEV-9kmS produces large weak biases for both MSLP and Vmax at the initial time in comparison to the slight strong bias by 3DEV. The weak MSLP bias in 3DEV is smaller through 87 hours, whereas the weak Vmax bias is comparable or slightly weaker in 3DEV-9kmS after 12 hours. This result suggests that there is possibly a systematic difference in the wind and pressure relationship between 3DEV-9kmS and 3DEV.

3.3.2 Impact of vortex initialization (VI) and ensemble relocation

As stated in the introduction, while recent studies show that efficient DA of dense inner-core observations can potentially replace the "bogus" VI to some extent for hurricane predication, this data is only available for a small part of the lifecycle in most storms. Therefore, the VR and VM are likely necessary for a continuously cycled DA system when conventional inner-core observations are not available. Experiments are conducted in this subsection to reveal the impact of applying the VR and VM within an end-to-end, fully cycled DA system.

The analyses here show that VR and VM are most important in the control analysis, but applying VR to the background ensemble can also improve analyzed storm structure. In the horizontal structure analyses (Fig. 3.2), without applying any VR or VM, the wind structure analyses in 3DEV-NVRM largely disagree with the HRD composite (Fig. 3.2d). Specifically, the HRD radar composite contains one dominant wind maximum that is located in the northeast quadrant. In comparison, 3DEV-NVRM shows two comparable wind maxima located in the northeast and southeast quadrants respectively. The northeast wind maximum in 3DEV-NVRM is much farther away from the storm center compared to its counterpart in the HRD composite. In addition, a large location error is observed in 3DEV-NVRM. Specifically, the 3DEV-NVRM shifts the storm center about 39 km to the east of the best track position. Compared to 3DEV-NVRM, 3DEV-NEVR reduces the location error and improves storm symmetry, which shows the benefit of applying the VR and VM to only the control background. Further applying VR to the background ensemble background improves the analysis even more. For example, two errors in 3DEV-NEVR (Fig. 3.2e) that are not present in 3DEV are a dominant wind maximum southeast of the storm and a dipole feature in the pressure field. These results are consistent with previous studies such as Chen and Snyder (2007) and Lu et al. (2017a), which found dipole-like increments can occur when the storm locations prescribed in the background ensembles are too diverse or the deviation of the background storm location from the observed storm location is too large.

Vertical cross-sections similarly show that VR and VM are most important for the control analysis. The inner-core structure analyzed by 3DEV-NVRM (Fig. 3.3d) is also largely inconsistent with the HRD composite (Fig. 3.3a) with a much weaker wind maximum on the north side and a much stronger, deeper wind maximum on the south side. In comparison with

3DEV-NVRM, both the northern and southern wind maxima in 3DEV-NEVR are more consistent with the HRD composite in terms of both the vertical extent and magnitude. However, when compared to 3DEV, 3DEV-NEVR degrades the analysis. For example, the low-level wind maxima in 3DEV are more consistent with the verifying analysis.

The spatial correlation between the various analyses here and the HRD wind speed analysis objectively verifies the above conclusions. 3DEV, 3DEV-NEVR and 3DEV-NVRM are respectively correlated with the HRD analysis at ~0.85, ~0.79, and ~0.54. Furthermore, over all TDR cycles (not shown) the average correlation is 0.77, 0.71 and 0.53, respectively. In summary, the results from both the horizontal and vertical structure analyses show that conducting VR and VM on the control background plays important roles in defining the location and structure of the analyzed storm. Further conducting VR in the ensemble background is also helpful in improving the structure of the analyzed storm. However, it should also be noted that the importance of ensemble VR may not be as important as the control VR and VM.

The mean absolute forecast errors in 3DEV-NVRM are much larger at most times than those in 3DEV (Fig. 3.4a-d). Without any VR or VM, the track, RMW, MSLP and Vmax forecasts produced by 3DEV-NVRM perform the worst. Consistent with Fig. 3.2d and Fig. 3.3d, the significantly larger track error at the early lead times in 3DEV-NVRM results from large location errors in the analysis. The overall larger RMW mean absolute errors in 3DEV-NVRM than 3DEV can possibly be attributed to the unrealistically analyzed storm structure as shown in Fig. 3.2d and Fig. 3.3d where multiple wind maxima exist at different heights and distances. The highly asymmetric storm in 3DEV-NVRM analysis is also consistent with significantly larger MSLP error for all lead times and significantly larger Vmax errors in the first 21 hours in the 3DEV-NVRM forecast (Fig. 3.4c and Fig. 3.4d). Forecast error biases (Fig. 3.4e-f) show that

3DEV-NVRM has a much larger strong bias for both MSLP and Vmax than 3DEV at the initial time. At later lead times after about 12-36 hours, 3DEV-NVRM shows larger weak bias compared to 3DEV. The large bias transition at about 12 to 21-hour lead times implies a significant wind and pressure field adjustment by 3DEV-NVRM.

The forecasts in 3DEV-NEVR are better than those produced by 3DEV-NVRM. Specifically, 3DEV-NEVR produces a better track and MSLP forecast at all lead times and a better RMW and Vmax forecasts at most lead times. This result differs from the early study by Schwartz et al. (2013), who found VR applied for the control member did not improve cycling DA. Such different results could be possibly due to the continuous location correction by ingesting "bogus" inner core observations during all cycles in Schwartz et al. (2013), while this study uses no bogus data with inner core real observations available only at limited times.

Meanwhile, the performance of the track, RMW, MSLP and Vmax forecasts by 3DEV-NEVR and 3DEV are commensurate over the entire 5-day forecast period (Fig. 3.4a-d), though 3DEV-NEVR appears to be right for the wrong reason at times. Further examination reveals that 3DEV-NEVR begins with a strong bias followed by an incorrect intensification rate as implied by the evolution of bias (too slow, e.g. Fig. 3.4f). These errors effectively cancel, leading to a better fit of 3DEV-NEVR to the best track during the 18- to 48-hour lead times (e.g. Fig. 3.4c-d).

3.3.3 Impacts of 4DEnVar for vortex scale observation assimilation

As stated in Section 3.1, 3DEnVar DA with a 6-hour time window is unlikely to resolve quickly evolving storm features due to the inability of 3DEnVar to capture the temporal evolution of error covariance in a 6-hour DA window. However, 4DEnVar might alleviate this issue due to its design (Section 3.2.2). To test this hypothesis, TDR DA experiments are first conducted for the cycles when Edouard was going through the rapid eyewall replacement.

The final NOAA P3 TDR mission in Edouard occurred during the eyewall replacement or the end of the "*decaying double eyewall storm*" period (Abarca et al. 2016). During this time period, Edouard was weakening, likely due to the eyewall replacement and cold upwelling or mixing (Stewart 2014). One NOAA P3 aircraft was sent out for HRD-tasked model evaluation between 1110 UTC and 1919 UTC on Sep. 17th, 2014, but its data was unfortunately divided between the 1200 UTC and 1800 UTC cycles, yielding a brief and uneven distribution in each individual cycle. The briefly and unevenly distributed data further increase the potential benefit of 4DEnVar over 3DEnVar DA as stated in the introduction. The temporal coverage of the TDR data is between 1258-1417 UTC for the 1200 UTC cycle and between 1617-1708 UTC for the 1800 UTC cycle. The spatial coverage of the TDR data is added to Figure 3.5a.

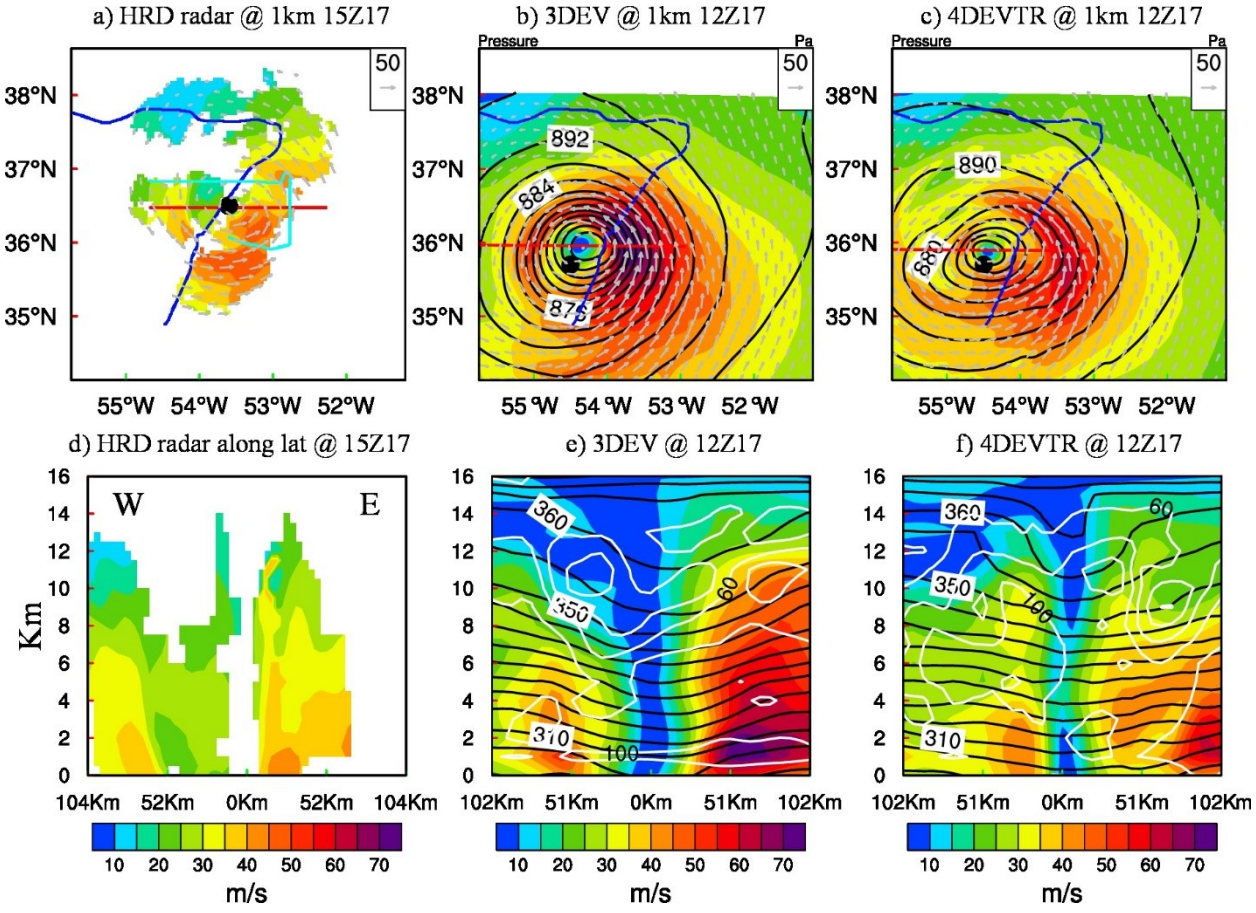

Figure 3.5 Horizontal plots of (a~c) wind (shading and vectors) and pressure (contours) at 1km height as well

as west to east cross-sections of (d~f) wind speed (shading), potential temperature (black contours) and relative humidity (white contours) for the HRD radar wind composite (first column), 3DEV (second column), and 4DEVTR (third column) for the fourth TDR-involved cycle valid at 1200 UTC 17 September 2014. The west to east vertical cross-sections in (d~f) are denoted by the corresponding red lines in (a~c). The blue line in (a~c) denotes the flight track when TDR data was available between 1258-1417 UTC, and the turquoise line in (a) denotes the flight track when TDR data is available between 1617-1708 UTC. Due to the data distribution, the HRD radar composite is valid at 1500 UTC 17 September 2014.

The 4DEnVar analysis in 4DEVTR better captures the structure of Edouard during this period. Figure 3.5 compares 1-km winds (Fig. 3.5a-c) and a vertical cross section of winds (Fig. 3.5d-f) with the HRD radar composite. The HRD radar composite shows a wind maximum southeast of the storm center as well as a secondary wind maximum east of the storm center. The vertical cross-section in Fig. 3.5d captures the edge of the inner wind maximum between 15~35 km east of the storm center as well as the complete outer maximum at 60 km. Compared with the HRD radar composite, 3DEV contains a spuriously strong wind maximum 50~75 km east of the storm (Fig. 3.5b and Fig. 3.5e), while 4DEVTR has two maxima roughly at the correct locations (Fig. 3.5c,f).

Likewise, the MSLP and Vmax forecasts initialized from the 4DEVTR analysis for this cycle are more consistent with the best track than the forecasts initialized from the 3DEV analyses, especially at early lead times (not shown). Consistent analysis and forecast performance in 4DEVTR and 3DEV are also found in the next consecutive cycle valid at 1800 UTC (not shown). This result suggests the benefit of utilizing 4DEnVar over 3DEnVar in the situation of rapidly evolving error covariance and temporally unevenly distributed observations.

Figure 3.6a-d shows the track, RMW, MSLP and Vmax forecast absolute errors over all cycles for the 4DEVTR and the 3DEV experiments. From Section 3.2.2, the only difference between 4DEVTR and 3DEV is the DA method applied for the TDR cycles. Therefore, by design, 4DEVTR reveals the direct impact of 4DEnVar on analyses and forecasts where TDR was available and also the secondary impact on subsequent analyses and forecasts. The

performance of track forecasts by 3DEV and 4DEVTR are comparable although slight but statistically significant degradation is found in 4DEVTR at longer lead times (Fig. 3.6a). The RMW absolute forecast error is also in general comparable between 3DEV and 4DEVTR except for the first 18 hours. This initial RMW degradation in 4DEVTR is primarily found during the "*decaying double-eyewall"* stage of Edouard (Abarca et al. 2016). Although the double eyewall is correctly captured by 4DEVTR and missed by 3DEV during this stage, sometimes 4DEVTR places a slightly larger wind maximum to the secondary eyewall rather than the primary eyewall, which leads to a larger RMW (not shown).

The main forecast improvement in 4DEVTR comes at early lead times. Relative to 3DEV, 4DEVTR measured in absolute errors, significantly improved MSLP forecasts for the first 15 hours and also Vmax forecasts for the first 45 hours (Fig. 3.6c-d). The MSLP and Vmax improvements at the early lead times for 4DEVTR are consistent with the better analyses that greatly reduced spurious wind maxima (e.g. Fig. 3.5 and Fig. 3.6f). The results are mixed at later lead times. Biases in 3DEV of MSLP and Vmax appear to benefit from compensating errors (i.e., strong initial bias followed by an unrealistically slow intensification rate). As shown in Fig. 3.6e-f, 4DEVTR has a much smaller bias at the initial time yet a similarly erroneous intensity evolution as 3DEV. This results in 4DEVTR having larger bias values from 6-12-hour lead time through about 66-78 hour.

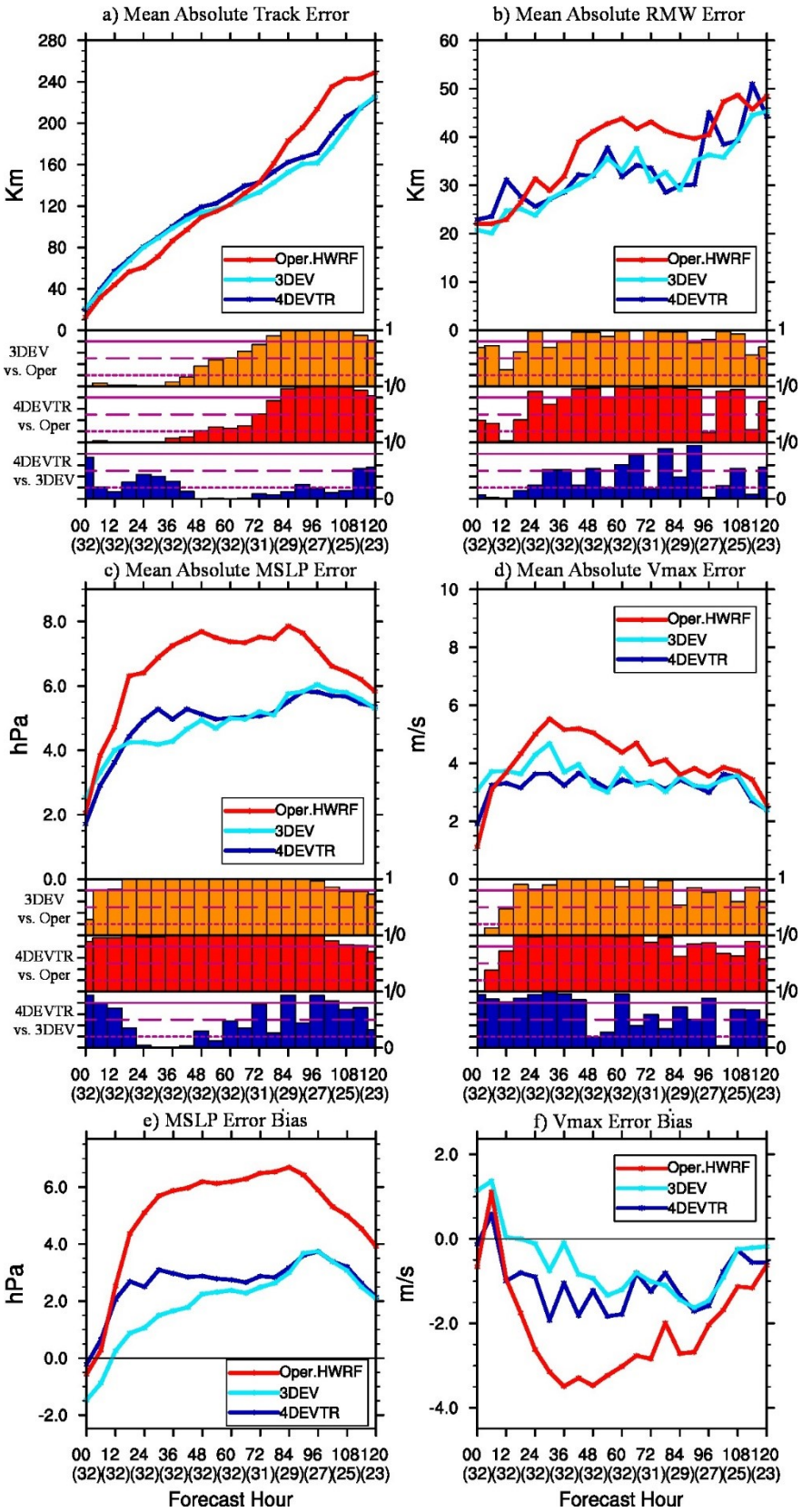

Figure 3.6 As in Figure 3.4 but for 3DEV (turquoise), 4DEVTR (blue) and the operational HWRF (red). The

orange histograms below (a), (b), (c) and (d) are the bootstrap significance levels where 3DEV is statistically different from the operational HWRF (A: "3DEV" minus B: "Oper.HWRF"). The red and blue histograms denote the bootstrap significance levels where 4DEVTR is statistically different from the operational HWRF (A: "4DEVTR" minus B: "Oper.HWRF") and 3DEV (A: "4DEVTR" minus B: "3DEV").

3.3.4 Investigation of intensity forecast improvement over the operational HWRF

As stated in the introduction, this subsection explores the potential of the newly developed DA system to improve the intensity forecast by comparing the analyzed TC structure with that from the operational HWRF where negative Vmax bias occurred during the intensification of Edouard.

Fig. 3.6 shows the Track, RMW, MSLP and Vmax forecast errors averaged over the 32 cycles from the operational HWRF. The performance of track forecasts measured in absolute errors between 4DEVTR and the 2014 operational HWRF are in general mixed, where 4DEVTR performs better in the later lead times and worse in the earlier lead times. 4DEVTR generally produces better size forecasts as compared to the operational HWRF except the first 18 hours (Fig. 3.6b). The slightly larger initial RMW of 4DEVTR has been discussed in Section 3.3.3 due to the ambiguity of identifying the RMW when realistic double eyewall is captured in 4DEVTR. Significant improvements in both MSLP and Vmax forecasts are found in 4DEVTR compared to the operational HWRF in terms of both absolute errors and biases (Fig. 3.6c-f). The only exception is the slightly worse Vmax at the analysis time, which can be attributed to not using VI for the TDR-involved cycles in 4DEVTR. Specifically, 4DEVTR improves the 0-120 h MSLP forecast and the 8-120 h Vmax forecasts as compared with the operational HWRF.

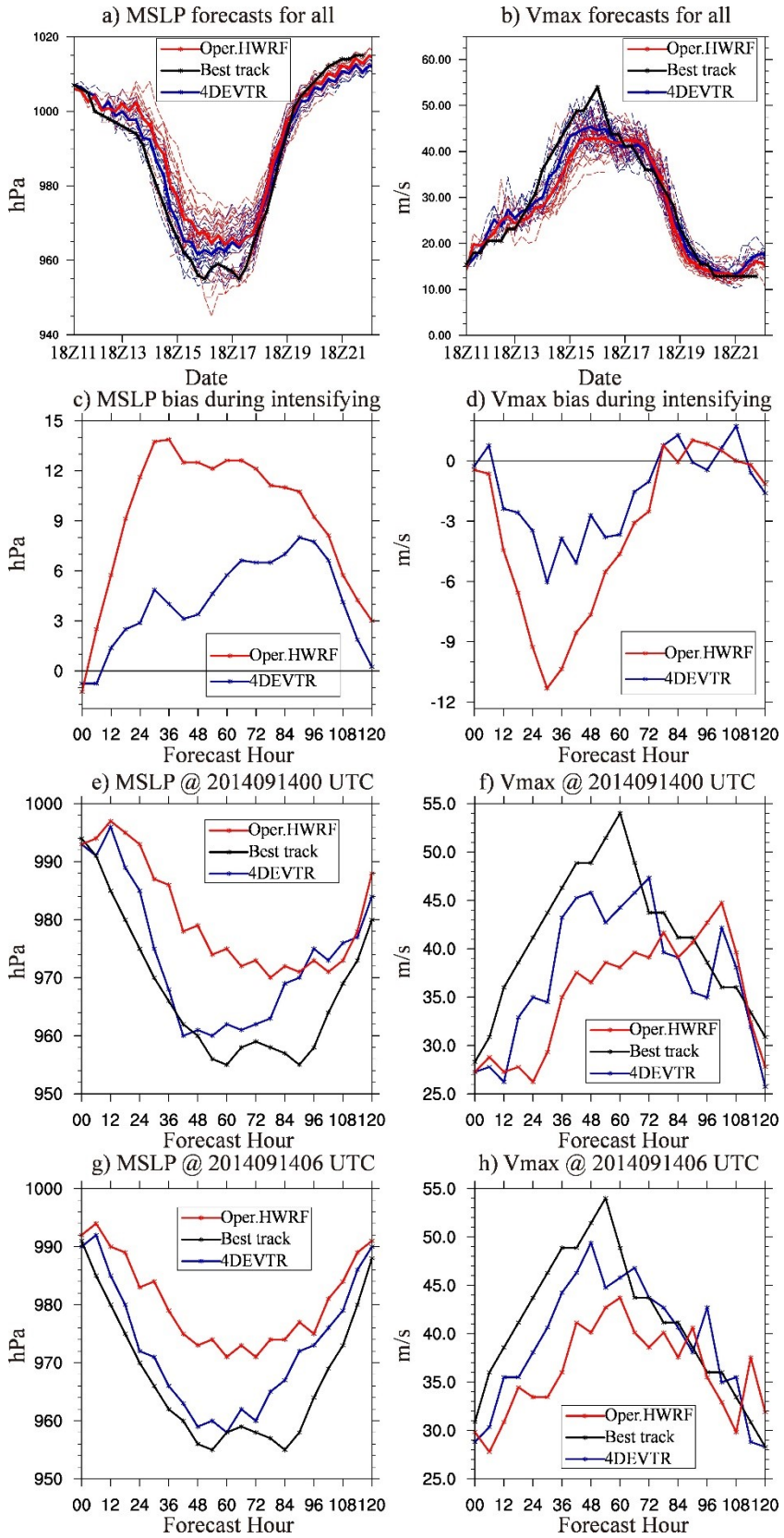

Figure 3.7 (a) MSLP and (b) Vmax forecasts for all missions during Edouard for the operational HWRF

(red), 4DEVTR (blue) and best track (black). The dashed lines denote the forecasts initialized from each DA cycle and the solid lines denote the multi-forecast average valid at the same time. The (c) MSLP and (d) Vmax forecast error bias during the intensifying period (Vmax change > 20kt 24h^{-1}) between 1200 UTC 13 September 2014 to 0600 UTC 15 September 2014 are given. The (e), (g) MSLP and (f), (h) Vmax forecast for 10th cycle at 0000 UTC (third row) and 11th cycle at 0600 UTC (fourth row) 14 September 2014 are also given.

Figure 3.7, which superposes all the deterministic MSLP and Vmax forecasts during Edouard (Fig. 3.7a and Fig. 3.7b), shows that the improvements in the forecasts from 4DEVTR primarily occur during the intensifying period[4,5]. Fig. 3.7c-d shows that 4DEVTR significantly alleviated the weak biases in the operational HWRF that resulted from slow or delayed intensification early in the forecast. Examples of two consecutive DA cycles during the intensifying period from 0000 UTC and 0600 UTC on Sep. 14th, 2014 are given in Fig. 3.7e-h. Since 4DEVTR uses the same physics as the operational HWRF (except the ocean coupling, which testing revealed to not impact results, not shown), the improvement seen here is likely a result of the upgraded DA system relative to the operational HWRF.

Figure 3.8 shows the time-averaged azimuth mean of inertial stability, radial wind and tangential wind for the analyses and 12h forecasts during the intensifying period of Edouard for both 4DEVTR and the operational HWRF. The inertial stability is calculated following Schubert and Hack (1982). In general, the analyses from 4DEVTR (Fig. 3.8a) have stronger inertial stability, a smaller RMW, shallower inflow depth and stronger tangential wind compared with the analyses from the operational HWRF (Fig. 3.8d). The high inner-core inertial stability analyses are known to favor intensification (Schubert and Hack 1982; Holland and Merrill 1984; Hack and Schubert 1986), and the consistently strong inertial stability in 4DEVTR during the first 12 hours is consistent with a continuous increase of the intensity of the storm initialized by

[4] Following Rogers et al. (2013a), an "intensifying" period is one in which the 12h best track Vmax change is greater than 20kt (24 h)$^{-1}$ [≈10.3 ms^{-1} (24 h)$^{-1}$]. Given this definition, the intensifying period is identified from 1200 UTC 13 September 2014 to 0600 UTC 15 September 2014.

[5] The first TDR mission was after this period.

4DEVTR during the intensifying period of Edouard. These features are also consistent with findings from individual cycles such as those in Fig. 3.7. On the contrary, the analyses from the operational HWRF show weaker inertial stability, larger RMW and weaker tangential wind in general (Fig. 3.8d). Therefore, the storm analyzed by the operational HWRF is less likely to produce immediate intensifications compared to 4DEVTR.

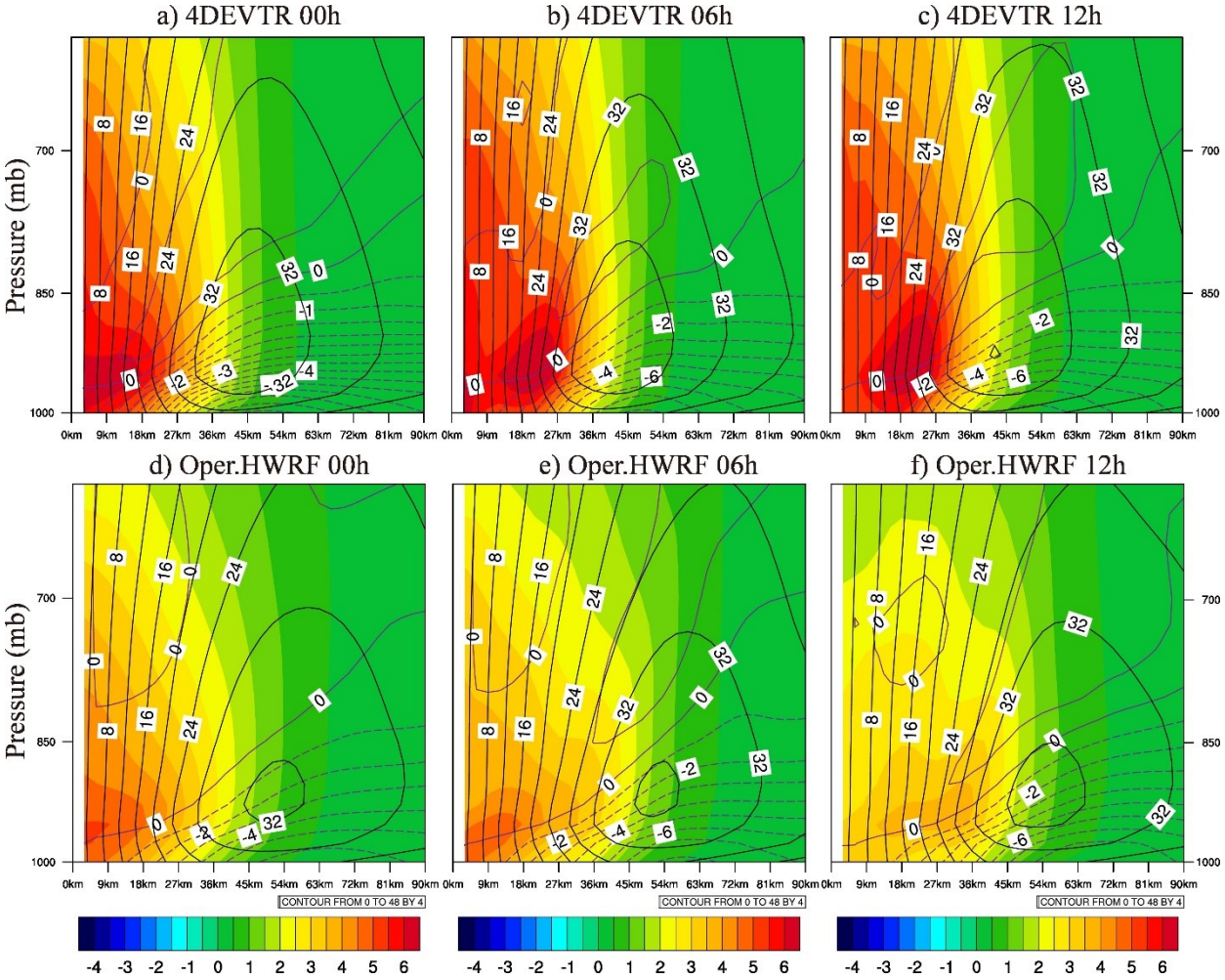

Figure 3.8 Mean azimuth mean inertial stability (shading; $10^{-6}s^{-2}$), radial wind (purple contours; dashed for inflow, solid for outflow; ms^{-1}) and tangential wind (black contours; ms^{-1}) averaged over intensifying period (8 cycles in total from 1200 UTC 13 September 2014 to 0600 UTC 15 September 2014) for 4DEVTR (first row) and the Operational HWRF (second row) and valid at 00h (first column), 06h (second column), and 12h (third column).

Additionally, similar Vmax but weaker inertial stability in the operational HWRF as compared to 4DEVTR indicates the nature of the vortices from the operational HWRF is

inherently different. Fourier decomposition diagnostics were therefore performed on the absolute vorticity in the analyses following Reasor et al. (2000) to illustrate this point. The averaged percentage of variance explained by each wavenumber within the 1.5 RMW range over all model levels during the intensifying period is shown in Table 3.3. Larger percentages on relatively high wavenumbers indicates more asymmetric TC vortices. Table 3.3 thus indicates that the analyzed operational HWRF vortices are less symmetric than those from 4DEVTR. These asymmetric anomalies possibly contribute to the delayed intensification in the operational HWRF (e.g.: Nolan and Montgomery, 2002; Nolan and Grasso, 2003; Nolan et al., 2007).

Table 3.3 Percentage of absolute vorticity variance explained by each wavenumber averaged over 1.5 RMW radius during the intensifying period from 1200 UTC 13 September 2014 to 0600 UTC 15 September 2014.

Wavenumber	0	1	2	3	4	>4
4DEVTR	83.8457	8.73058	3.29733	1.53631	0.971752	1.61828
Oper.HWRF	81.3286	8.7944	4.28238	1.91919	1.27799	2.3974

3.4 Summary and Conclusion

A GSI-based, continuously cycled, dual-resolution hybrid EnKF-Var DA system is developed for HWRF with a self-consistent HWRF EnKF ensemble and a newly developed directed moving nest strategy. Both the 3DEnVar and 4DEnVar capabilities have been implemented with the system. The system also integrates with VM and VR that are used in the operational HWRF. Using hurricane Edouard (2014), a few scientific questions discussed in Section 3.1 are investigated by multiple sets of experiments.

In the baseline 3DEV experiment, 3DEnVar with FGAT is applied every 6 hours continuously from the beginning to the end of Edouard (2014), assimilating the TDR radial velocity observations onboard NOAA P-3 aircraft in addition to all in-situ and satellite radiance observations from the operational HWRF data stream. Dual-resolution 3DEnVar is implemented

with a control analysis at 3-km horizontal grid spacing and a self-consistent HWRF EnKF ensemble at 9-km horizontal grid spacing. 3DEV adopts the newly developed directed moving nest strategy within continuous DA and forecast cycling associated with moving nests. VR is applied for both the control and ensemble background forecasts, and VM is applied to the control background in this experiment where TDR is not available. All other experiments are identical to 3DEV except each has major difference to address the scientific questions.

To investigate the impact of introducing a high-resolution nest with dual-resolution DA in the baseline 3DEV experiment, 3DEV-9kmS is conducted where both the control and the ensemble background are run at 9-km horizontal grid spacing only. With the high-resolution control analysis, 3DEV produces storm structures with more detail and in better agreement with the observations as compared with 3DEV-9kmS. The subsequent forecast suggests that the better analysis in 3DEV provides better subsequent MSLP and Vmax forecasts measured in both absolute errors and biases at early lead times compared to 3DEV-9kmS. These improvements seem to be short-lived. The track and RMW forecasts are not improved by introducing the high-resolution control analysis.

Two experiments were designed and conducted to investigate the importance of integrating VR and VM in the cycled DA system. Completely removing VR and VM (3DEV-NVRM vs. 3DEV-NEVR) significantly degrades the TC analysis, the subsequent track, Vmax and MSLP forecasts. Compared to not applying VM and VR at all (3DEV-NVRM), applying VR to the control background for all DA cycles and applying VM to the control background to the DA cycles without TDR (3DEV-NEVR) significantly improves the TC structure analysis, overall track forecasts and RMW forecasts for the first 72 hours, MSLP forecast out to 120 hours and Vmax forecast for the first 51 hours. Applying additional VR for the ensemble background

forecasts improves the TC structure analysis further (3DEV). Specifically, the wind maxima are located in the quadrant that is consistent with the verifying observations, and spurious double SLP minima no longer exist. The subsequent short-term MSLP and Vmax forecasts measured in terms of absolute errors are improved, although the improvements do not last long. The track, RMW, MSLP and Vmax forecasts in 3DEV do not in general show consistent improvement over 3DEV-NEVR. However, systematic MSLP and Vmax error bias evolutions are in general better in 3DEV than in 3DEV-NEVR especially at the early lead times.

By design, 6-hourly 3DEnVar is not able to represent the fast-evolving error structures due to the lack of temporal flow-dependency in the background error covariance. This issue is illustrated when Edouard went through rapid eyewall replacement, and the inner core TDR data was brief and unevenly distributed. Experiment 4DEVTR is designed to investigate the impact of using 4DEnVar DA in comparison with 3DEnVar for such situations. 4DEnVar improves the analyzed TC structure, as illustrated by its reduction of a spuriously strong wind maximum produced by 3DEnVar. Consistently, MSLP and Vmax forecasts are improved at early lead times initialized by 4DEnVar as compared with 3DEnVar, although slight degradations are found in the track forecasts. These track degradations warrant further investigations with a larger sample in the future.

The newly developed EnVar DA system is found to improve the MSLP and Vmax forecasts of Edouard (2014) due to the better analyses during the intensifying period compared to the operational HWRF. Further diagnostics indicate that the analyzed inner core structure by EnVar possesses stronger inner-core inertial stability, a smaller radius of maximum wind, stronger tangential wind and more symmetric inner-core vorticity structures during the intensifying period

compared to the analysis produced by the operational HWRF system. This difference in structure may be responsible for the intensity forecast improvement.

The current study represents the first step of testing, evaluating and understanding the newly developed DA system for HWRF. This system has served as a basis for the 2017 operational HWRF implementation and systematic experiments have been conducted before the implementation (personal communication with J. Sippel, 2017). Although 32 cycles of continuously cycled DA and forecasts are performed in this study, the sample size is still relatively small. Further experiments are needed to systematically test the system with many more cases and with other types of inner core observations. Additionally, more frequent assimilation cycles (e.g., using an hourly DA interval) offers an alternative way to take into account the quickly evolving error covariance. Therefore, further experiments are warranted to explore optimal DA configurations.

Chapter 4: What is Missing to Capture the Rapid Intensification of Hurricane Patricia (2015) when HWRF is already Initialized with a More Realistic Analysis?

4.1 Introduction

An accurate depiction of the TC inner-core dynamic and thermodynamic structures is essential for the numerical prediction of TC intensity (Torn and Hakim 2009b; Xiao et al. 2009; Zhang et al. 2009a, 2011; Li et al. 2012; Weng and Zhang 2012; Lu et al. 2017a,b). However, TCs spend most of their lifetime over the open ocean, where high-resolution in-situ inner-core observations are often lacking. Although satellites can cover vast areas over the ocean, effective utilization of all-sky satellite radiance observations in the cloudy and rainy regions, such as the eyewall and spiral rainbands, is still immature (Bauer et al. 2010, 2011; Yang et al. 2016; Zhang et al. 2016; Zhu et al. 2018; Geer et al. 2017).

Due to the lack of high-resolution inner-core observations, early NWP studies usually initialized the TC predictions using a bogus vortex based on limited vortex information, such as RMW, Vmax and MSLP (Thu and Krishnamurti 1992; Kurihara et al. 1995, 1998; Liu et al. 2000, 2006; Pu and Braun 2001; Tallapragada et al. 2014). As described in Section 2.5, in the NOAA operational HWRF, VI contains two components: VR and VM, where VR corrects the storm location and VM modifies the storm intensity and size. Details can be found in Liu et al. (2000, 2006) and Tallapragada et al. (2015). Briefly, VR extracts the vortex from the background HWRF forecast. VM is then performed on the extracted vortex before it is placed back. During VM, the vortex size is first modified based on the RMW and the 34-kt wind radius. Then, the axisymmetric component of the vortex is rebalanced, and a historic axisymmetric composite storm is added to the vortex to adjust the storm intensity. The added composite storm is from a HWRF simulation of a real storm in 2007 (Tallapragada et al. 2015).

However, numerous observations and studies have suggested that asymmetric dynamics can play important roles in the TC intensity prediction, especially during the intensification phase (Schubert et al. 1999; Reasor et al. 2000, 2004; Montgomery et al. 2002; Smith et al. 2008; Persing and Montgomery 2003; Braun et al. 2006; Cram et al. 2007; Sang et al. 2008; Nguyen et al. 2011; Montgomery and Smith 2014; Persing et al. 2013). For example, the rapidly-intensifying TCs are usually accompanied with asymmetric convective bursts (Montgomery et al. 2006; Fierro and Reisner 2011; Chen and Zhang 2013; Rogers et al. 2015; Susca-Lopata et al. 2015; Guimond et al. 2016). Therefore, more realistic inner-core initial conditions are required for TC predictions rather than the axisymmetric storms generated through VM. More recent studies suggested that efficient inner-core DA can be a better initialization approach than VM when inner-core observations are available (Torn and Hakim 2009b; Xiao et al. 2009; Zhang et al. 2009a, 2011; Li et al. 2012; Weng and Zhang 2012; Aksoy et al. 2013; Schwartz et al. 2013; Lu et al. 2017a,b).

In recent years, unique opportunities to sample TC inner-core structures and near-core environments have been provided by different field campaigns such as the IFEX supported by NOAA (Rogers et al. 2013a) and the TCI Experiment supported by ONR (Doyle et al. 2017) programs. Airborne instruments from aircraft from these field campaigns can provide valuable high-resolution inner- and near-core information for TCs. Examples include Doppler radar observations collected by the NOAA WP-3D/G-IV aircraft during the IFEX field campaign; and dropsondes released by the WB-57 aircraft during the TCI field campaign. Together with the enhanced high-resolution atmospheric motion vector (AMV) wind observations provided by the Cooperative Institute for Meteorological Satellite Studies (CIMSS, Velden et al. 2017), an unprecedentedly thorough three-dimensional picture of TCs can be depicted including the inner-

core, the environment, the outflow layer and the low-level inflow regions. More specific information regarding these observations will be presented in the next Chapter 5.

A cycled, dual-resolution hybrid EnKF-Var DA system based on the National Weather Service operational DA system: GSI was recently operationally implemented since 2017. The approach adopted by this system is based on Lu et al. (2017a,b). Lu et al. (2017a,b) demonstrated that the self-consistent ensemble covariance in this DA system was able to properly assimilate inner-core observations, which contributed to the improved intensity forecast. It is therefore expected that the 3D analysis produced by this DA system ingesting the abundant observations provided by IFEX, TCI and CIMMS AMVs mentioned above would be more realistic than the VM analysis.

One challenge associated with the intensity forecast by HWRF is the "spin-down" issue (Bernardet et al. 2015; Zhou et al. 2015a,b; Pu et al. 2016; Tong et al. 2018). Following these early studies, spin-down is defined as a significant vortex weakening (e.g.: Vmax drop greater than 5 ms^{-1} per 6 hours) during the first 6~12 hours of the model forecast (Bernardet et al. 2015; Zhou et al. 2015a,b; Tong et al. 2018). This definition of spin-down is used for the rest of the paper. Such a spin-down issue sometimes jeopardizes the intensity forecasts especially for strong hurricanes during the intensification period. Most early studies attributed the spin-down issue to the imbalanced, incomplete or unrealistic initial analysis (Bernardet et al. 2015; Zhou et al. 2015b; Pu et al. 2016). However, as discussed in this paper, although a more realistic initial condition was generated for hurricane Patricia (2015) using the field campaign observations and the GSI hybrid DA system compared to the VM analysis, more significant spin-down occurs during the subsequent prediction initialized by the DA analysis than the VM analysis. This more significant spin-down issue with a better DA analysis was also consistently found in Tong et al.

(2018) with a larger sample size. The primary objective of this study is to investigate the reason behind it.

Some other studies (Vukicevic et al. 2013; Tong et al. 2018) indicated that the spin-down issue is also likely be caused by the insufficient model physics, especially for the boundary layer physics. But no prominent evidence was found to support this hypothesis. As discussed later in the paper, our experiments suggest that the spin-down is largely due to the deficiency associated with the HWRF model physics schemes. Previous studies suggested that simulated TCs can be highly influenced by the turbulent diffusion processes (Emanuel 1997; Bryan and Rotunno 2009a,b; Bryan 2012; Rotunno and Bryan 2012; Zhang and Montgomery 2012; Gopalakrishnan et al. 2013; Montgomery and Smith 2014; Zhang and Marks 2015; Zhang et al. 2015). While a typical picture of TC secondary circulation in the eyewall region is an in-up-out cell (Montgomery and Smith 2014), some studies (Stern and Nolan 2011; Stern et al. 2014, 2017) suggested that there can be oscillating inflow and outflow in the vertical direction between the typical boundary layer inflow and the upper-level outflow in both observations and model simulations. Bryan and Rotunno (2009a) provides an analytical solution showing that these vertical oscillations of inflow and outflow in such TCs can be a result of unbalanced flow effects, in which the vertical sub-gradient and super-gradient oscillation plays a key role instead of the gradient-wind balance in the eyewall region. However, these unbalanced flow effects can be damped through strong radial diffusion in the models (Bryan and Rotunno 2009a). Therefore, in this study, experiments are conducted to understand if the horizontal diffusion parameterization like the horizontal mixing length scale L_h (a key parameter for horizontal diffusion configuration in the HWRF model) is too large. The overly large horizontal diffusion may spuriously damp

the realistically captured TC structures by DA analyses, which therefore results in spin-down during the prediction of hurricane Patricia (2015).

In addition to the horizontal diffusion, previous studies also suggested that the vertical diffusion can play a key role in the TC intensification process in HWRF. For example, Gopalakrishnan et al. (2013), Zhu et al. (2014) and Zhang et al. (2015) showed that the value of vertical diffusivity K_m is important for the simulated maximum intensity in both the idealized and the operational HWRF. On the other hand, Bryan and Rotunno (2009b) found in the axisymmetric model that the maximum intensity of storms are insensitive to vertical diffusivity. Zhu et al. (2018) found that there was an unrealistic discontinuity of vertical diffusion near the boundary layer top in the PBL scheme applied in the HWRF model (e.g. Fig. 4.1). This parameterization of vertical diffusivity K_m was originally designed under a clear-sky assumption where the free atmosphere has little diffusion. Therefore, K_m is always set to zero at the PBL top and the K_m above the PBL is always following the clear-sky profiles in the HWRF PBL scheme. But this assumption is not suitable for the deep convection, such as the eyewall or spiral rainbands, where in-cloud turbulence creates large mixing above the PBL. Zhu et al. (2018) proposed a modified turbulent mixing parameterization scheme that replaces the boundary layer top with a "turbulent layer" top[6] when calculating vertical diffusivity (e.g. Fig. 4.1). Although the in-cloud mixing is further considered in this new scheme, the modified vertical diffusivity is still calculated using the empirical equations with slight adaptions. As a result, the level of the peak diffusivity is elevated from inside the PBL to the middle level (e.g. 500 hPa in Fig. 4.1) and the magnitude of the peak vertical diffusivity is larger (not shown). Although the modified

[6] The turbulent layer is currently defined as the updraft greater than a certain critical value (e.g. 0.4 ms^{-1} in this study) above the boundary layer height. Therefore, in the non-deep-convection zone, the vertical diffusivity profile in the modified PBL scheme is identical to the original PBL scheme.

profile still requires further evaluation given lack of direct observations, in a recent study by Zhu et al. (2018), this modified turbulent mixing parameterization significantly improves the intensity forecast for TCs. Therefore, in this study, the impacts of the newly proposed modified turbulent mixing parameterization scheme together with the sensitivity to L_h are explored with the analysis produced from the advanced DA system to investigate the spin-down issue. Detailed diagnostics are performed to explore how and why the deficiencies of the model physics parameterizations can contribute to the spin-down issue.

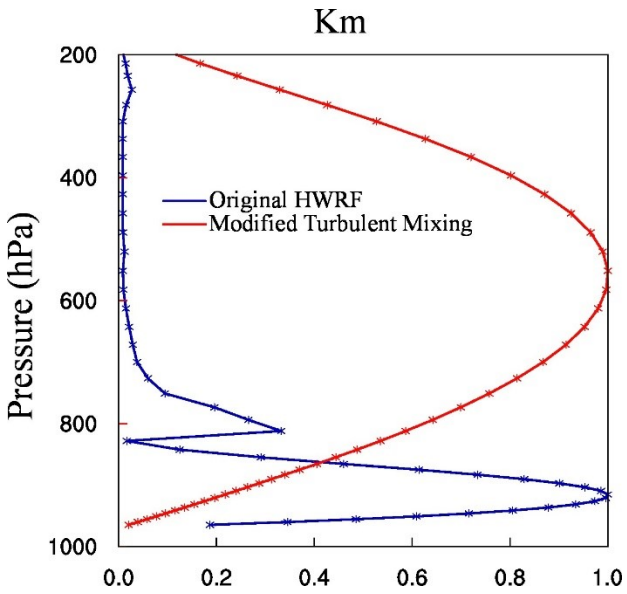

Figure 4.1 An example of the normalized vertical diffusivity profile for the original HWRF (blue) and modified turbulent mixing (red) PBL parameterization scheme. These profiles are for the eyewall.

Patricia (2015) was a category five hurricane that formed in the East Pacific on 20 October and made landfall along the southwestern coast of Mexico around 2300 UTC on 23 October 2015 (Kimberlain et al. 2016). Many have claimed that this is the strongest observed TC in the East Pacific, with a maximum surface wind speed of 95.2 ms^{-1} (185 kt, Rogers et al. 2017). But most of the operational centers failed to forecast the RI and the strong peak intensity (Qin and Zhang 2018). In this study, experiments are carried out on 1800 UTC, 22 October 2015 for the

third TCI mission which sampled the RI phase of Patricia. A detailed description of the data collected by TCI is documented in Chapter 5.

Considering the very small size of Patricia (smallest RMW recorded during Patricia's life time is about 9-km), the 2-km model grid spacing configuration may not be enough to resolve the convective-scale features well in this case. Thus, in addition to investigating the issues associated with the model physics, experiments are also performed in this study to investigate the impact of model resolution on the intensity forecast and the spin-down issue.

In this study, we first describe the DA system, the model and the experiment design in Section 4.2. Then, Section 4.3 shows the comparisons between VM and DA analyses and their subsequent forecast. As part of the comparison, investigations are carried out to understand why the more persistent TC spin-down exists with the more realistic DA analysis but not the unrealistic VM analysis. Section 4.4 explores the impacts of model PBL physics parameterization changes on the spin-down issue. Section 4.5 describes the impact of model resolution on the TC forecast and spin-down issue and Section 4.6 summarizes and concludes the results.

4.2 Methodology, Data and Experiment Design

4.2.1 System Description

Following Chapter 2, the newly developed GSI-based, continuously cycled, dual-resolution hybrid ensemble-variational (EnVar) DA system for HWRF is used in this study with some upgrades. To be consistent with the model resolution update in the 2015 operational HWRF (Tallapragada et al. 2015), a 18/6/2-km grid spacing configuration is used in this study instead of the previous 27/9/3-km grid spacing in Chapter 3. Figure 4.2 shows the flow chart of this

upgraded hybrid DA system with adaptations from Chapter 2.1. For consistency, the following descriptions parallel that of Chapter 2.1 with adaptations and simplifications.

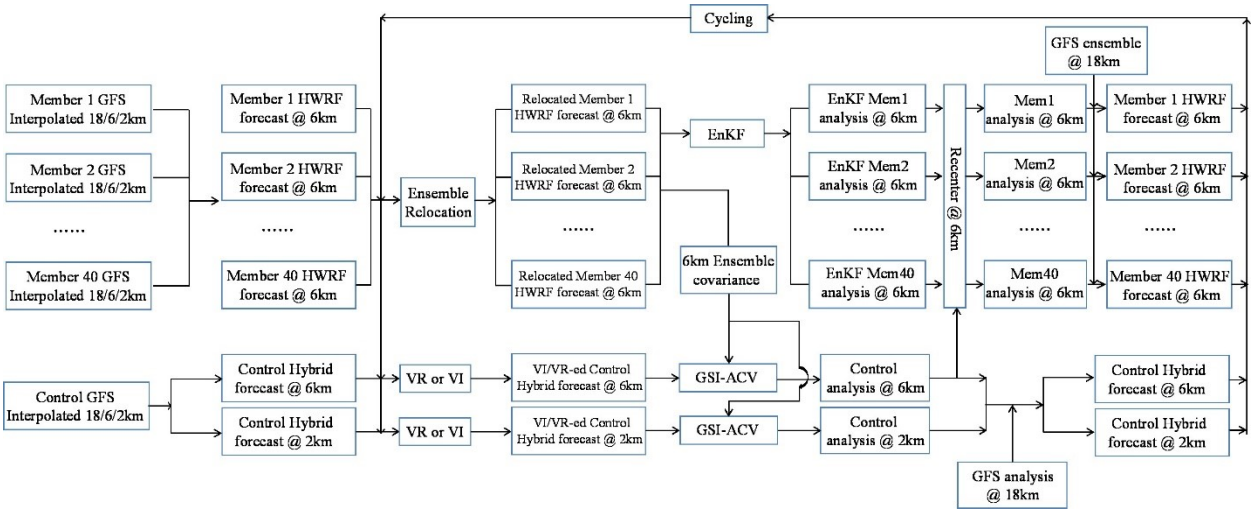

Figure 4.2 Flowchart of the GSI-based EnVar hybrid DA system for HWRF [adapted and upgraded from Fig. 2.1]. VI is a combination of VM and VR.

At the initial cycle of a storm, a 40-member 18/6-km doubly nested HWRF ensemble and a single deterministic 18/6/2-km triply nested HWRF control are initialized from the GFS ensemble and control analyses, respectively. These analyses are obtained from the NCEP operational GFS hybrid DA system (Wang et al. 2013; Wang and Lei 2014). Then, VR is performed on both ensemble and control forecasts and VM is only performed on the control forecast and only when the inner-core observations are unavailable. The details on how to perform VR and VM can be found in Chapter 2.5. These updated control and ensemble forecasts will be used as the background for the next DA. To solve the non-overlapping domain issue associated with the moving nests for the EnVar DA, the newly developed directed moving nest strategy is adopted during cycled ensemble and control forecasts following Chapter 2.1.

At the DA stage, a 40-member analysis on the 6-km grid is first produced by EnKF based on the relocated HWRF background ensemble forecast. Next, the modified control analysis on the 2- and 6-km domains is produced by the 3DEnVar using the same HWRF ensemble and the

ACV method (e.g. Wang et al. 2007; Wang 2010; Wang et al. 2013). Then the EnKF mean on the 6-km grid is replaced with the 6-km DA analysis to re-center the EnKF ensemble. During re-centering, the ensemble mean is replaced by the control analysis. After re-centering, the outermost HWRF domain on the 18-km grid is replaced by the GFS control and ensemble analyses. Similar re-centering is adopted for the global hybrid DA system (Wang et al. 2013).

After the DA stage, the updated analyses are used to produce background forecasts for the next DA cycle. For example, a 9-hour deterministic forecast is initialized from the DA analysis on the 18/6/2-km grid, and a 6-hour 40-member ensemble background forecast is initialized from the EnKF analysis on the 18/6-km grids. The directed moving nest strategy is also applied during the forecasts following Lu et al. (2017), and VR and VM procedures are conducted before applying the next DA stage. Meanwhile, an independent single deterministic 120-h free forecast is initialized from the DA analysis on the 18/6/2-km grid using HWRF's original vortex-following strategy. The above DA and forecast cycles are continuously repeated until the end of the storm. This cycled, self-consistent hybrid DA system was not implemented to operational HWRF until 2017. However, the same operational HWRF model in 2015 is used as a baseline in this study.

4.2.2 HWRF Model Configuration

Table 4.1 List of experiments and their descriptions.

<table>
<tr><th>Experiment Name</th><th>Innermost and Intermediate Domains</th><th>Outermost Domain</th><th>Model Resolution</th><th>VM</th><th>VR</th><th>Basic Model Physics</th><th>Observations Assimilated</th><th>Model Physics Change</th></tr>
<tr><td>NoDA-warm</td><td rowspan="8">6-hour control forecast initialized from 1200 UTC 22 October 2015 using the GSI-based, continuously cycled, dual-resolution hybrid ensemble-variational (EnVar) DA system for HWRF (Lu et al., 2017b) valid at 1800 UTC 22 October 2015</td><td>6-hour control forecast initialized from 1200 UTC 22 October 2015</td><td rowspan="3">18/6/2-km</td><td rowspan="3">No</td><td rowspan="3">No</td><td rowspan="8">Ferrier-Aligo microphysics scheme; simplified Arakawa-Schubert (SAS) cumulus scheme; HWRF modified surface layer scheme; Noah land surface model; HWRF PBL scheme; RRTMG longwave and shortwave radiation schemes</td><td rowspan="3">No</td><td rowspan="7">No</td></tr>
<tr><td>NoDA</td></tr>
<tr><td>VM</td></tr>
<tr><td>DA</td><td rowspan="6">GFS analysis valid at 1800 UTC 22 October 2015</td><td rowspan="5">Yes</td><td rowspan="5">Yes</td><td rowspan="5">TDR, flight level observations, SFMR, CIMSS AMV, HDSS dropsondes and operational observations (Radiosondes; Dropwindsondes; Aircraft Reports; Surface Ship and Buoy Observations; Surface Observations over Land; Pibal Winds; Wind Profilers; Radar-derived Velocity Azimuth Display Wind; WindSat Scatterometer Winds; Integrated Precipitable Water derived from the Global Positioning System; satellite radiances from HIRS, AIRS, IASI, GOES, AMSU-A, MHS and ATMS)</td></tr>
<tr><td>DA-Hi</td><td>6/2/0.67-km</td></tr>
<tr><td>DA-HD</td><td rowspan="2">18/6/2-km</td><td>Reduced “Coac” (horizontal diffusion weight) from 0.75/3.0/4.0 to 0.75/1.0/1.2</td></tr>
<tr><td>DA-HDVD</td><td>Further modified turbulent mixing parameterization (vertical diffusivity profile modification) in addition to “Coac” reduction.</td></tr>
<tr><td>DA-HDVDHi</td><td>6/2/0.67-km</td><td>No</td><td>Same as DA-HDVD except for the “Coac” is adjusted to the finer grid spacing for the innermost domain.</td></tr>
</table>

The HWRF model was developed by the Environmental Modeling Center (EMC) in collaboration with the GFDL and the University of Rhode Island (URI) based on the Weather Research and Forecasting (WRF) model infrastructure and Non-Hydrostatic Mesoscale Model (NMM) dynamic core (Tallapragada et al. 2015). As mentioned in the previous section, the operational HWRF has experienced a major update in the model grid spacing from 27/9/3-km to 18/6/2-km in 2015. Correspondingly, a horizontal grid spacing of 0.135/0.045/0.015 degrees (approximately 18/6/2-km) for the outermost/intermediate/innermost domains are used for the

newly developed DA system in this study, which is similar to that used in the 2015 operational HWRF. The outermost, intermediate, and innermost domains are configured with 288×576 (roughly 80×80 degrees), 304×604 (roughly 30×30 degrees) and 265×472 (roughly 7×7 degrees) horizontal grid points, respectively (domain size similar to Fig. 2.3). There are 61 vertical levels and the model top is at 2hPa following the operational HWRF. The physics parameterization schemes used in this study follows those used in the 2015 operational HWRF (details can be found in table 4.1).

4.2.3 Experiment Design

To understand why TC spin-down exists with the more realistic DA analysis and how the model PBL physics parameterization and model resolution can impact the spin-down and intensity forecasts, eight experiments denoted as "NoDA-warm", "NoDA", "VM", "DA", "DA-Hi", "DA-HD", "DA-HDVD" and "DA-HDVDHi" are conducted (see descriptions in Table 4.1). The analysis time of interest is 1800 UTC on 22 October 2015. Details for each experiment are described as below:

NoDA-warm is a 6-hour "non-stop" free forecast initialized from the 1200 UTC DA analyses on 22 October 2015. Seven cycles of DA and forecasts were performed before hand starting from 1800 UTC October 20, 2015 when Patricia became a tropical depression EP20 using the cycled DA system as described in Fig. 4.2 and Section 4.2.1. During these DA cycles, the same observations from the operational HWRF (Tallapragada et al. 2015) are assimilated as listed in Table 4.1.

In the NoDA experiment, the forecast is initialized by the relocated control background valid at 1800 UTC October 22, 2015. Compared to NoDA-warm which is more like a "restart" run, NoDA zeroes out the vertical velocities and hydrometeors, performs vortex relocation and

replaces the outermost domain with the GFS analysis. Comparison between NoDA and NoDA-warm will reveal if these procedures typically done before each DA update can contribute to the spin-down issue.

Experiments VM and DA perform purely VM and DA, respectively, based on the relocated background from NoDA. Specifically, DA assimilates the inner-core and near inner-core observations from IFEX, TCI field campaigns and CIMSS AMV in addition to the operational observations upon NoDA (specific observation types are listed in Table 4.1 of this paper and details of each type of observations are introduced in Chapter 5). The satellite radiances from the operational observations are only assimilated in the intermediate domain following Chapter 3 and the operational HWRF configuration (Tallapragada et al. 2015). Slightly adjusted from Lu et al. (2017a,b), the horizontal and vertical localizations used in this study are configured to be 150-km/180-km and -0.46/-0.46 scale-height recursive filter covariance localization length scale (Barker et al. 2004; Wang et al. 2008; Pan et al. 2014) for the innermost/intermediate domains, respectively. Full ensemble error covariance is used for both DA domains in this study following the configurations in Lu et al. (2017a,b). Inter-comparison between NoDA, VM and DA can help reveal why the more persistent TC spin-down occurs in the realistic DA but not in the unrealistic VM.

DA-Hi is a high-resolution (6/2/0.67-km grid spacing) forecast based on DA. Due to the constraints in the HWRF model infrastructure, current HWRF model does not support the quadruple nest domain configuration. Therefore, to investigate the model resolution impact while maintaining the benefits of the continuously cycled DA system, we utilize the relocation package from the operational HWRF (Liu et al., 2000, 2006) to downscale the analysis produced by the EnVar DA (2-km resolution) onto a higher resolution domain (0.67-km resolution).

Specifically, the analyses from 18/6/2-km grid spacing domains are first merged into one combined domain (3-km resolution). Next, the combined domain is interpolated onto finer 6/2/0.67-km grid spacing domains. Then, a 120-hour free forecast is launched based on these interpolated analyses. The goal of this high-resolution experiment is to investigate the impact of model resolution on both the spin-down issue and the TC peak intensity forecast.

DA-HD is similar to DA except using a reduced "*Coac*" (horizontal diffusion weighting factor) physics parameterization configuration from 0.75/3.0/4.0 to 0.75/1.0/1.2 for the outermost/intermediate/innermost domains, respectively. The "*Coac*" controls the magnitude of L_h. The larger the "*Coac*", the more the horizontal mixing. Different "*Coac*" values in different domains are due to the model grid spacing dependency of the horizontal eddy diffusivity (Janjic, 1990; Zhang et al., 2018). According to Zhang and Marks (2015), the configuration of 0.75/3.0/4.0 was designed for large horizontal grid spacing. Such a configuration is equivalent to the L_h of 1900-m (Zhang et al. 2018). As a result, in the 2016 operational HWRF, the "*Coac*" is reduced to 0.75/1.0/1.2, which gives an estimate of L_h at about 800-m. Zhang et al, (2018) claimed this new set of values are more consistent with the observational estimate and the model resolution (Zhang and Montgomery 2012). This latter set of values are used in this study for the "DA-HD" experiment. To reduce the accumulated effect from altered diffusion over multiple cycles, the model physics are only modified 6 hours prior the target DA cycle in this study.

Experiment DA-HDVD is based on DA-HD where a modified PBL scheme is further used to modify the vertical diffusion profile in the HWRF model in addition to the "*Coac*" reduction. This modified PBL scheme is proposed by Zhu et al. (2018) and is discussed in Section 4.1. Inter-comparison among DA, DA-HD and DA-HDVD will reveal how the model PBL physics changes impact the TC spin-down and intensity forecasts.

DA-HDVDHi is similar to DA-Hi except using the modified PBL physics including the reduced "*Coac*" and the modified PBL scheme. To be consistent with the increased model resolution, the "*Coac*" is also adjusted to the finer grid spacing for the innermost domain. Comparison between DA-HDVD and DA-HDVDHi will reveal the impact of model resolution on TC intensity forecast with the modified model physics. Inter-comparison among DA, DA-Hi, DA-HDVD and DA-HDVDHi will reveal the relative contribution of model physics and model resolution on the spin-down issue and on the peak intensity forecasts of Patricia.

4.3 Why more persistent TC spin-down exists with the more realistic analyses produced by DA?

4.3.1 Differences between VM and DA on TC analyses and forecasts

The performances of VM and DA are first compared together with NoDA in this subsection to investigate their impacts on TC analyses and forecasts in the HWRF model. The horizontal wind structures at different levels produced by the VM and DA analyses are first verified against the observations and the radar wind composite. Figure 4.3 shows the model-derived wind and the corresponding verifications at the surface and 3-km height valid at 1800 UTC 22 October 2015. The surface verification is from the observations of SFMR (Stepped Frequency Microwave Radiometer) onboard NOAA WP-3D aircraft and the 3-km height verification is composited from the TDR radial velocity data provided by HRD (Gamache 2005; both observations can be obtained from HRD, 2015). While the SFMR observations suggested a small size hurricane (RMW about 18 km) with strong surface wind maximum (close to 60 ms^{-1}; Fig. 4.3a) around the northeast of Patricia at this time, experiment NoDA produces a spuriously large hurricane (RMW about 42 km) with much weaker surface wind maximum (about 41 ms^{-1}) to the southeast (Fig. 4.3b). This spuriously large size is also found in the 3-km height verifications above the surface

(Fig. 4.3g,h). Although the magnitude of wind maximum at the 3-km height is comparable with the observations, the wind speed in the southwest of the storm in NoDA is too strong (Fig. 4.3g,h). Therefore, modifications such as VM or DA are necessary to improve this sub-optimal initial condition.

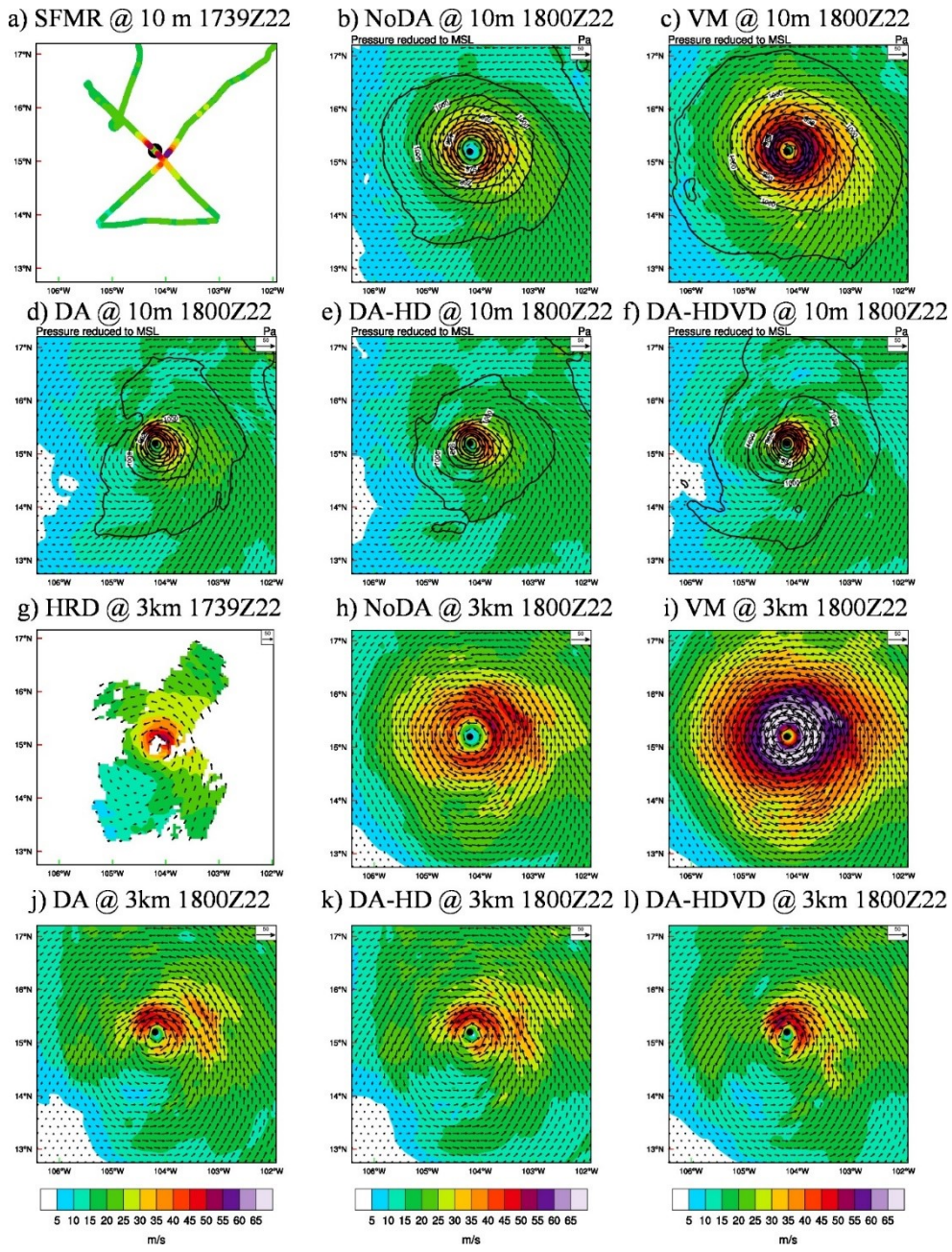

Figure 4.3 (a)~(f) Wind (shading and vectors, ms^{-1}) and pressure (contours, hPa) at 10-m height for (a) SFMR observations, (b) NoDA analysis, (c) VM analysis, (d) DA analysis, (e) DA-HD analysis and (f) DA-HDVD analysis for the third TCI mission valid at 1800 UTC, 22 Oct 2015. The black dot is the best track position

from NHC. (g)~(l) is the corresponding wind (shading and vectors) at 3-km height for (g) HRD radar composite, (h) NoDA analysis, (i) VM analysis, (j) DA analysis, (k) DA-HD analysis and (l) DA-HDVD analysis. Note, the SFMR and HRD radar composite are centered around 1739 UTC, 22 Oct 2015. There are no wind vectors in (a) SFMR observations and there are no pressure contours in both (a) SFMR and (g) TDR observations.

The corresponding analyses produced by VM and DA at different heights are shown in Fig. 4.3c,d and Fig. 4.3i,j. In the VM experiment, an axisymmetric composite vortex from the historic HWRF model forecasts is added onto the background to enhance storm intensity (Tallapragada et al. 2015). As a result, although the value of surface wind maximum in VM is modified and is now more consistent with the operational intensity estimate and the best track (Fig. 4.5a), the wind maximum above the surface becomes spuriously strong (e.g.: Fig. 4.3i). Meanwhile, although the RMW of the VM analysis is reduced slightly due to the size modification, the size of the 34 kt wind radii is significantly increased after adding the strong axisymmetric composite. In other words, the primary circulation in VM becomes spuriously large and strong. In comparison with VM, experiment DA produces a significantly contracted vortex where both the RMW and 34 kt wind radii are more consistent with the SFMR observations (Fig. 4.3d). This storm size reduction is consistently found at different levels (e.g. Fig. 4.3j). Moreover, the spuriously strong wind flows in the southwest quadrant found in NoDA are reduced to be more comparable with the HRD radar composite. However, the wind maximum in DA is positioned to the north rather than the northeast of the storm. In addition, the magnitude of this wind maximum (about 52 ms^{-1}) is still weaker than the SFMR observations at the surface. But overall, the general 3D TC inner-core structure produced by the DA experiment fits observations much better than either NoDA or VM. Further details on how assimilated observations from IFEX, TCI and CIMSS can improve various aspects of the analysis of Patricia are presented in Chapter 5.

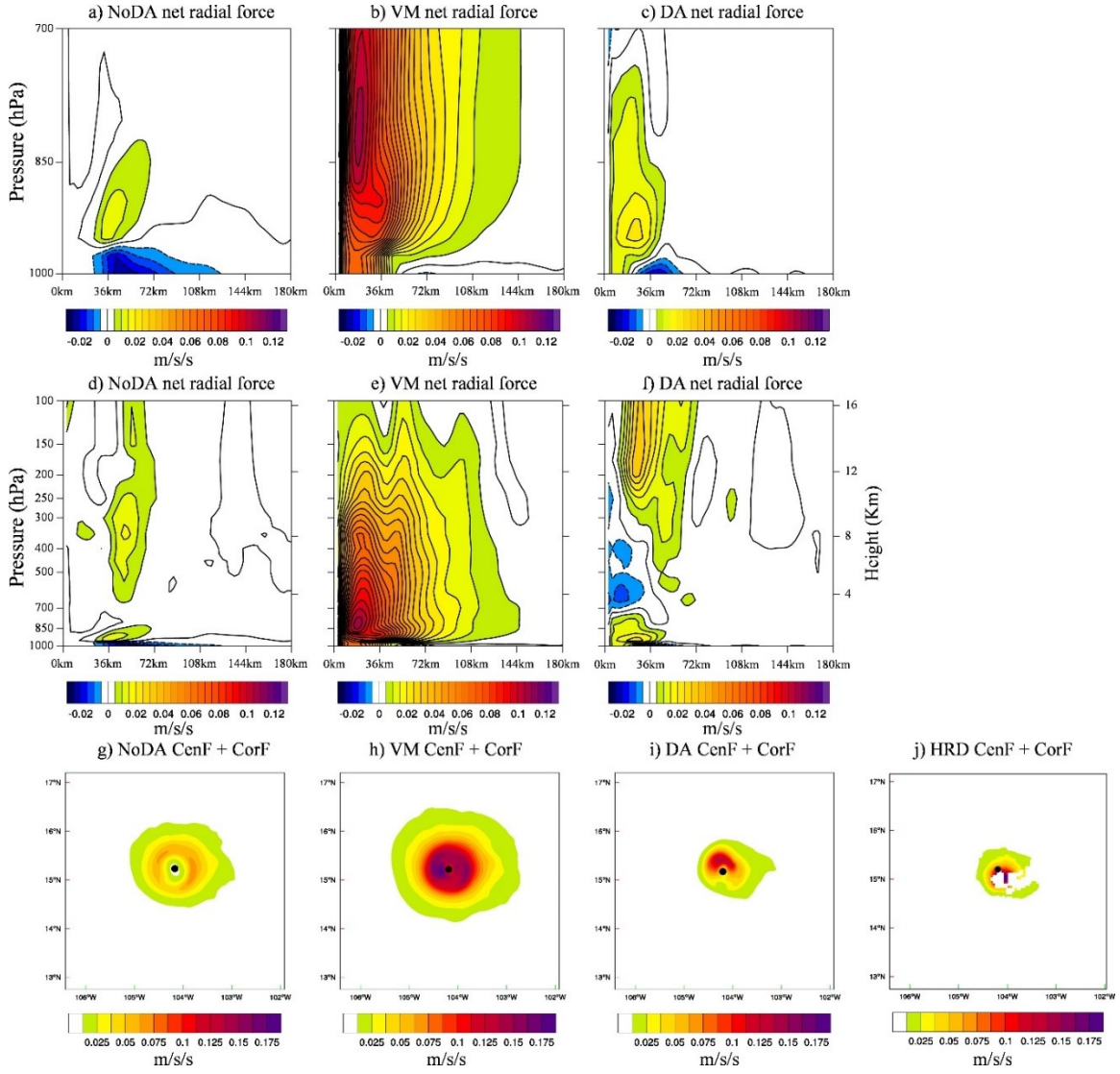

Figure 4.4 Radius-height cross-section of the isopleths of the azimuthal mean NRF (m s^{-1} s^{-1}) for (a), (d) NoDA, (b), (e) VM and (c), (f) DA analysis at 1800 UTC 22 Oct 2015. (a)~(c) is a zoom-in plot for (d)~(f) below 700 hPa and within 90 km radii. The sum of Centrifugal Force and Coriolis Force (m s^{-1} s^{-1}) at 1-km height are also given for (g) NoDA, (h) VM, (i) DA, and (j) HRD radar composite.

To further diagnose the differences among NoDA, VM and DA, the gradient wind balance (GWB) relationship within each experiment is investigated. Following Smith et al. (2009), a net radial force (NRF) field defined as the difference between the local radial pressure gradient force and the sum of centrifugal force and Coriolis force is used to describe the GWB relationship. This NRF is calculated on the pressure coordinates following Pu et al. (2009):

$$NRF = -g\frac{\partial z}{\partial r} + \frac{v^2}{r} + f_0 v \quad (4.1)$$

where z is the geopotential height, r is the radial distance, v is the tangential wind speed, and g and f_0 are the constants of gravitational acceleration and Coriolis parameter, respectively. Therefore, the GWB is established when NRF equals 0, and the flow is super-gradient or sub-gradient when NRF is larger or smaller than 0, respectively. The corresponding azimuthal mean NRF fields for each experiment in the radius-pressure cross-section are shown in Figure 4.4.

According to some previous studies, the boundary layer of an intensifying storm is found to be sub-gradient at outer radii and super-gradient at inner radii (Smith et al. 2008, 2009). Fig. 4.4a and Fig. 4.4c show that NoDA and DA are producing consistent boundary layer NRF fields with these theoretical studies. In the free atmosphere regions above the PBL, previous studies often assumed GWB and hydrostatic balance (Emanuel 1986, 1995). Consistently, Fig. 4.4d and Fig. 4.4f indicate that the NRF fields in both NoDA and DA are almost 0, or GWB, outside the eyewall region above PBL. Additionally, as indicated in Section 4.1, studies by Bryan and Rotunno (2009a, b) analytically showed that these hydrostatic and gradient-wind balances are violated near the eyewall region. They found unbalanced sub-gradient and super-gradient oscillations associated with inflow/outflow oscillations in the vertical directions around the eyewall. Stern et al. (2014, 2017) showed evidence from simulations for these unbalanced oscillations in the eyewall with strong small-size storms like Patricia (2015). Moreover, Stern et al. (2017) suggested that the atypical middle-level wind speed maxima (centered around 6-km) found in Patricia observations on Oct 23 was attributed to the unbalanced flow oscillations. Consistently, the vertical sub-gradient/super-gradient oscillations are captured by the negative/positive oscillating NRF field around the eyewall in DA analyses above the PBL although it is difficult to verify this due to the lack of enough 3D pressure observations. Thus, only the verifications of the wind related terms in the GWB equation (sum of centrifugal Force

and Coriolis Force terms) against those calculated from the HRD radar composite are conducted. The results show that the DA analysis is much more consistent with the verifications than NoDA and VM (Fig. 4.4g-j). In comparison with DA and NoDA, Fig. 4.4b and Fig. 4.4e indicate that VM is producing a significantly positive NRF field throughout the PBL and above. The spurious, positive NRF, or super-gradient, field in VM can be found far away from the eyewall even up to the 120 km radii. This spurious and strong super-gradient field in VM is a sign of initial vortex imbalance according to Pu et al. (2016).

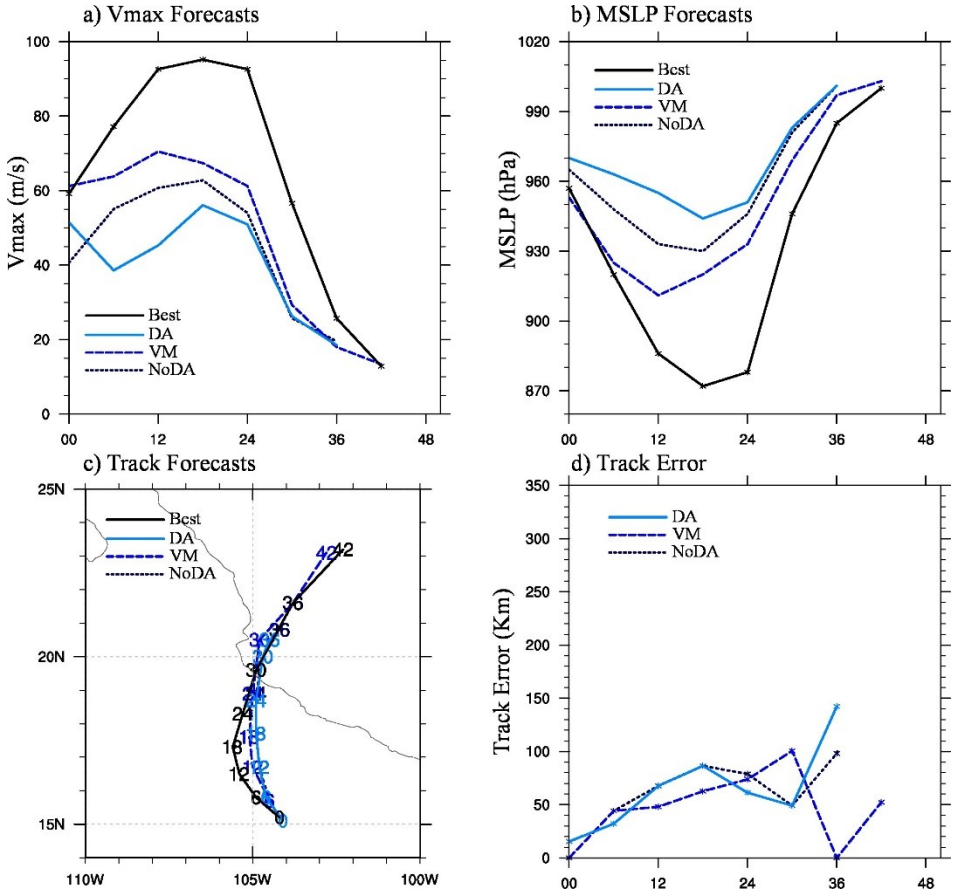

Figure 4.5 (a) 10-m Vmax forecast, (b) MSLP forecast, (c) track forecast and (d) track forecast error for NoDA (dotted navy), VM (dashed blue), DA (solid cyan) and best track (solid black) during Patricia initialized from 1800 UTC 22 Oct 2015. The numbers in (c) indicates the corresponding forecast lead time for each track forecast.

In addition to the verifications of the TC structure analyses, the Vmax, MSLP and track forecasts initialized from these analyses are verified against the best track data in Figure 4.5.

Without any DA or VM, NoDA predicts an intensifying storm. However, the initial intensity in NoDA is too weak and the intensification rate is slower than best track after hour 6 (e.g. Fig. 4.5a,b). Consequently, the forecasted peak Vmax and MSLP in NoDA is about 32 ms^{-1} and 58 hPa weaker than the best track, respectively. In addition, the track forecast from NoDA suggests an eastward bias at the early lead times before landfall (Fig. 4.5c). In comparison with NoDA, regardless of the unrealistically large, strong and super-gradient imbalanced analyses shown earlier in this subsection (Fig. 4.3c,i and Fig. 4.4b,e), VM apparently improves the Vmax and MSLP forecasts upon NoDA although the track forecast is only slightly improved. For example, the initial values of Vmax and MSLP in VM are more consistent with the best track due to the intensity modification (Fig. 4.5a-b). Additionally, the peak intensity in VM is also improved over NoDA where the peak values of Vmax and MSLP are now only 24.7 ms^{-1} and 39hPa weaker than the best track, respectively. Nevertheless, the intensification rate of VM is unreasonably slow and the timing of peak intensity in VM is shifted 6 hours earlier as compared to the best track. In comparison with VM, although DA apparently improves the initial storm structures and the initial Vmax values upon NoDA, the intensity forecast from DA is degraded. In particular, significant Vmax spin-down (about 13 ms^{-1} drop for the first 6 hours) happens in DA. As a result, the intensification in DA is delayed and the peak intensity is even weaker than NoDA. But regardless of the intensity forecast degradation, the track forecast from DA is overall comparable with NoDA (Fig. 4.5c-d).

4.3.2 Why did more persistent spin-down occur with a more realistic DA analysis?

As analyzed in the previous Section 4.3.1, VM creates spuriously strong and large storm with spuriously large super-gradient imbalance. However, this analysis produced by VM somehow improves the Vmax and MSLP forecasts upon NoDA. On the contrary, although the DA

analysis is more realistic, or more consistent with both theoretical and observed TC structures, the intensity forecast is significantly degraded upon NoDA due to the Vmax spin-down. Therefore, diagnostics are performed in this subsection to understand why the more persistent spin-down occurs with the more realistic DA analysis but not the unrealistic VM analysis.

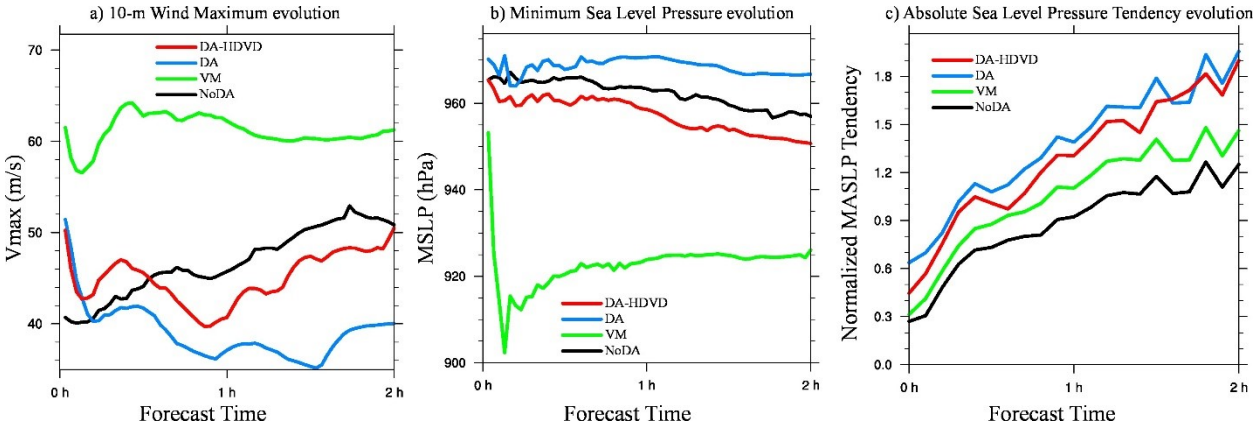

Figure 4.6 2-hour evolution of (a) 10-m Vmax, (b) MSLP and (c) NMASPT for NoDA (black), VM (green), DA (cyan) and DA-HDVD (red) initialized from 1800 UTC 22 Oct 2015. The output are plotted every 2 minutes.

The 2-min frequency outputs of the intensity forecasts from different experiments are shown in Figure 4.6 to investigate the detailed Vmax and MSLP evolutions during the first two hours. During the time period, NoDA produces a constantly intensifying storm with steady increase in Vmax and steady decrease in MSLP. This steady intensification in NoDA is consistent with the 6-hour interval outputs shown in Fig. 4.5. In comparison with NoDA, although the 6-hour interval outputs suggest a slow steady intensification in VM, the higher frequency outputs show that VM still suffers from a Vmax drop (6 ms^{-1}) during the first 10-20 minutes. Such a Vmax drop is likely to be associated with a dramatic MSLP drop (more than 50 hPa) in Fig. 4.6b. The huge MSLP drop can be attributed to the super-gradient imbalance found in Fig. 4.4, where the pressure gradient is increased by reducing the central pressure to compensate the strong wind field. After a brief (about 20~25 min) period of decaying and re-intensification, the intensity becomes near-stationary. In other words, it takes HWRF a short period of time to regain its

initial Vmax value although the VM analyzed vortex is unrealistically super-gradient. In comparison to VM, DA does not suffer from the significant MSLP drop due to the more physically balanced initial condition. However, the Vmax in DA drops more (about 16 ms^{-1}) and longer (about 1 hour) than VM. DA struggles to intensify and it never regains the initial Vmax strength over the first 6 hours. This Vmax drop, struggling to intensify, and failure to recover are reflected as the spin-down issue shown in Fig. 4.5.

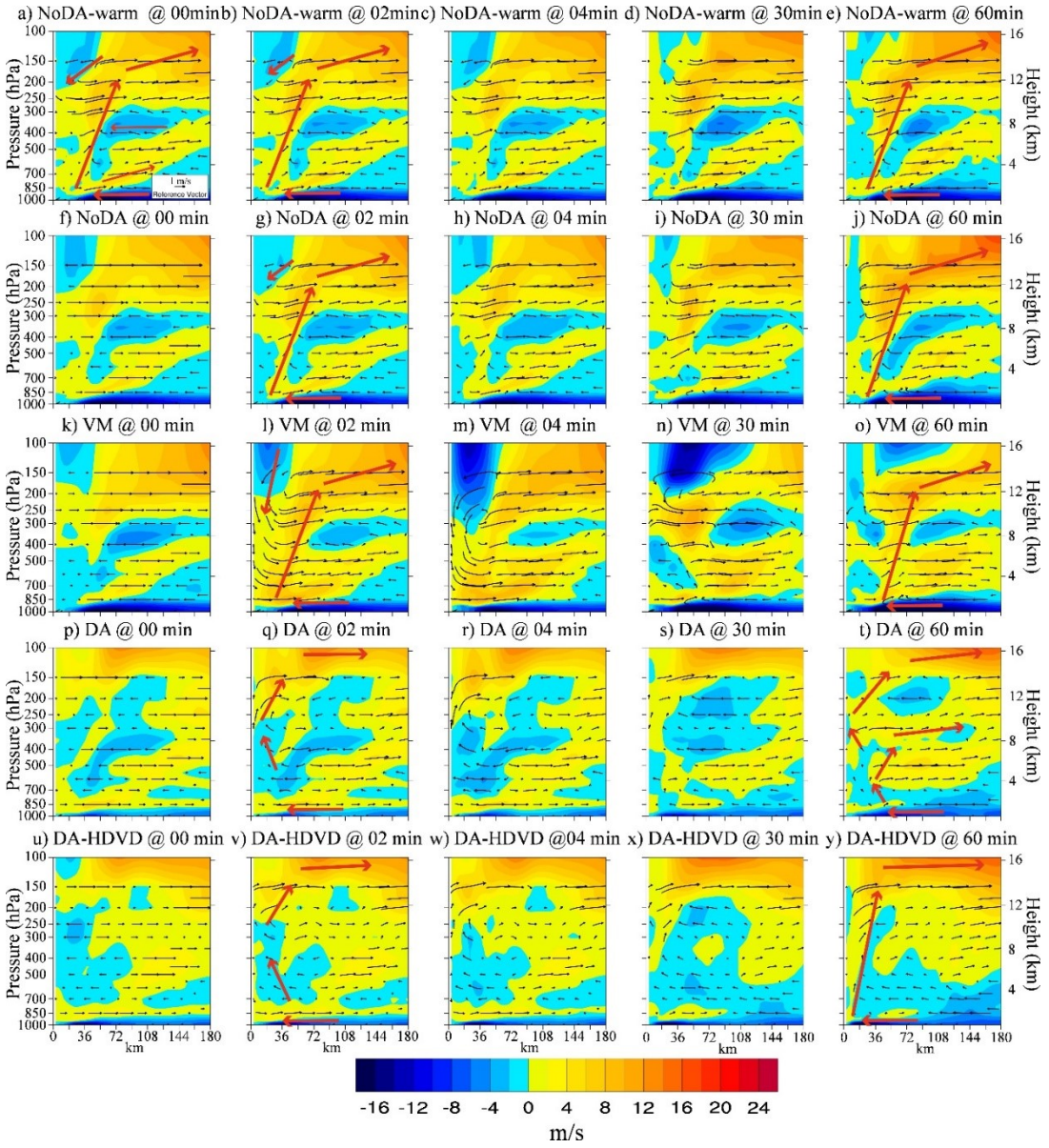

Figure 4.7 Time evolution of the azimuthal mean radial wind (shading, m s^{-1}) and secondary circulation

(vectors, m s^{-1}) for (a)~(e) NoDA-warm, (f)~(j) NoDA, (k)~(o) VM, (p)~(t) DA and (u)~(y) DA-HDVD for the (a), (f), (k), (p), (u) initial analysis; (b), (g), (l), (q), (v) 2-min forecast; (c), (h), (m), (r), (w) 4-min forecast; (d), (i), (n), (s), (x) 30-min forecast; and (e), (j), (o), (t), (y) 60-min forecast. Red arrows are added to illustrate the evolution of secondary circulations.

To understand why DA and VM evolve differently in the intensity forecast, the temporal evolution of the secondary circulation is investigated and shown in Figure 4.7. Since HWRF resets vertical velocity to 0 when it is initialized[7], and Vukicevic et al. (2013) suggested that this could be one of the factors that contribute to the spin-down issue within their HWRF Ensemble Data Assimilation System (HEDAS) system, an extra experiment NoDA-warm is first conducted to investigate the potential impact of this loss of initial velocity on the secondary circulation evolution (Fig. 4.7a-e). In NoDA-warm, the initial secondary circulation consists of four major components: a strong inflow in the boundary layer, a strong outflow in the upper-level, an updraft in the eyewall connecting the boundary layer inflow and upper-level outflow, and a weak downdraft in the upper-level eye region (Fig. 4.7a). These inner-core features are typically found in the conceptual model of a mature hurricane (e.g., Liu et al. 1997). Additionally, the inflow and outflow oscillations between the dominant upper-level outflow and boundary layer inflow are also found in NoDA-warm. As stated in Section 4.1, these vertically oscillating features are consistent with previous studies (Willoughby et al. 1984; Marks and Houze 1987; Stern and Nolan 2011; Stern et al. 2017) and are hypothesized to be related to the super-gradient/sub-gradient unbalanced oscillation around the eyewall (Bryan and Rotunno 2009a). As compared to NoDA-warm, although vertical velocity is set to 0 at the initial time (Fig. 4.7f), after only 2 minutes of model integration, the secondary circulation evolution in NoDA becomes comparable with NoDA-warm (Fig. 4.7b and Fig. 4.7g), suggesting the zeroed out vertical velocity field is not the main cause of the spin-down. This high similarity in the secondary

[7] Restart mode does not function in the HWRF model when the moving nest configuration is used.

circulation evolution between NoDA-warm and NoDA consistently exists over the first thirty minutes (Fig. 4.7a-d,f-i), and gradually diverges afterward due to the influences of relocation and GFS replacement in the outmost domain (Fig. 4.7e,j).

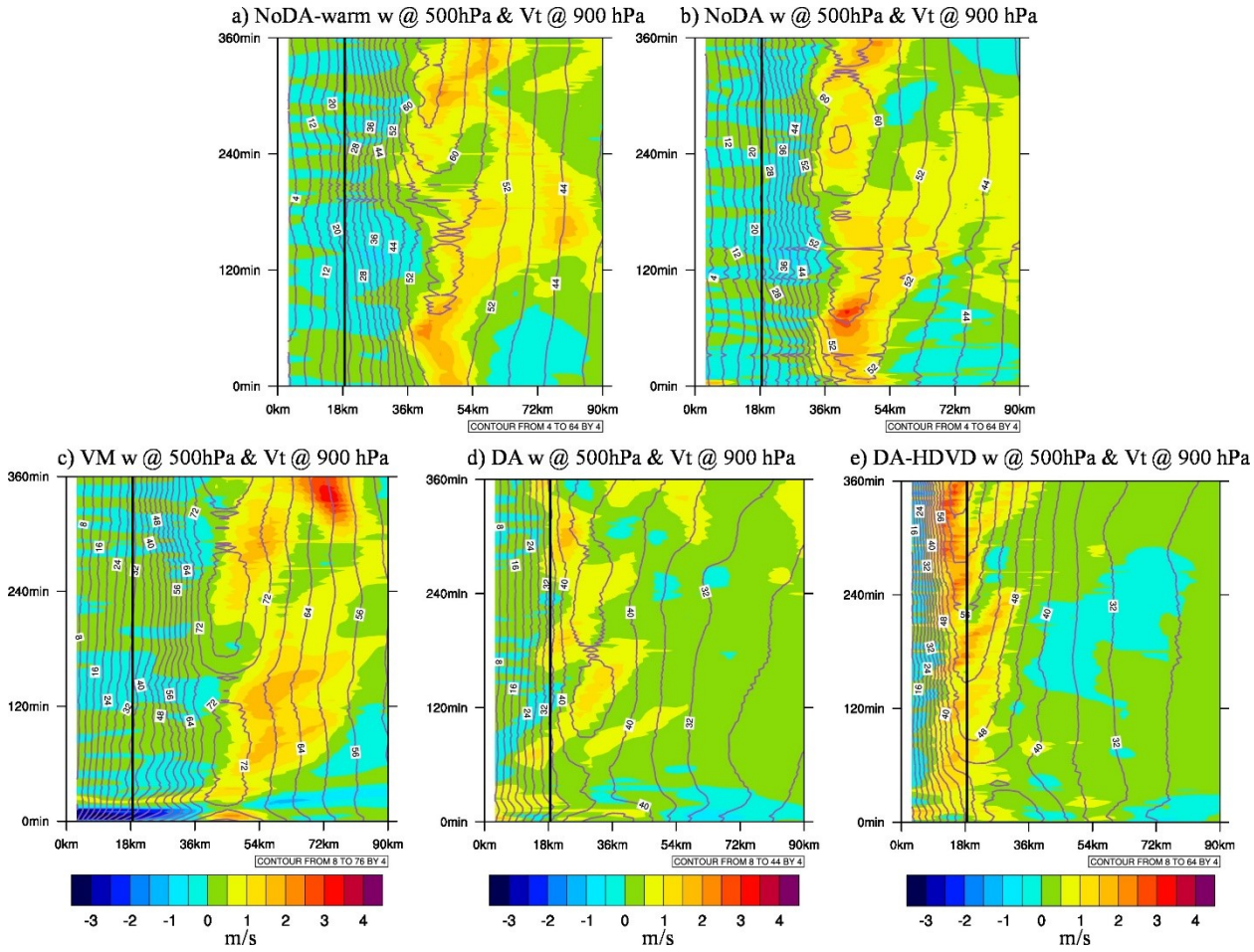

Figure 4.8 Radius-time Hovmoller plots of the 500 hPa azimuthal mean vertical velocity (shading, m s^{-1}) and 900 hPa tangential wind (contour, m s^{-1}, 4 m s^{-1} interval) for (a) NoDA-warm, (b) NoDA, (c) VM, (d) DA and (e) DA-HDVD for the first 6 hours. The RMW from the best track is given as solid black line.

To help visualize the temporal evolution of secondary circulation as analyzed above, a Hovmöller diagram is given in Figure 4.8 to mark the time evolution of the eyewall for each experiment. Consistent with Fig. 4.7a-j, Fig. 4.8a-b again show that although differences can be found, the general feature of the eyewall evolution is overall comparable between NoDA and NoDA-warm, especially during the first 2 hours. These results suggest that the resetting of initial vertical velocity in NoDA has minimal impacts on the secondary circulation evolution in

the HWRF model. Nevertheless, the eyewall in both NoDA and NoDA-warm is spuriously large in size (500 hPa radii about 45 and 40 km, respectively; Fig. 4.8a-b) compared to the small size (surface RMW about 18 km) from the best track[8].

Unlike the similar TC structures between NoDA and NoDA-warm, VM modifies NoDA significantly as shown in Fig. 4.3 and Fig. 4.4. However, the initial radial wind structures produced by VM is similar to NoDA (Fig. 4.7k). This result shows that the primary modifications in VM are through enhancing the tangential wind fields, or the primary circulation. The super-gradient imbalance found in VM starts to impact the secondary circulation structures after the model integrates (e.g. 2 minutes later). For example, spuriously strong downdraft (greater than 6 ms^{-1}) is found in the eye region (Fig. 4.7l-n). This strong downdraft is consistent with the dramatic MSLP drop found in Fig. 4.6. The downdraft warms the eye and hydrostatically lowers the surface pressure as a result of the wind and pressure adjustment. However, regardless of the spuriously strong downdraft in the eye, the typical TC secondary circulation components like the upper-level outflow, low-level inflow and the linking updraft can still be consistently found during the evolution (Fig. 4.7k-o and Fig. 4.8c). After one hour of model integration, the overly strong downdraft in the eye region is gradually reduced and the secondary circulation structure is more consistent with NoDA although the upper-level outflow is weaker (Fig. 4.7o) and the eyewall size is even larger (e.g. 500 hPa radii greater than 40 km; Fig. 4.8c).

According to the TCI dropsonde observations, the outflow of Patricia at the analysis time should be centered around 100 hPa at the outer radii of eyewall (30-60 km; shown in Chapter 5, Fig. 5.4a). However, the outflow at the outer radii of eyewall is located around 150hPa in both

[8] The RMW information is obtained from the post-season b-deck “best tracks" (available online at ftp://ftp.nhc.noaa.gov/atcf/archive/2015/)

NoDA and VM, which is lower than observed (Fig. 4.7f and Fig. 4.7k). DA elevated the outflow to 100 hPa (Fig. 4.7p), which is more consistent with the observations (shown in Chapter 5). But once the model integrates, it cannot establish a consistent updraft that directly links the elevated upper-level outflow and low-level inflow. Instead, the updraft in DA is not only weak below 300 hPa, but also oscillated inward and outward in the vertical direction. The upper part of the updraft is also pushed toward the eye such that the upper eye region is dominated by updraft instead of the typically expected weak downdraft (Fig. 4.7q). This disorganized secondary circulation is likely because the HWRF model is not able to support the strong sub-gradient/super-gradient oscillations in the DA analysis (Fig. 4.4c) where sub-gradient produces inflow and super-gradient produces outflow near the eyewall. The strong sub-gradient/super-gradient oscillation in the DA analysis is consistent with early observational and modeling study of Patricia (Stern et al. 2017). Consequently, the inflow/outflow oscillations within the updraft produce several closed small secondary circulations. This disorganized secondary circulation continues throughout the first hour and is consistent with the Vmax spin-down (Fig. 4.6a). As discussed in Section 4.1, Bryan and Rotunno (2009) found that the vertical variation associated with the unbalanced flow effects can be damped by stronger radial diffusion. It is hypothesized that one of the reasons that HWRF cannot support the realistically analyzed unbalanced oscillations in the eyewall could be that the horizontal diffusion is too large.

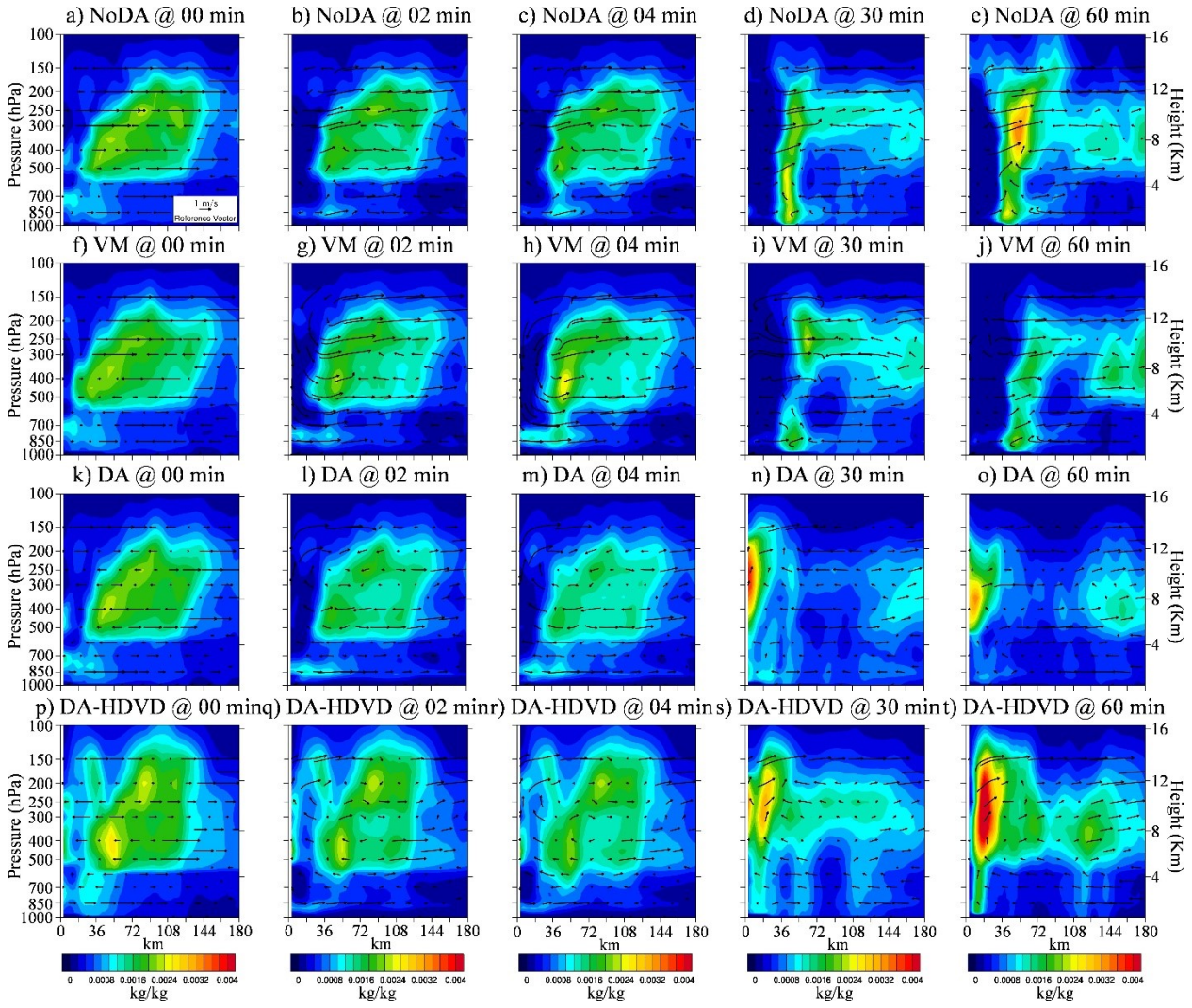

Figure 4.9 Same as Fig. 4.7 except the shading for azimuthal mean total condensate (kg kg^{-1}) for (a)~(e) NoDA, (f)~(j) VM, (k)~(o) DA and (p)~(t) DA-HDVD for the (a), (f), (k), (p) initial analysis; (b), (g), (l), (q) 2-min forecast; (c), (h), (m), (r) 4-min forecast; (d), (i), (n), (s) 30-min forecast; and (e), (j), (o), (t) 60-min forecast.

Moreover, even after one hour of model integration, the dominant updraft in the eyewall for DA is still not established (Fig. 4.7t). Figure 4.8d shows that DA is not able to build up a consistent updraft in the eyewall until about 100 min later, although the size of eyewall in DA is more consistent with the best track as compared to either NoDA or VM. Furthermore, after one-hour of model integration, the updraft in DA (Fig. 4.8d) is in general weaker in strength as compared to NoDA (Fig. 4.8b). This weak updraft cannot reach the realistically elevated upper-level outflow by DA. Therefore, a lower upper-level outflow is therefore spuriously generated

during the model integration to satisfy the mass conservation (Fig. 4.7t). The weak updraft is hypothesized to be related to the unrealistically discontinuous vertical diffusion parameterization as mentioned in section 4.1 (Fig. 4.1), where the lack of vertical diffusion at the boundary layer top constrains the upward moisture and energy transport and therefore the updraft triggered by latent heat release in the eyewall is constrained. Such an inefficient vertical energy and moisture transport is reflected by Figs. 4.9a–o where an unrealistic localized low-level total condensate maximum around 900 hPa is found in all the experiments at any forecast time in HWRF.

Overall, diagnostics in this subsection suggest that the spin-down issue in Patricia is a direct response to the secondary circulation evolution. The disorganized and weak secondary circulation is likely to be attributed to the model physics deficiencies such as the unrealistic horizontal and vertical diffusion parameterization configurations. In other words, the spin-down happens when the unrealistic model physics parameterization configurations cannot maintain the more realistic analysis produced by DA.

The mean absolute surface pressure tendency (MASPT) is usually used as a measurement of the incompatibility between the initial condition (or analysis) and the numerical model (e.g. Lynch and Huang 1992; Kleist et al. 2008; Wang et al., 2013; Lei and Whitaker, 2016). Given the surface pressure tendency will likely be dependent on the model physics itself, to facilitate quantifying the "incompatibility" between the model physics and DA analysis, a normalized mean absolute surface pressure tendency (NMASPT) is calculated in Fig. 4.6c.[9] This NMASPT is calculated by normalizing MASPT with the relatively balanced free forecast in NoDA-Warm and NoDA-HDVD-Warm. The larger the NMASPT, the more incompatible between the model and the DA analysis. Fig. 4.6c shows that VM only introduces slightly more incompatibility

[9] Sensitivity experiments suggest that deviates of NoDA from one are primarily due to the replacement of GFS analysis in the outermost domain and the VR process (not shown).

compared to NoDA since the composite vortex added in VM is from historical HWRF model forecasts and is therefore more model "compatible". In contrast, the confliction between the unrealistic model physics and the realistic analysis by DA shows significantly more incompatibility measured by NMASPT.

Therefore, the spin-down issue is hypothesized to be alleviated for the DA experiment when the model physics are improved. The hypothesis will be investigated in the next section.

4.4 Can Modified Model Physics Alleviate the spin-down issue?

As stated in Section 4.3.2, improving model physics parameterizations, such as the horizontal and vertical diffusion parameterizations, are hypothesized to help alleviate the spin-down issue. Therefore, additional experiments DA-HD and DA-HDVD with physics modifications are conducted and the best performer will be compared with DA in this section to investigate the hypothesis.

4.4.1 Impacts of model physics parameterization modifications on TC analyses and intensity forecasts

Although the 6-hour background and ensemble error covariances are different due to the use of different model physics, the DA analyses from these additional experiments are still comparable (Fig. 4.3d-f, j-l). The only exception is that DA-HDVD analysis is less symmetric than the DA analysis. This more asymmetry in DA-HDVD is reflected by the Fourier decomposition in the relative vorticity, where DA-HDVD is explained more by the higher wavenumber components as compared to DA, especially at wavenumber 2 (not shown). However, the more compact wind maximum region in DA-HDVD seems to be more consistent with the HRD radar composite. Overall, all the experiments using the 3DEnVar with inner-core

observations can capture the major TC features at different levels consistent with the verifications as discussed in Section 4.3.1. For example, the contracted storm size and the weaker wind speed to the southwest of Patricia are both captured.

Nevertheless, the intensity and track forecasts initialized from these similar analyses are different as shown in Figure 4.10. Using a reduced horizontal diffusion, DA-HD improves the MSLP forecast and shows apparent alleviation of spin-down in the Vmax forecast as compared to DA (Fig. 4.10a-b) although no improvement is found in the track forecast (Fig. 4.10c-d). Without the significant spin-down issue, the simulated peak intensity of DA-HD is increased over the peak intensity of DA, and is closer to the best track. This improved Vmax forecast suggests that the overly large horizontal diffusion is likely one of the reasons for the spin-down issue during the prediction of Patricia as hypothesized. But the RI rate in DA-HD is still slower than the best track and so is the peak intensity. This slow and weak intensification in DA-HD is likely still due to the lack of strong updraft connecting the realistically elevated upper-level outflow as suggested in Section 4.3.2 (not shown).

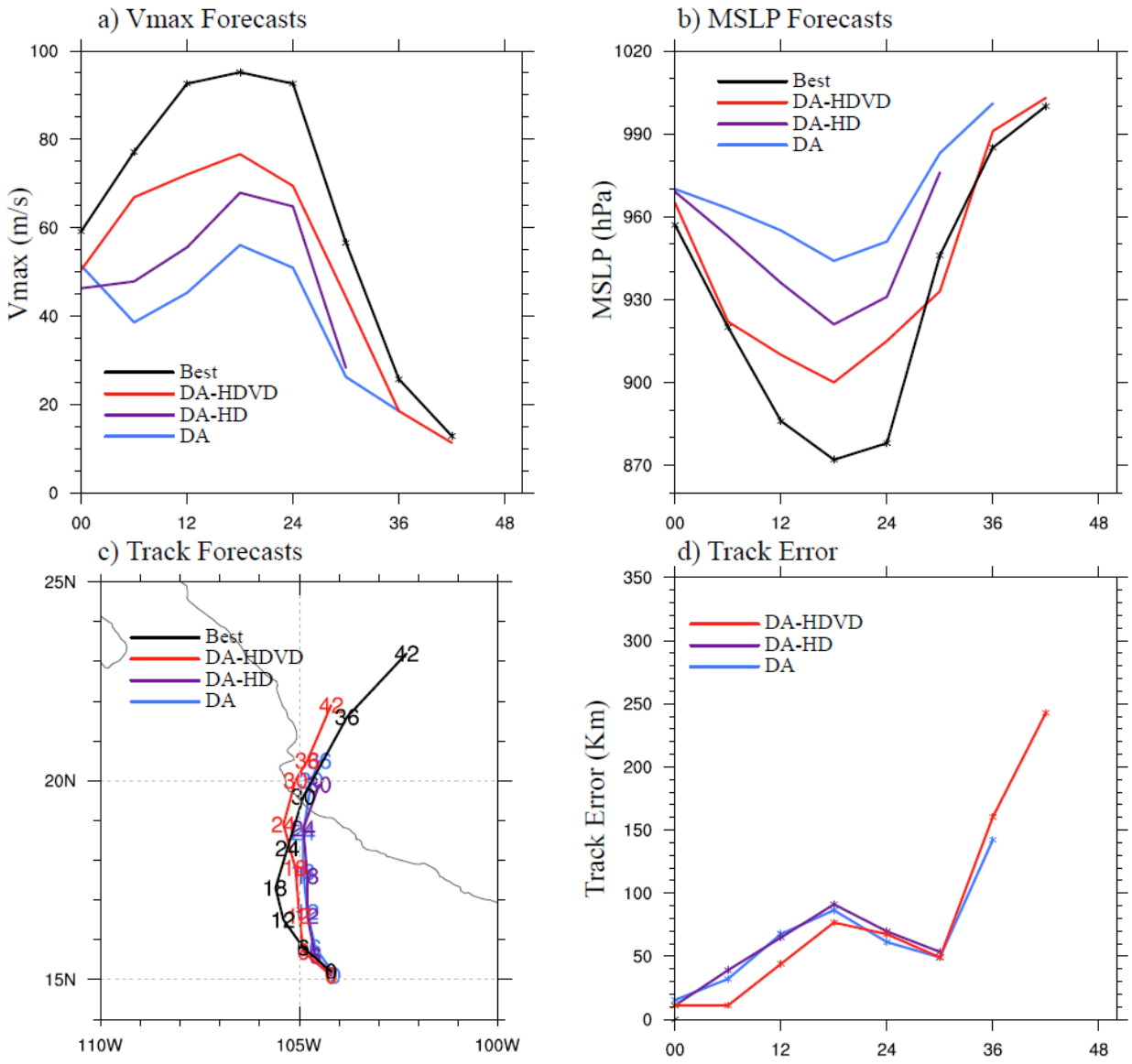

Figure 4.10 Same as Fig. 4.5 except for DA (cyan), DA-HD (purple), DA-HDVD (red) and best track (black).

Using the modified turbulent mixing parameterization scheme on top of the reduced horizontal diffusion in DA-HDVD shows further improvement in Vmax, MSLP and track forecasts upon DA-HD (Fig. 4.10a-d). The first 6-hour RI trend in DA-HDVD is now comparable with the best track and the spin-down is significantly alleviated. Specially, the peak Vmax and MSLP values in DA-HDVD is now 20 ms^{-1} larger and 44 hPa smaller than DA, respectively, more consistent with the best track. More detailed investigations on how the spin-down is alleviated with DA-HDVD will be presented in the next subsection 4.4.2.

In general, this subsection confirms the hypothesis proposed at the end of Section 4.3.2: improved model physics are needed to support and maintain the realistically analyzed TC structure from DA during the forecast. For the Patricia forecast in particular, both the modified turbulent mixing parameterization scheme and the reduced horizontal diffusion are important for improving the intensity forecast initialized from an improved analysis.

4.4.2 How can the modified model physics parameterizations alleviate spin-down?

To further understand how the improved model physics can alleviate the spin-down issue, detailed diagnostics similar to Section 4.3.2 are performed in this subsection for the best performing DA-HDVD experiment.

First of all, the frequent output of Vmax and MSLP in Fig. 4.6a-b shows that although alleviated and is not found in the 6-hour frequency output, DA-HDVD still suffers from a Vmax drop of about 12 ms^{-1} within the first hour. However, this Vmax drop in DA-HDVD is 25% smaller than DA, and DA-HDVD intensifies rapidly and consistently after the first hour of adjustment. The RI in DA-HDVD after hour 1 compensates the Vmax drop and restores the Vmax to the initial value around hour 2. The Vmax in DA-HDVD keeps growing afterward. Consistent with the Vmax evolution, the MSLP evolution in DA-HDVD shows smaller magnitude of adjustments as compared with DA in the first hour and is followed by a steady intensification afterward.

The secondary circulation evolution of DA-HDVD (Fig. 4.7u-y) shows that the vertical sub-/super-gradient oscillation in the eyewall is still not well supported during the first several minutes of model integration. However, the issue is less significant and less persistent due to the reduced horizontal diffusion. At the end of hour one, there is a clear outward updraft that connects the low-level inflow and realistically elevated upper-level outflow (Fig. 4.7y).

Consistently, Fig. 4.8e shows that the eyewall can be built up quickly in DA-HDVD and well maintained during the evolution. The 500hPa radius of eyewall in DA-HDVD is comparable with or even slightly smaller than the RMW given by the best track. The enhanced updraft is likely to be a result of applying the modified turbulent mixing parameterization scheme. Elimination of the vertical diffusion discontinuity in the new parameterization scheme (Fig. 4.1) facilitates the vertical communication of heat and moisture. Consequently, no localized low-level total condensate maximum is found in Fig. 4.9p-t, which suggests that the hydrometeors are well mixed in the eyewall region and can release more latent heat in the eyewall (Fig. 4.9t), and eventually enhanced the secondary circulation. As discussed in Section 4.3.2, the NMASPT is calculated for DA-HDVD as well. Fig. 4.6c shows that consistent with the spin-down alleviation, DA-HDVD reduces the model-analysis incompatibility as compared to DA.

Overall, comparisons from Fig. 4.6 to Fig. 4.9 suggest that the spin-down issue in Patricia is likely to be a consequence of the conflict between the unrealistic model physics parameterization and the more realistic DA analysis as hypothesized in Section 4.3.2. Reducing the confliction by either using an unrealistic but model generated analysis as VM or using a more realistically improved model physics parameterization can help alleviate the spin-down issue. However, there is still more incompatibility in DA-HDVD in comparison with VM (Fig. 4.6c) and DA-HDVD do still suffer from the short-term Vmax drop. These results suggest that further tunings and investigations in the model physics and further improvement of the DA are needed in the future.

4.5 How does model resolution impact on the TC intensity forecast?

As shown in Section 4.4, the improved model physics parameterization can help alleviate the spin-down issue and improve the TC intensity forecast significantly. However, the forecasted

maximum peak intensity is still about 20 ms^{-1} or 30 hPa weaker than the peak Vmax or MSLP recorded by the best track. This remaining gap between the two peak intensities is likely due to the insufficient model resolution considering the small size of Patricia as stated in Section 4.1. Therefore, an experiment has been conducted in this study to investigate the impact of model resolution on the peak intensity as well as the spin-down issue.

Similar to Fig. 4.5, the Vmax, MSLP and track forecasts of the model resolution experiments are verified against the best track in Figure 4.11. Without changing the model physics parameterization configuration, DA-Hi shows slightly alleviated Vmax spin-down and a significant improvement in the peak intensity in comparison with DA. However, this spin-down alleviation through the resolution increase is not as significant as the model physics parameterization improvement. This result suggests the spin-down is largely attributed to the model physics errors rather than the relatively coarse model resolution. While the peak intensity is improved in DA-Hi as compared to DA, the track forecast is somehow degraded because the predicted TC moves too fast. Specifically, DA-Hi makes landfall after hour 18 while the best track shows landfall close to hour 30.

Since the spin-down is already alleviated in DA-HDVD, increasing model resolution with the improved model physics in DA-HDVDHi shows significantly more improvement in the intensification rate and peak intensity. Although the timing is shifted 6 hours earlier, the peak Vmax in DA-HDVDHi is now comparable with the best track. The early peak intensity in DA-HDVDHi is also due to the over-fast prediction of track similar to DA-Hi (Fig. 4.11c-d).

Altogether, Fig. 4.11 suggests that the model resolution can be an important factor for maximum peak intensity prediction for HWRF model when the model physics are properly

modified, but the model resolution is not as important as the model physics in the spin-down alleviation for this case.

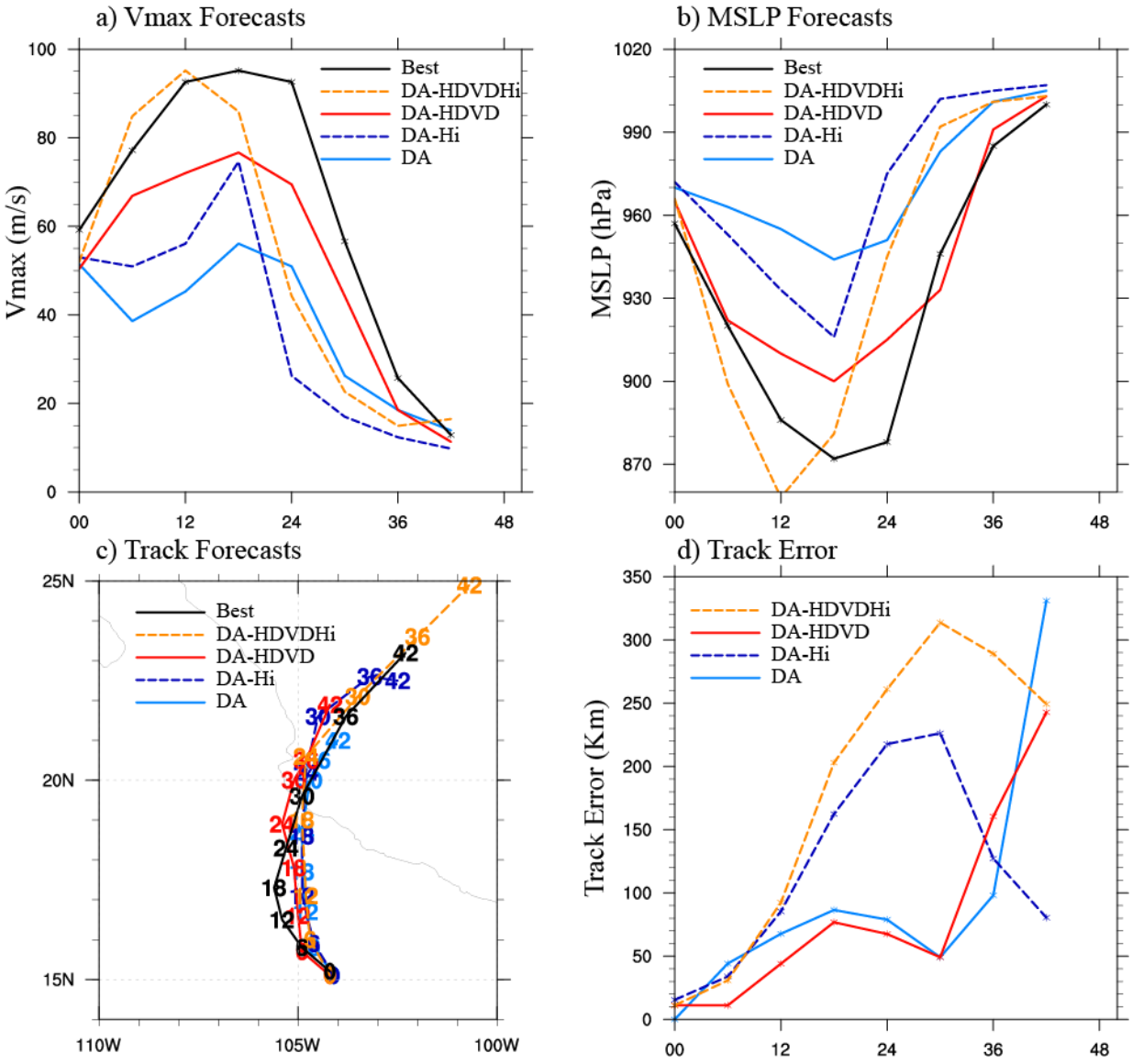

Figure 4.11 Same as Fig. 4.5 except for DA (solid cyan), DA-Hi (dashed blue), DA-HDVD (solid red), DA-HDVDHi (dashed orange) and best track (solid black).

4.6 Summary and Discussions

A newly developed GSI-based, continuously cycled, dual-resolution hybrid EnKF-Var DA system for HWRF (Lu et al. 2017b) is upgraded to be consistent with the 2015 operational

HWRF at a higher model resolution. Using this upgraded system, abundant field campaign inner-core and near inner-core observations together with the enhanced CIMSS AMVs collected during Hurricane Patricia (2015) are assimilated to provide a realistic 3D analysis of the storm. As the second part of the dissertation, this chapter aims at investigating the source of the spin-down issue associated with the more realistic DA analysis. Diagnostics have shown that the analysis is consistent with various observations. Additionally, the analysis produced by DA is more consistent with the GWB and unbalanced force theories. In contrast, VM creates a spuriously strong super-gradient imbalance throughout the inner-core to near inner-core region. However, the realistic analysis produced by DA is found to experience significant and persistent Vmax spin-down (e.g. Vmax drop lasts longer than 6 hours) which jeopardizes the subsequent intensity forecast. On the other hand, the spurious analysis produced through VM is found to produce better intensity forecast without apparent long-lasting Vmax drop. Therefore, diagnostics are performed in this study to understand why the more persistent spin-down occur when initialized with the more realistic DA analysis but not with the spurious VM analysis.

Frequent outputs from HWRF model show that Vmax drop happens in both DA and VM. The Vmax drop in VM is attributed to the significant wind and pressure adjustment caused by the super-gradient imbalance at the initial time. This model adjustment in VM is significant but brief. Vmax is recovered to the strength of the analysis quickly and slowly intensifies afterward. However, the Vmax drop in DA is more severe and persistent than the Vmax drop in VM. The evolution of secondary circulation and eyewall indicates that this significant Vmax drop in DA is attributed to the defective model physics parameterization schemes that cannot maintain the realistic sub-/super-gradient oscillations associated inflow/outflow oscillations around the eyewall. Additionally, the realistically elevated upper-level outflow by DA is also not supported

by the model due to the unrealistically weak secondary circulation even after the model resumes its balance. It is hypothesized from these results that better HWRF model physics such as the turbulent horizontal and vertical diffusion parameterizations are needed to alleviate the spin-down initialized by the analysis produced by DA.

Further diagnostics with modified model turbulent diffusion parameterizations are therefore conducted in this study to investigate the hypothesis. Results show that using a reduced horizontal diffusion parameterization configuration is able to better maintain the sub-/super-gradient oscillation from the DA analysis and therefore significantly alleviated the spin-down issue. Further applying the modified turbulent mixing parameterization scheme with improved vertical diffusion profile significantly increased the intensification rate and peak intensity with enhanced secondary circulation. However, it should be noted that this study is not trying to suggest that the reduction in the horizontal diffusion or the change of vertical diffusion profile is a final resort to resolve the spin-down issue. Rather, the experiments conducted in this study demonstrate that the model physics do play an important role in the spin-down alleviation and a realistic DA analysis requires a compatible, realistic model physics to improve the TC intensity forecast.

Considering the small size of Patricia, some initial experiments are also conducted in this study to investigate the impacts of increased model resolution in the intensity forecast. Results show that by increasing the model resolution, the spin-down issue can be alleviated and the intensification rate and therefore peak intensity can be increased significantly. However, the spin-down alleviation from the resolution increase is not as significant as the alleviation from the model physics modification. These results suggest that the model resolution is one key factor that limits the intensification rate and peak intensity, but the model physics plays a more

important role in the spin-down alleviation in this case. Additionally, the predicted TC moves overly fast with the finer resolution experiments, which requires further investigations in the future work. In Chapter 5, the impact of various field campaign and enhanced CIMSS AMV observations on the analysis and subsequent forecast of Patricia using the improved physics are discussed. This study focuses on the Vmax spin-down with a time scale of 6 hours or more, based on definition of spin-down from early studies (Bernardet et al. 2015; Zhou et al. 2015a,b; Tong et al. 2018). The Vmax drop at a much shorter time scale, e.g. over the first 10-20 minutes shown in Fig. 4.6a, is worth additional investigation in future studies.

Chapter 5: Observation Impacts on the Analysis and Prediction of Patricia (2015)

5.1 Introduction

Hurricanes are difficult to observe over the open ocean, especially their inner-core regions. Due to heavy cloud and precipitation, utilization of all-sky satellite radiances is still a challenge and the corresponding research for Tropical Cyclone (TC) predictions are just beginning (Bauer et al. 2010, 2011; Yang et al. 2016; Zhang et al. 2016; Zhu et al. 2016; Geer et al. 2017). Therefore, data collected by the manned or unmanned aircraft penetrating hurricanes becomes one of the few options for hurricane inner-core studies (Marks and Houze 1984, 1987; Gamache et al. 1993; Reasor et al. 2000; Xiao et al. 2009; Zhang et al. 2009a, 2011; Weng and Zhang 2012; Aksoy et al. 2013; Lu et al. 2017a,b). These aircraft are usually supported by different field campaign programs.

Starting from 2005, an Intensity Forecasting Experiment (IFEX) program was conducted by the National Oceanic and Atmospheric Administration (NOAA). In this multiyear experiment, observations such as Stepped Frequency Microwave Radiometer (SFMR), flight-level (FL) and tail doppler radar (TDR) observations were collected through the NOAA WP-3D aircraft (Rogers et al. 2006, 2013a). The different observations primarily focus on the inner-core structures of hurricanes at various levels. For example, the SFMR samples only the surface, the FL observations are usually centered around 700 hPa to 800 hPa, and the TDR scans three-dimensional (3D) structures with the number of observations peaked around 900 hPa (e.g. Fig. 5.1c).

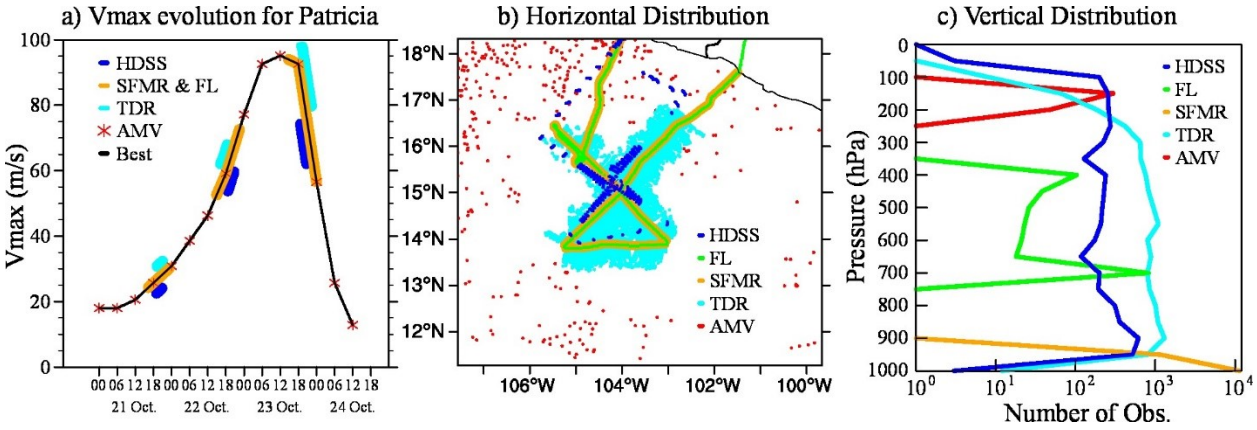

Figure 5.1 An example of the (a) Temporal, (b) horizontal and (c) vertical distribution of the observations. (b) and (c) are the wind observations assimilated in the innermost domain valid at 1800 UTC 22 Oct 2015 during Patricia. Best is short for the best track data form NHC. Note, the x-axis in Fig. 5.1c is in log space.

These observations collected from the IFEX field campaign have been widely used in hurricane research for decades. For instance, the SFMR wind observations are commonly used to validate or estimate the maximum surface wind speed (Vmax) for hurricanes (e.g.: Uhlhorn and Black 2003; Uhlhorn et al. 2007; Powell et al. 2009; Weng and Zhang 2012). The FL observations are often used for the estimation of TC center and the validation of simulated TC inner-core structure (Aksoy et al. 2013; Rogers and Uhlhorn 2008b; Willoughby and Chelmow 1982; Willoughby and Rahn 2004; Chen et al. 2011). The TDR radial velocity observations are extensively used for hurricane inner-core data assimilation (DA), and extensive studies have demonstrated the potential of high-resolution inner-core observations in improving high-resolution hurricane predictions using advanced DA methods (e.g.: Zhang et al. 2009, 2011; Weng and Zhang 2012; Poterjoy et al. 2014; Zhang and Weng 2015; Pu et al. 2016; Lu et al. 2017a,b).

In 2015, a Tropical Cyclone Intensity (TCI) program supported by the Office of Naval Research (ONR) was conducted to collect dropsonde observations aiming at sampling the TC outflow as well as the inner-core regions (Doyle et al. 2017). These dropsondes were released by WB-57 from about the 18-km altitude and sampled all the way down to sea surface. The high

altitude of the aircraft provided valuable opportunities to sample upper-tropospheric information, especially for the TC outflow region. Thanks to the High Definition Sounding System (HDSS) and eXpendable Digital Dropsonde (XDD) technology (Black et al. 2017), these dropsonde observations have unprecedentedly high vertical spacing (~0.1-hPa) (Bell et al. 2016). Given tens of dropsondes were deployed within a small time-window, the finest horizontal transection spacing of the dropsondes near the inner-core regions of the TCs can be around 4.4-km (Doyle et al. 2017). Dropsondes with such a high resolution provide a great sampling of both the inner-core and the outflow structures. But due to the novelty of the dataset, there are only a few studies exploring their applications in the hurricane analysis and prediction (e.g. Feng and Wang, 2019; Zhang and Pu, 2019).

Other than those field campaign observations, in recent years, the "enhanced" Atmospheric Motion Vector (AMV) observations have been produced by the Cooperative Institute for Meteorological Satellite Studies (CIMSS) (Wu et al. 2014, 2015; Velden et al. 2017). The CIMSS AMVs are designed to have higher density, larger coverage and better quality as compared to the operationally produced AMVs provided by the National Environmental Satellite, Data, and Information Service (NESDIS) (Velden et al. 2017). These CIMSS AMVs can provide upper-level environmental information of the TCs (e.g. Fig. 5.1). Previous studies suggested that assimilating the CIMSS AMVs can modestly improve hurricane track and intensity predictions (Wu et al. 2014, 2015; Velden et al. 2017).

The aforementioned observations each provides sampling of certain aspects of the TC structure including the inner-core, the outflow layer, the surface inflow and the environment flow. Co-existence of all these types of observations for the same hurricane and at the same time is rare. Therefore, most early studies only revealed impacts of one type of observations or only

simultaneously compared the impacts of a limited sub-sets of these observations (Weng and Zhang 2012; Aksoy et al. 2012, 2013; Poterjoy et al. 2014; Wu et al., 2014, 2015; Lu et al. 2017a). Fortunately, through coordination between the IFEX and TCI field campaigns, hurricane Patricia (2015) became the sole hurricane which was intensively and simultaneously sampled by all the above-mentioned instruments. This provides an unprecedented opportunity to reveal and inter-compare the impacts of all these types of observations. To the authors' best knowledge, this work is the first data assimilation study that reveals the relative impacts of all these types of observations on the analysis and prediction in the same hurricane. In addition, the simultaneous availability of these observations also provides a good opportunity to cross-validate the analysis after assimilating each type of observations.

To make a good use of the observations, an efficient and advanced DA system is required. A GSI-based, continuously cycled, dual-resolution, hybrid Ensemble-Variational (EnVar) DA system for Hurricane Weather Research and Forecast (HWRF) was recently developed (Lu et al. 2017a,b) expanded from the same hybrid DA system for the operational global forecast system (Wang et al. 2013). It was shown that the new system can improve both the track and intensity predictions upon the operational HWRF. In Chapter 4, experiments were conducted to investigate the impact of model physics and model resolution on the spin-down issue during Hurricane Patricia (2015). Results indicated that assimilating the aforementioned observations altogether using the new system and modified model physics, the 3D structures of Patricia were realistically captured in the analysis. In addition, the realistic TC structure from the DA analysis was well maintained during the forecast, evidenced by the improved subsequent forecast of rapid intensification (RI) of Patricia (2015). Therefore, in this part of the study, the same system and model configurations will be used to investigate the relative impacts of these diverse observation

types on the analysis and prediction of Patricia (2015). Since this is only a case study with limited sample size, the primary goal of this study is to improve the physical understanding of the relative importance of each observation type, and to suggest future directions for additional studies.

As the second part of the two-part study, we first briefly describe the model, the observations and experiment designs in Section 5.2. Section 5.3 discusses the results of the impacts of various observations on the analysis and prediction of Patricia. Section 5.4 concludes and further discusses the results.

5.2 Model, Data and Experiment Design

5.2.1 Model description

Table 5.1 List of experiments and their descriptions.

Experiment name	Common Features	Description
NoDA	**Background**: 6-hour control forecast initialized from 1200 UTC 22 October 2015 using the GSI-based, continuously cycled, dual-resolution hybrid ensemble-variational (EnVar) DA system for HWRF (Lu et al., 2017b) valid at 1800 UTC 22 October 2015. **Physics**: Ferrier-Aligo microphysics scheme; simplified Arakawa-Schubert (SAS) cumulus scheme; HWRF modified surface layer scheme; Noah land surface model; HWRF PBL scheme; RRTMG longwave and shortwave radiation schemes; Reduced "Coac" (horizontal diffusion weight) from 0.75/3.0/4.0 to 0.75/1.0/1.2; Modified turbulent mixing parameterization.	No DA is performed
OperH		Conventional in-situ data in prepbufr (Radiosondes; Dropwindsondes; Aircraft Reports; Surface Ship and Buoy Observations; Surface Observations over Land; Pibal Winds; Wind Profilers; Radar-derived Velocity Azimuth Display Wind; WindSat Scatterometer Winds; Integrated Precipitable Water derived from the Global Positioning System), tcvital, EMC AMVs and satellite radiances (from HIRS, AIRS, IASI, GOES, AMSU-A, MHS and ATMS). Note, the satellite radiances are only assimilated in the intermediate domain following the operational configuration.
CIMSS_Only		Only CIMSS AMVs are assimilated
SFMR_Only		Only SFMR observations are assimilated
FL_Only		Only flight-level observations are assimilated
TDR_Only		Only TDR are assimilated
HDSS_Only		Only HDSS dropsodes from TCI are assimilated
All		Conventional in-situ data in prepbufr, tcvital, TDR, SFMR and flight-level observations, HDSS dropsodes from TCI, CIMSS AMVs and satellite radiances

The GSI-based, continuously cycled, dual-resolution, hybrid EnVar DA system for HWRF (Lu et al. 2017b) is used in this study as a tool to investigate the observation impacts on the analysis and prediction of Patricia. As stated in Chapter 4, this upgraded DA system is based on the 2015 operational HWRF (H215). One major difference between the new DA system and the DA system in the H215 is the source of ensemble covariances. Specifically, a continuously cycled HWRF ensemble consistent with the intermediate domain resolution of the control (e.g. 6-km grid spacing in this study) is used to provide ensemble background covariances in the 3DEnVar DA replacing the coarser resolution GFS ensemble. Further details about the new DA system and workflow can be found in Chapter 4.2.1.

The horizontal grid-spacing of the model is approximately 2-km (0.015 degrees), 6-km (0.045 degrees) and 18-km (0.135 degrees) for the innermost (265×472 grid points), intermediate (304×604 grid points) and outermost (288×576 grid points) domains, respectively. The model is configured with 61 vertical levels and the model top is at 2 hPa. The initial and boundary conditions for the outermost domain are obtained from the GFS analyses and forecasts. The choice of model physics parameterization schemes follows the H215 (Tallapragada et al. 2015) with modifications in the vertical and horizontal diffusion parameterizations (Table 5.1). Briefly, the in-cloud turbulent mixing parameterization in the PBL scheme proposed by Zhu et al. (2018) is adopted to enable the in-cloud mixing for the eyewall and rainband regions. The horizontal diffusion is reduced to be more consistent with the 2-km model grid-spacing as suggested by Zhang et al. (2018). As discussed in Chapter 4, the modified suite of model physics was able to better maintain the realistically analyzed TC structure and largely alleviate the Vmax spin down issue. The spin-down is a short-term but significant Vmax drop due to the incompatibility between the realistic DA analysis and inaccurate model physics (Lu and Wang

2019a). Additional experiments (not shown) without the model physics modifications did not change the relative data impacts, although most of those experiments suffered from the spin-down issue.

5.2.2 Observations and preprocessing

As introduced in Section 5.1, there are five special types of observations that are assimilated in this study: CIMSS AMV wind; SFMR surface wind speed; FL temperature, moisture and wind; TDR radial velocity; and HDSS dropsonde temperature, moisture and wind. Further information, descriptions and preprocessing applied for each type of observations are described below.

The CIMSS AMV observations used in this study are derived from the Geostationary Operational Environmental Satellite (GOES) by CIMSS. Following Wu et al. (2014), the CIMSS AMVs are quality controlled and superobbed before being assimilated by the DA system. Specifically, only the CIMSS AMVs with quality indices no less than 0.6 and expected error lower than 4.5 ms^{-1}, or the observations greater than 25 ms^{-1} with quality indices no less than 0.7 are assimilated. The superob prisms are configured to be $0.1° \times 0.1° \times 15$ hPa, and the CIMSS AMVs are averaged with equal weight within each prism. The observation errors for the CIMSS AMVs range from 2.5 ms^{-1} to 7 ms^{-1} depending on the pressure level at which the observations are located.

The SFMR, FL, and TDR observations assimilated in this study are collected by the NOAA WP-3D aircraft during the IFEX field campaign. The SFMR equipment has been onboard NOAA WP-3D aircraft since 1984 (Uhlhorn and Black 2003) and redesigned since 2004 (Uhlhorn et al. 2007). In this study, the SFMR wind observations are obtained from Hurricane Research Division (HRD, 2015), and are superobbed before the assimilation. The horizontal

dimension of the superob prism is configured to be 0.03°×0.03°, and the observation error is set to be 5 ms^{-1}. The FL observations, including wind, temperature and moisture observations, have been synthetically sampled by multiple instruments onboard the NOAA WP-3D aircraft for decades (Friedman 1982, 1984). In this study, the FL observations are directly obtained from the National Weather Service (NWS) data pool. The horizontal data resolution is about 3~5-km and therefore no further thinning or superobbing is performed. The observation errors are about 5.5 ms^{-1}, 2.5 K and 2.5 $kgkg^{-1}$ for the wind, temperature and specific humidity, respectively. Due to data transfer issue, the TDR data was not available in the operational HWRF before 23 October 2015 during the real time forecast of hurricane Patricia. The TDR data used in this study was obtained from HRD (2015). The preprocessing for the TDR radial velocity follows Gamache (2005) and Lu et al. (2017a,b), and the observation error is assigned to be 5 ms^{-1}.

The HDSS dropsondes are provided by the TCI field campaign as stated in Section 5.1. During hurricane Patricia, there are in total 257 dropsondes deployed during the four WB-57 missions between October 20 to October 23, 2015 to sample the moisture, temperature and wind profiles in the inner-core and outflow regions of Patricia. This study only focuses on the 83 dropsondes released on October 22, 2015. These HDSS dropsondes were initially quality controlled through both software and manual inspections by the TCI scientists (Bell et al. 2016). Due to the high vertical resolution of the observations, superobbing is applied to reduce the data density. After some initial trials (not shown), the superobbed prisms are roughly chosen to be about 2 times the model grid-spacing, specifically, about 0.04°×0.04° (roughly 4-km×4-km) in the horizontal and every other model level (e.g. about 10 hPa near 1-km height) in the vertical in this study. The observations within each prism are averaged with equal weights. The observation errors used for the HDSS dropsondes range from 2.5 ms^{-1} to 5.1 ms^{-1}, and from 0.5 K

to 2 K for the wind and temperature respectively and 2 $kgkg^{-1}$ for the specific humidity. In this study, the diagnostics and verifications are based on these superobbed dropsonde observations. Further sensitivity experiments on the optimal data preprocessing approach in the HDSS dropsondes will be presented in a forthcoming study.

5.2.3 Experiment Design

For Patricia, there are only 3 DA cycles that all the IFEX, TCI and CIMSS AMV observations are simultaneously available (Fig. 5.1a). This study only focuses on the cycle on October 22, 2015 for the following reasons. First, October 23 is not considered because we are mostly interested in the analysis and prediction of the RI phase of Patricia. October 21 was not selected because the actual TCI WB57 flights deviated from the original plan. The deviation makes the actual WB57 flight tracks have undesirably little overlap with the IFEX WP-3D flight track in the horizontal direction when both sample the inner core region. For example, on October 21, the flight pattern from WB-57 missed the southern portions of the storm while the WP-3D captured it (not shown). Such a difference complicates the interpretation of the impact of the data on the inner core analysis. In comparison, the October 22 cycle has similar flight patterns in the inner-core region between the IFEX and TCI field campaigns. This cycle was then selected to aid in addressing the scientific objectives of the study.

To understand the relative impact of each individual observation type on the TC analysis and prediction, eight experiments denoted as "NoDA", "OperH", "HDSS_Only", "TDR_Only", "FL_Only", "SFMR_Only", "CIMSS_Only" and "All" are conducted (see descriptions in Table 5.1). Details for each experiment are described as below.

Experiment NoDA is initialized from a relocated control background forecast valid at 1800 UTC 22 October 2015 from the newly upgraded hybrid DA system with modified model

physics. The model physics are modified from the previous cycle starting from 1200 UTC 22 October 2015. There were seven DA and forecast cycles performed ahead every 6 hours starting from 1800 UTC 20 October 2015 using the cycled DA system with only the operational HWRF observations assimilated and the physics configurations comparable to the 2015 operational HWRF. The configuration and design of NoDA in this study are identical to experiment "NoDA" in Chapter 4, except the modified model physics. No vortex modification (VM) is performed but the vortex relocation (VR) is kept at the TDR-available cycle prior to DA following Lu et al. 2017b. Note that some preliminary diagnostics of this study were included in the Fig. 15 of Doyle et al. (2017). However, those preliminary diagnostics were conducted without the physics parameterization improvement and were shown at different levels, and therefore differ from Fig. 5.2 and Fig. 5.3 in this study.

To provide a reference to reveal the impact of other specially collected observations, experiment OperH is conducted to assimilate observations from the operational HWRF data stream based on NoDA. The details about the observations assimilated in OperH are described in Table 5.1. Note, as indicated in Section 5.2.2, no TDR data is assimilated in the operational HWRF at 1800 UTC 22 October 2015 during hurricane Patricia, and the clear-air satellite radiance observations are only assimilated in the intermediate domain. Therefore, the inner-core information in OperH is only provided by a few dropsondes in the lower troposphere launched from WP-3D aircraft and TCVital MSLP. Note that the analysis by this OperH experiment is different from that generated by the operational HWRF. In addition to the system differences mentioned in Section 5.2.1, the operational HWRF performs VM before the assimilation whereas this study does not.

Compared to NoDA, CIMSS_Only, SFMR_Only, FL_Only, TDR_Only and HDSS_Only are experiments where the corresponding individual type of observations is assimilated, respectively. Inter-comparison among these experiments, NoDA and OperH reveals the data impact of each individual observation type.

Experiment All assimilates all types of observations listed above based on NoDA. This experiment is conducted to reveal the impact of combining all types of observations. Note that experiment All is identical to experiment "DA-HDVD" in Chapter 4.

5.3 Results

5.3.1 Evolution of Patricia observed from various platforms

As shown in Fig. 5.1a, Patricia became a tropical storm around 0000 UTC 21 October 2015 and started its RI on 22 October. After reaching the peak intensity around 1200 UTC 23 October, Patricia rapidly weakened and made landfall around 2300 UTC 23 October. This study primarily focuses on the RI evolution of Patricia between 1800 UTC 22 and 1800 UTC 23 October. The structural evolution of Patricia observed from various platforms during this period is first briefly discussed in this subsection.

At 1800 UTC 22 October 2015, Patricia was a small-sized, category 4 hurricane. The Vmax was 59 ms^{-1} and the radius of maximum wind (RMW) was about 18-km. Such a strong Vmax in the northeast (NE) quadrant of Patricia and the small RMW were well captured by the SFMR observations (Figure 5.2a). The small storm size and the wind speed maximum located in the NE quadrant were also consistently found in the FL and TDR observations (e.g. Figure 5.3a). A southeast-northwest (SE-NW) cross-section of the radial wind patterns derived from the HDSS dropsondes shows that Patricia was dominated by inflow (blue colors) in the SE section of the low-level and was dominated by outflow (red colors) in the NW section (Fig. 5.4a). Other than

the cross-sections, the environmental wind (outside the 150-km radius of the storm) sampled by the CIMSS AMVs was also available. Given the peak number of observations (Fig. 5.1c)[10], the corresponding radial flow patterns derived from the CIMSS AMVs at 150 hPa are shown in Figure 5.5a. The environmental wind at this level was featured with outflow except the east (E) to SE portion. Besides the dynamic structures, the thermodynamic structures were also sampled from the HDSS dropsondes. For instance, the corresponding temperature anomaly in the SE-NW cross-section is shown in Figure 5.6a. The Jordan annual mean profile (Jordan 1958) is used as the environmental sounding during the anomaly calculation. At this time, there were two warm anomaly maxima in the eye region for this cross-section: one stronger upper-level warm-core (UWC) centered between 200~250 hPa, and one weaker middle-level warm-core (MWC) centered between 550~600 hPa.

[10] The AMV observations at the lower troposphere were only distributed in the intermediate domain but outside the innermost domain at this time in this study.

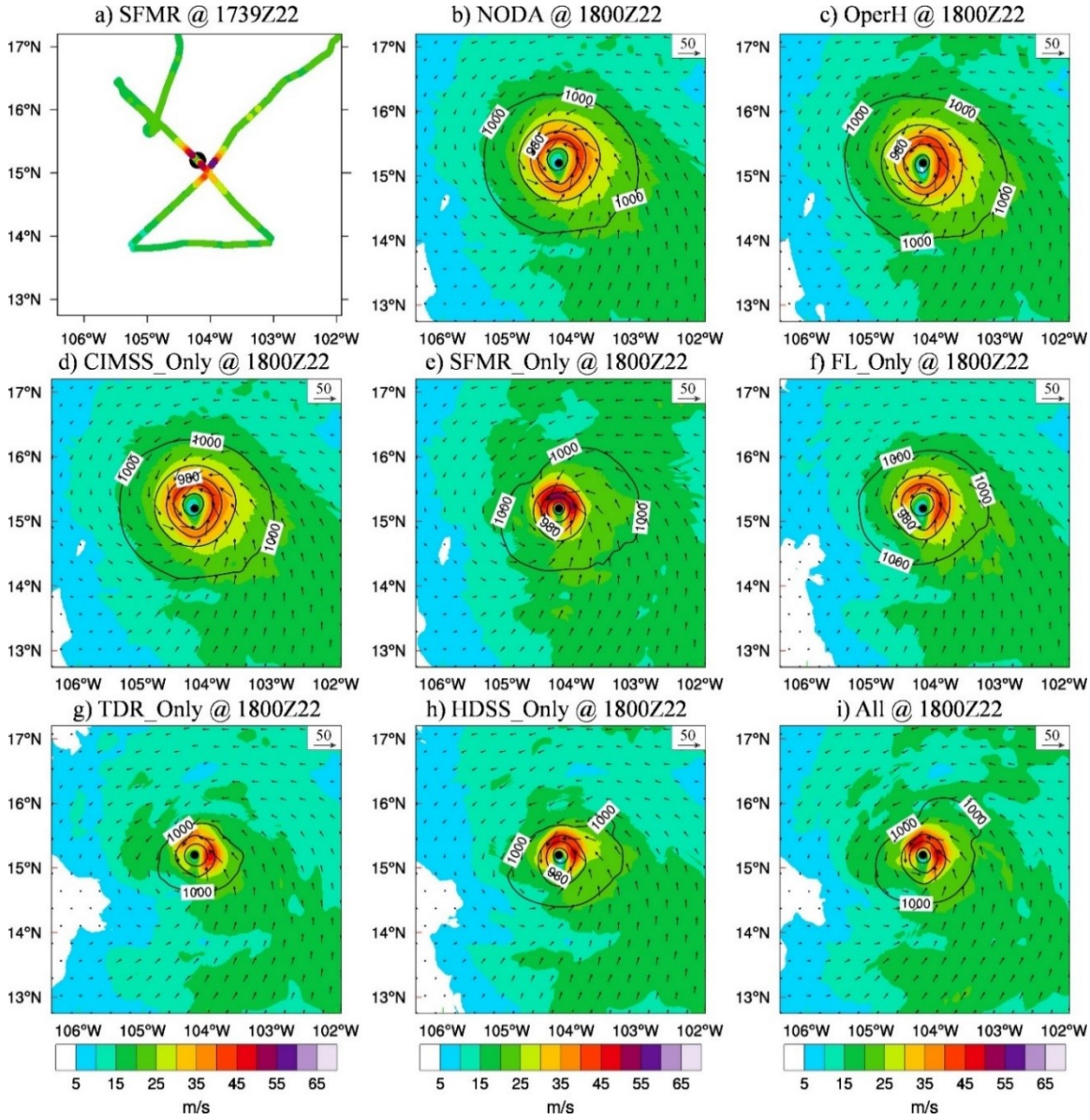

Figure 5.2 Wind (shading and vectors, m s-1) and pressure (contours, hPa) at 10-m height for (a) SFMR observations onboard NOAA P-3 aircraft centered around 1739 UTC 22 Oct 2015, (b) NoDA analysis, (c) OperH analysis, (d) CIMSS_Only analysis, (e) SFMR_Only analysis, (f) FL_Only analysis, (g) TDR_Only analysis, (h) HDSS_Only analysis and (i) All analysis valid at 1800 UTC 22 Oct 2015 during Patricia. The black dots denote the best track position valid at 1800 UTC 22 Oct 2015.

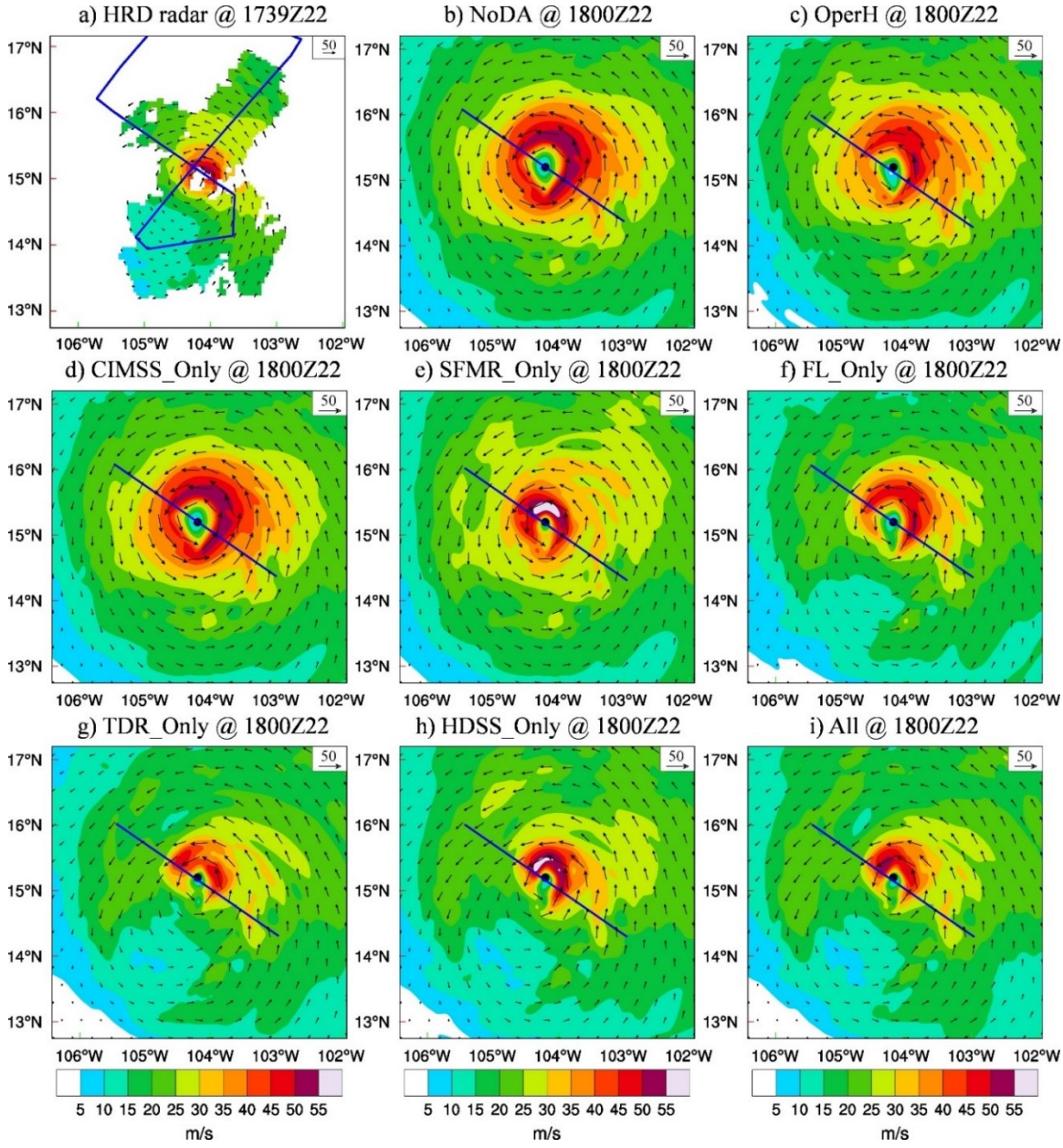

Figure 5.3 Same as Fig. 5.2 except for the 3-km horizontal wind (shading and vectors, m s^{-1}) in verification with (a) the HRD radar composite. The blue lines in (a) denote the flight track of WB-57 and the blue lines in (b)~(i) denote corresponding southeast to northwest cross-section to be plotted in Fig. 5.4 and Fig. 5.6.

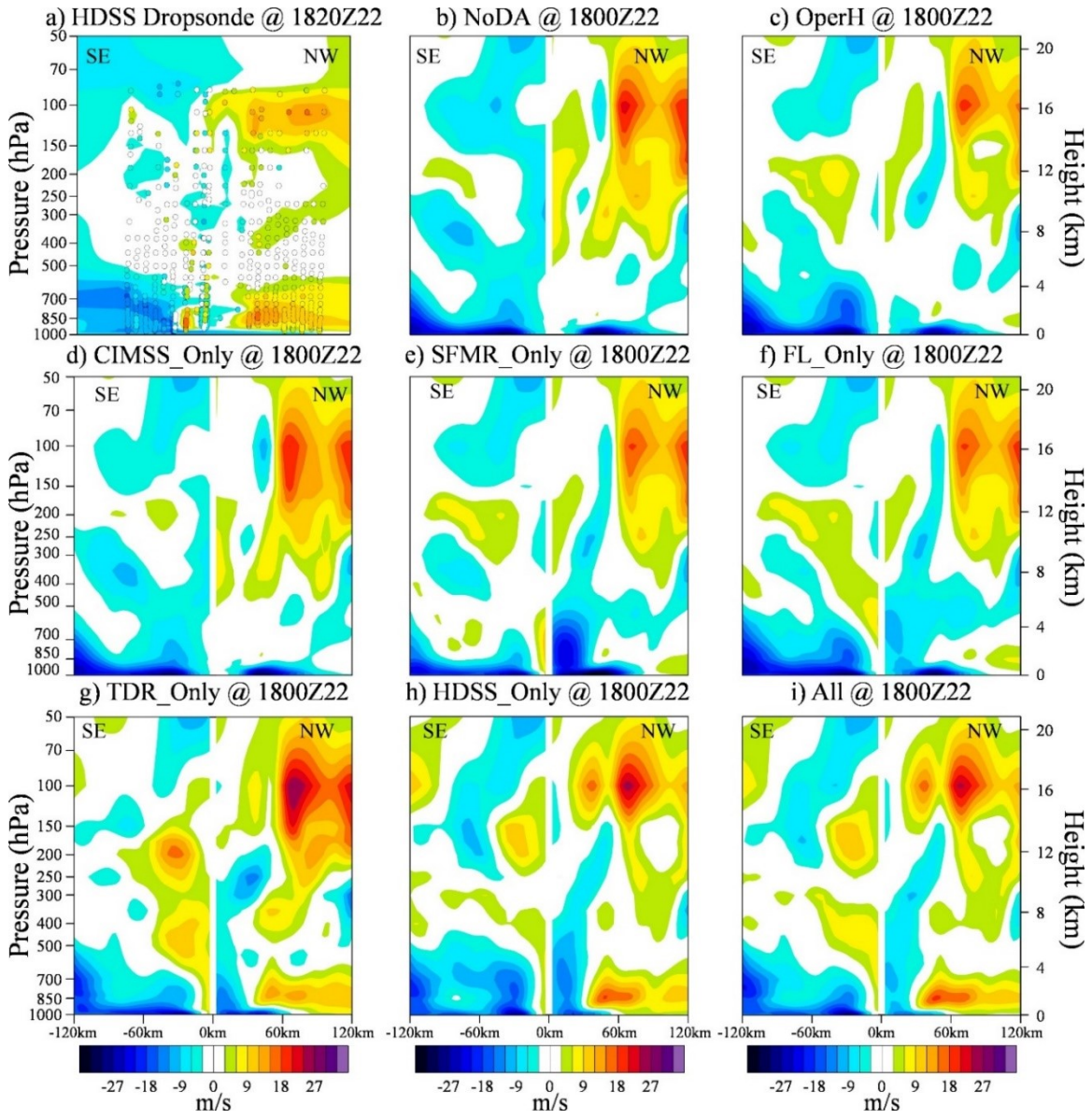

Figure 5.4 Same as Fig. 5.2 except for the Radial wind (shading, m s-1) analysis of the southeast to northwest vertical section in verification with (a) the HDSS dropsonde observations centered around 1820 UTC 22 October 2015. Positive (warm color) indicates outflow and negative (cold color) indicates inflow.

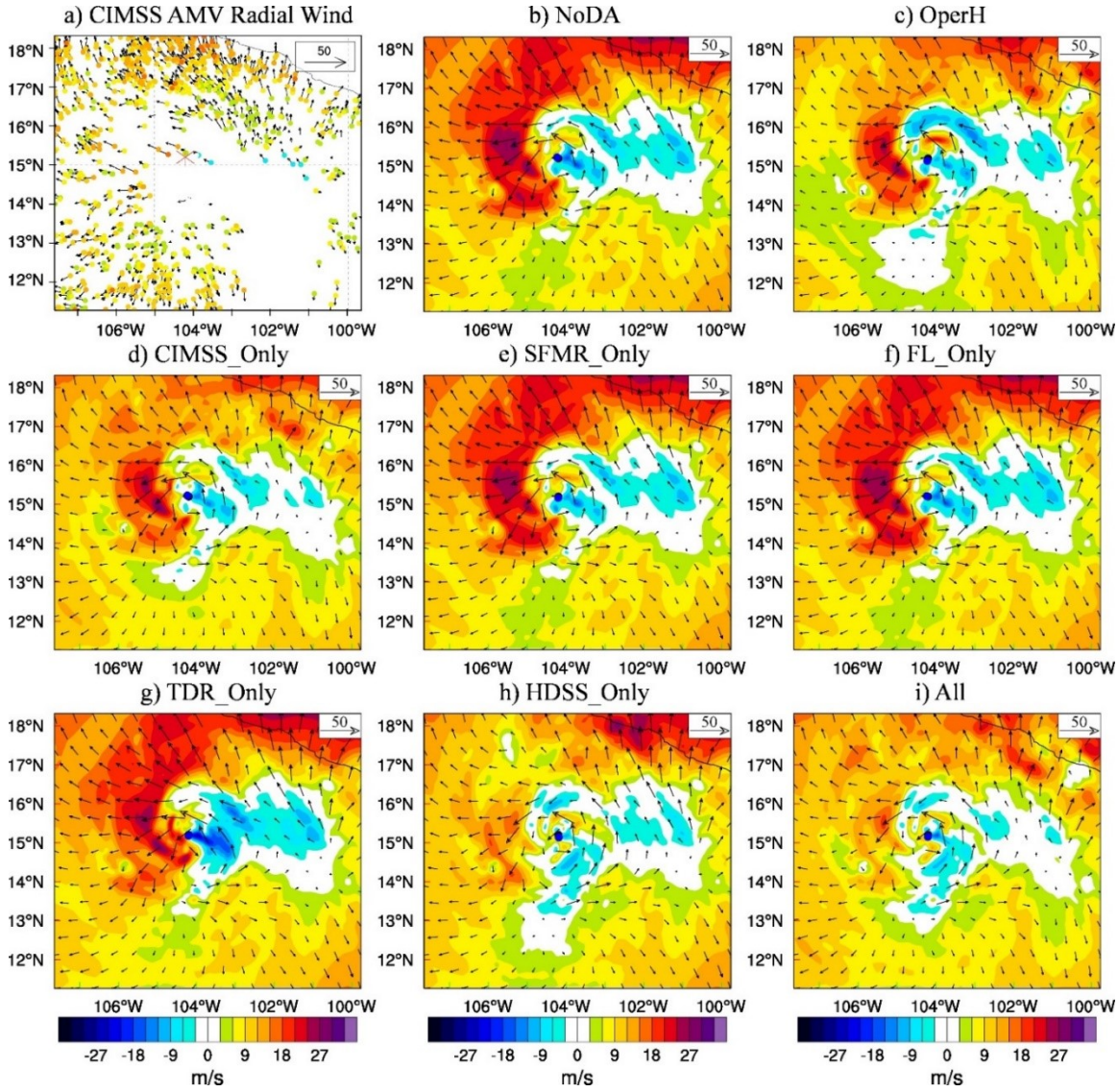

Figure 5.5 Same as Fig. 5.2 except for 150 hPa radial wind (shading, m s-1) and horizontal wind (vectors, m s-1) in verification with (a) the CIMSS AMV observations. The red star in (a) and the black dots in (b)~(i) denote the best track position and the blue dots in (b)~(i) denote the analyzed storm center at the surface. Note, the black and blue dots are very close to each other for each experiment due to the vortex relocation.

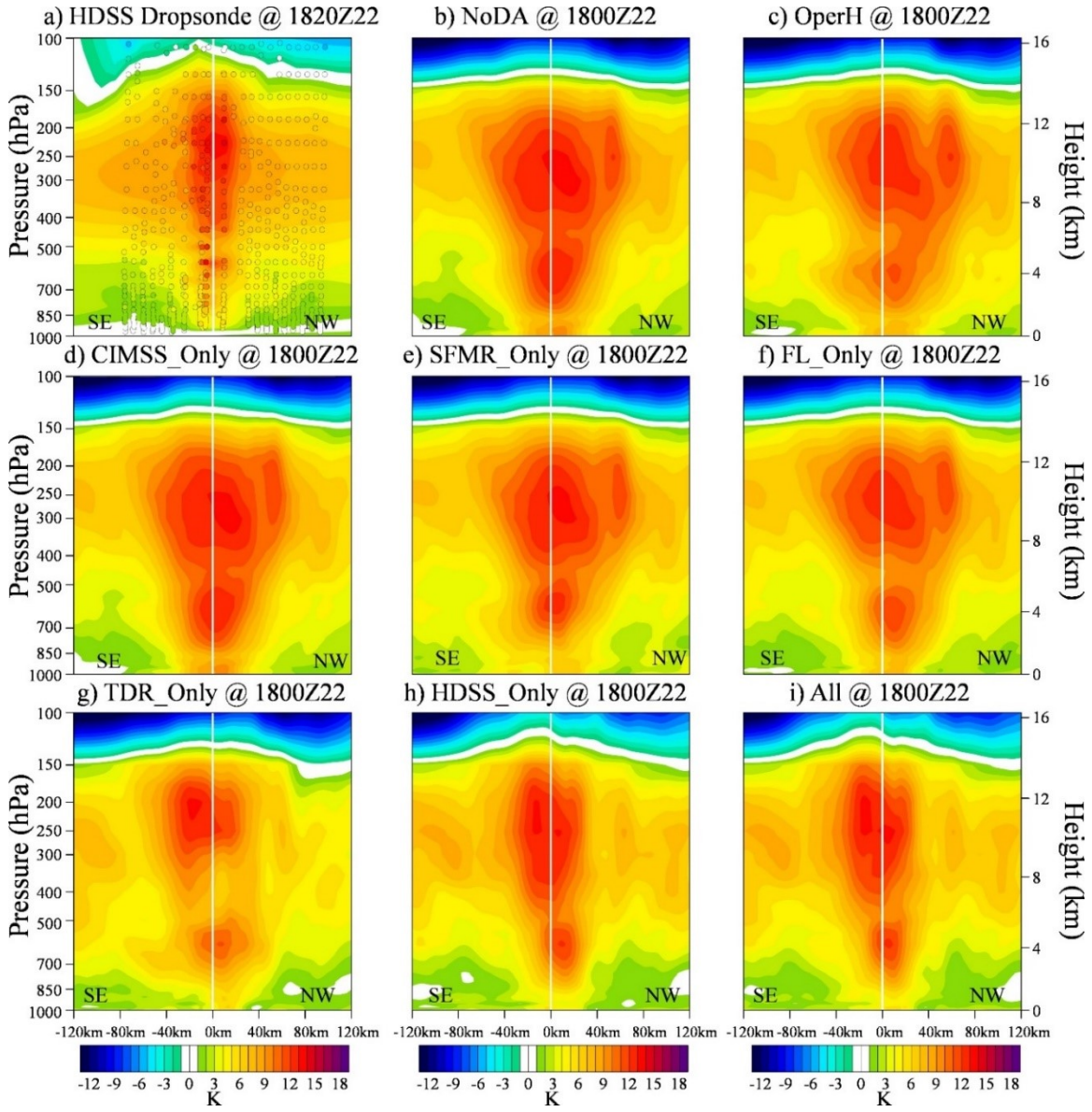

Figure 5.6 Same as Fig. 5.4 except for the warm-core anomaly analysis of the southeast to northwest vertical section in verification with (a) the HDSS dropsonde observations centered around 1820 UTC 22 October 2015. The Jordan annual mean profile is used as the environmental sounding for all experiments for consistency.

The above observations will then be used to verify the analyses at 1800 UTC 22 October 2015 produced by the various DA experiments. Since the next aircraft observations were only available at 1800 UCT 23 October, the subsequent 24-hour forecast is verified using the GOES-13 brightness temperature (BT), which is available every 15 minutes (CLASS, 2015). Forecast verification is based on band 4 (10.7 μm central wavelength), because this longwave band

retrieved the cloud-top temperature and precipitation evolution of Patricia. The BT series show that Patricia featured with a well-maintained, small and symmetric eye during the 24-hour period. According to the hurricane report from NHC (Kimberlain et al. 2016), the eye size of Patricia ranged from 13-km to 18-km during this time period. Not only the size of the eye remained small, the size of the central dense overcast (CDO) region in Patricia also remained small (diameter ranging from about 250-km to 300-km, e.g. Figure 5.7a-5.8a).

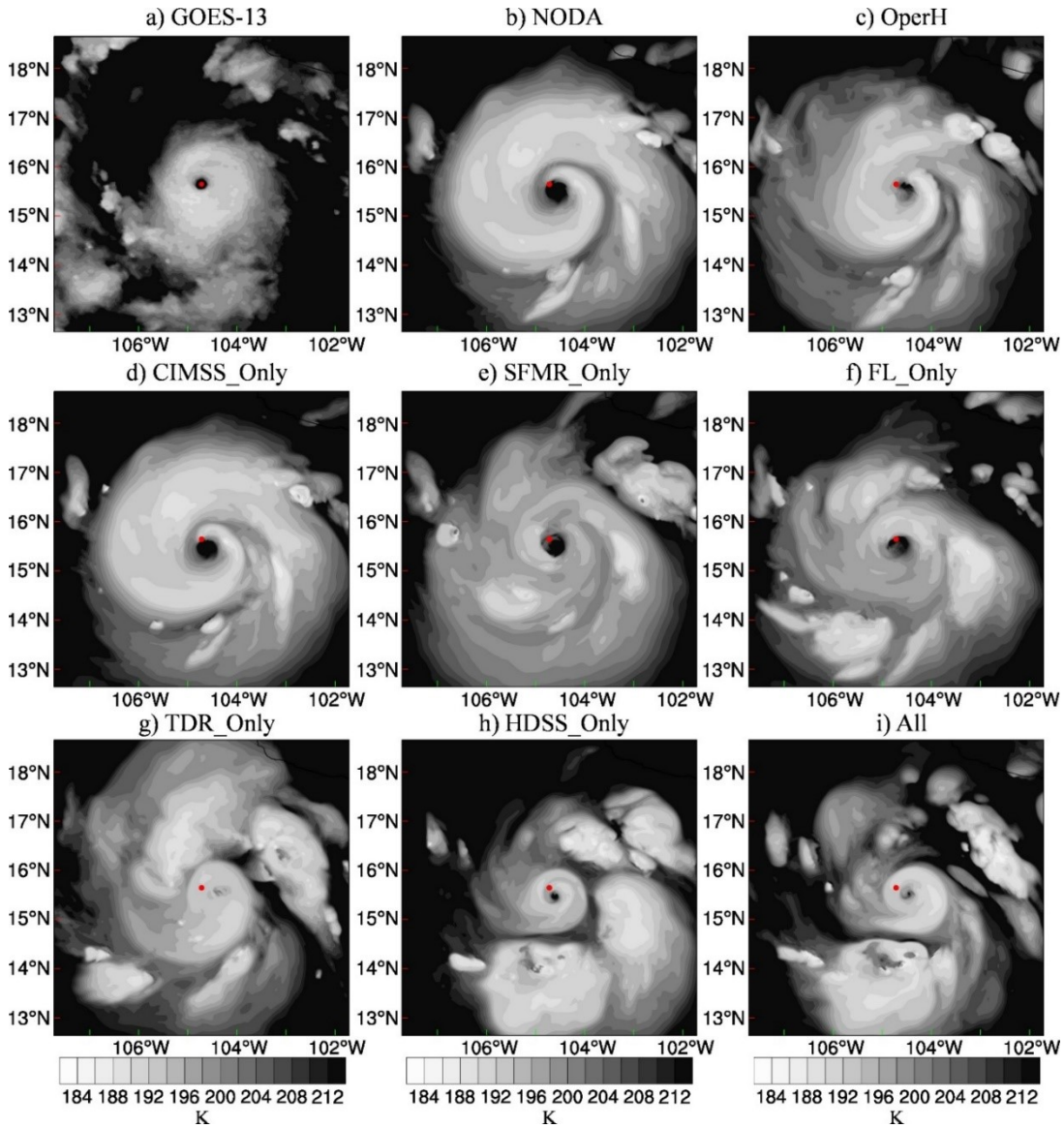

Figure 5.7 Same as Fig. 5.2 except for the 4-hour forecasted brightness temperature (K) in verification with (a) GOES-13 band 4 valid at 2200 UTC 22 Oct 2015 during Patricia. The red dots denote the satellite-derived

storm position at this time.

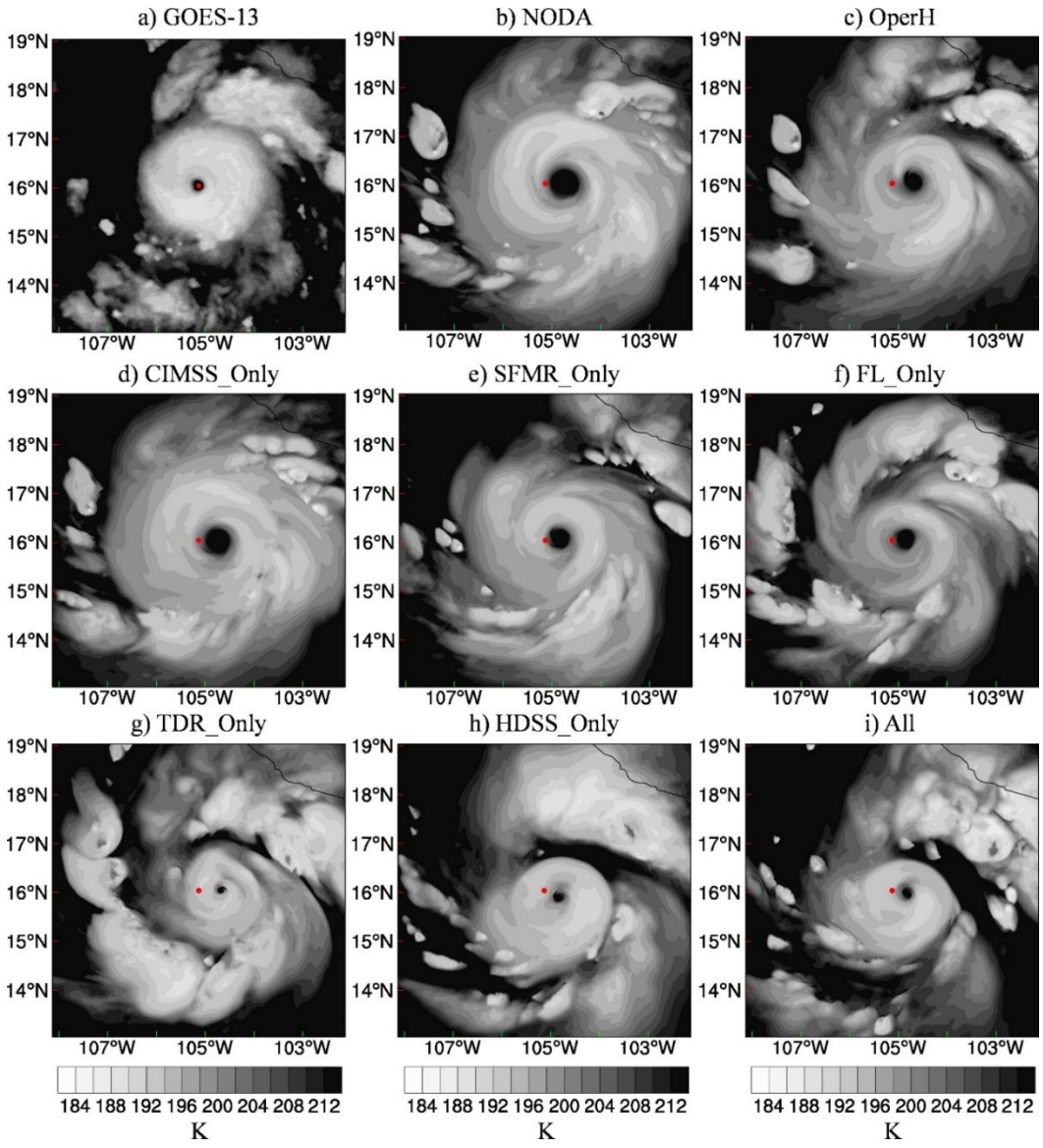

Figure 5.8 Same as Fig. 5.6 except for the 8-hour forecasted brightness temperature (K) valid at 0200 UTC 23 Oct 2015 during Patricia.

At 1800 UTC 23 October 2015, Patricia already entered a rapid weakening (RW) stage. But the storm was still well-organized, and the Vmax was as strong as 92.6 ms^{-1} (180 kt). The strong Vmax and the small size (RMW about 9-km) of Patricia can be consistently found in the Hurricane Imaging Radiometer (HIRAD) observations at 10-m altitude (Cecil et l. 2016) and the corresponding HRD radar composite at 3-km height (Figure 5.9 and Figure 5.10).

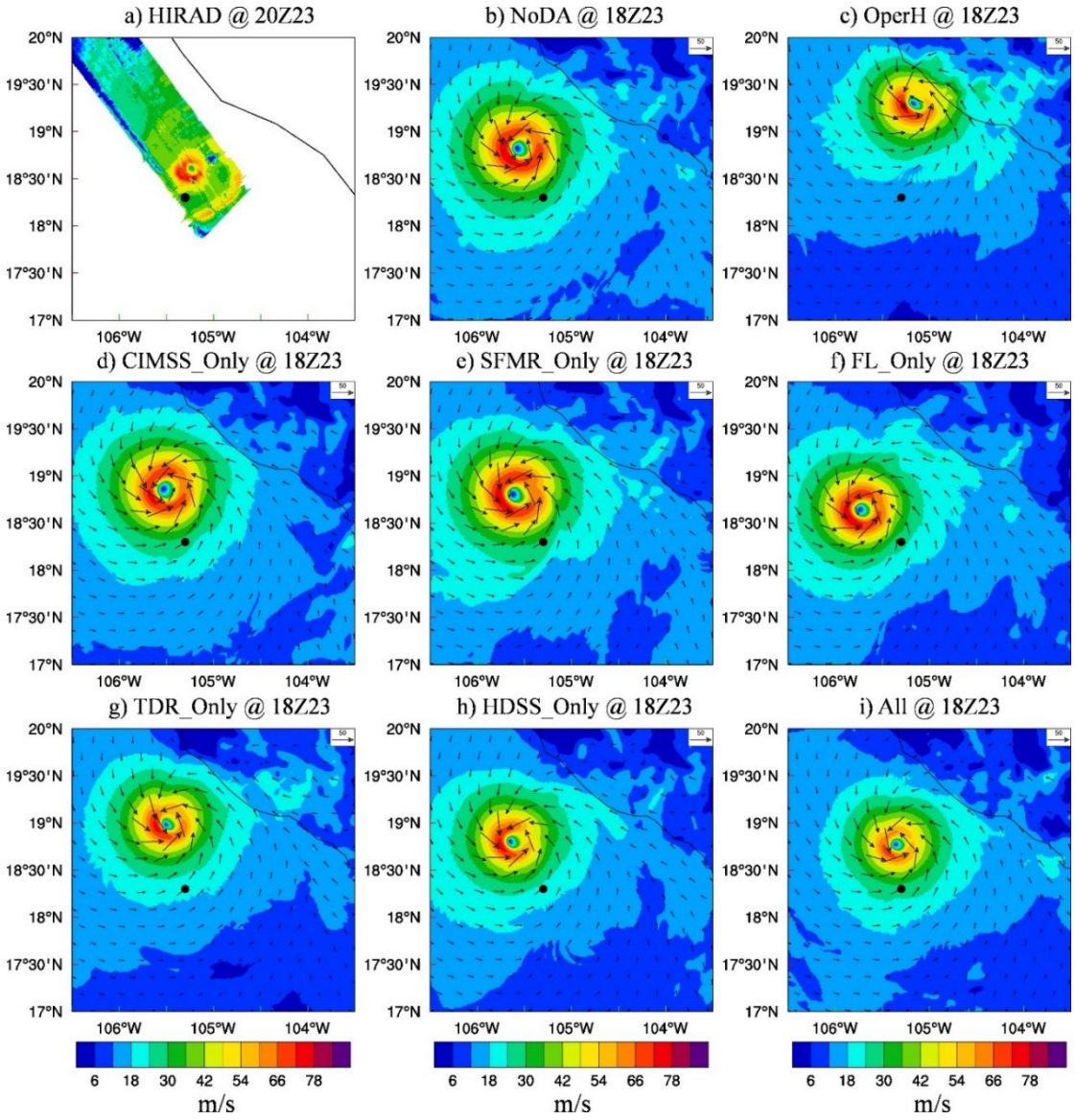

Figure 5.9 Same as Fig. 5.2 except for the 24-hour forecasted surface wind (shading and vectors, m s^{-1}) valid at 1800 UTC 23 Oct 2015 in verification with (a) HIRAD (Hurricane Imaging Radiometer) observations centered at 2000 UTC 23 Oct 2015 during Patricia. The domain size is the same in (a)-(i). The black dots denote the best track position at 1800 UTC 23 Oct 2015.

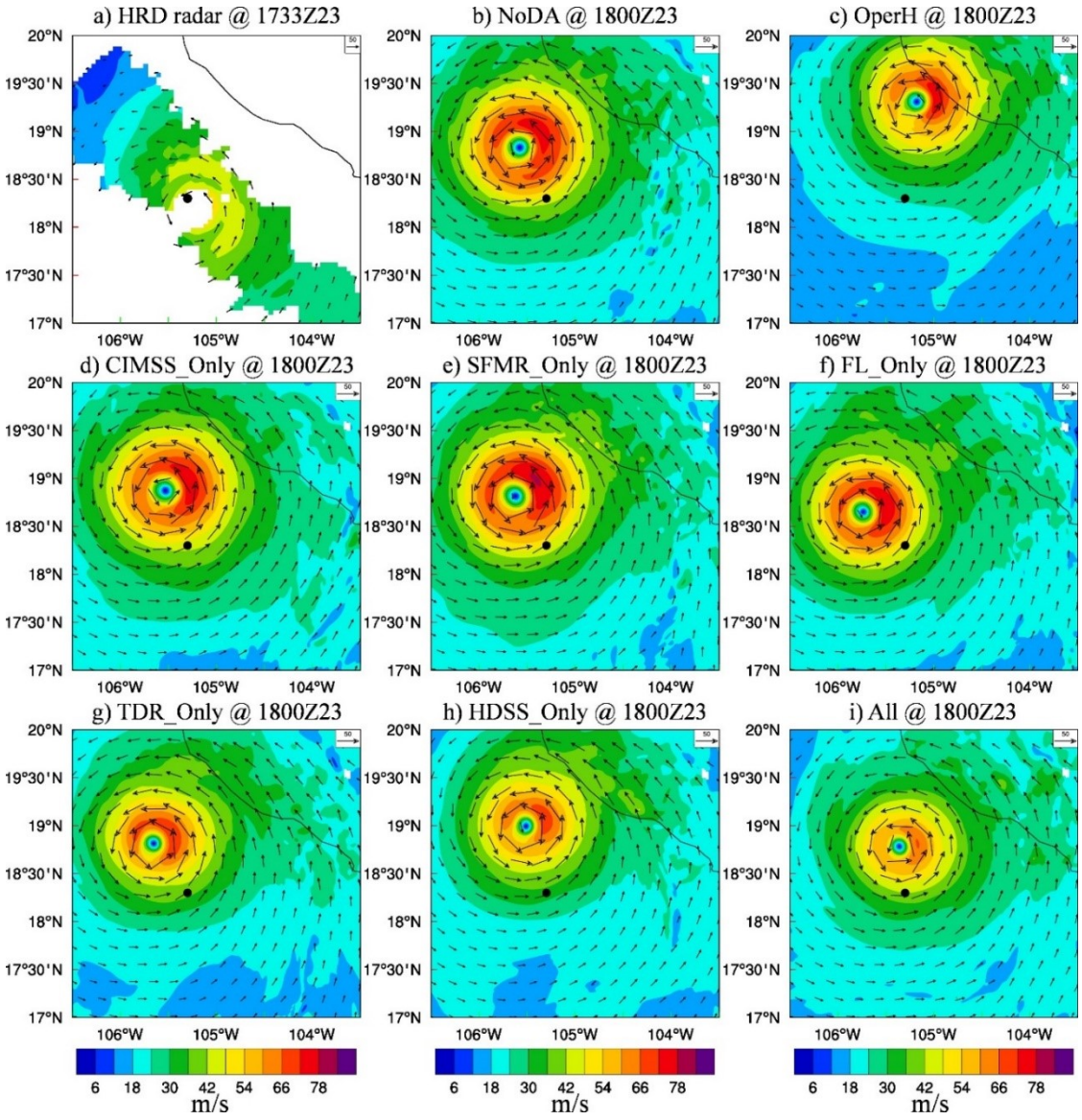

Figure 5.10 Same as Fig. 5.2 except for the 24-hour forecasted 3-km wind (shading and vectors, m s^{-1}) in verification with (a) HRD radar composite valid at 1733 UTC 23 Oct 2015 during Patricia. The black dots denote the best track position valid at 1800 UTC 23 Oct 2015.

5.3.2 Analysis and forecast from NoDA

This subsection shows model-predicted Patricia in the NoDA experiments during the 24 hours between 1800 UTC 22 October and 1800 UTC 23 October 2015.

At the initial time (1800 UTC 22 October), the vortex from NoDA is spuriously large in size, weak in intensity. For example, Fig. 5.2b shows that NoDA produces an RMW about 39-

km with the Vmax weaker than 45 ms^{-1}. Although the value of the wind speed maximum at 3-km is almost comparable with the observations (Fig. 5.3b), the storm is still significantly larger and more symmetric. This weak Vmax but comparable 3-km wind maximum structure in NoDA could be attributed to the HWRF model bias in the vertical wind profile (Tong et al. 2018). Additionally, NoDA produces incorrect radial inflow/outflow patterns. For example, the NW low-level outflow is incorrectly represented as an inflow (Fig. 5.4b), and the westward upper-level outflow in the W to NW side of the storm are overestimated (Fig. 5.5a, b).

Aside from those inconsistencies in the model-predicted dynamical fields, NoDA also suffers from biases in the thermodynamic fields of the TC. Specifically, Fig. 5.6b shows that the center of the UWC in NoDA is about 50 hPa lower than that captured by the HDSS dropsondes. Additionally, the MWC centered around 600 hPa is stronger than that in the observations. Both warm-cores are about twice as wide as those in the observations. Such an erroneously large warm-core size is consistent with the abnormally large storm size shown in Fig. 5.2 and Fig. 5.3.

Those spurious dynamic and thermodynamic structures in the initial conditions therefore produces false structural forecast within the next 24 hours. For example, in the model-derived BT patterns produced by NoDA, the eye size (~60-km on average) and the size of the CDO region (~400 to 500-km) are almost tripled or doubled the corresponding sizes in the observations, respectively (Fig. 5.7b - Fig. 5.8b). Moreover, given the larger regions of CDO, the spiral rainbands found in the observations become less pronounced in NoDA. For instance, at 22 UTC 22 October, there is only a few convective bands outside of the CDO (Fig. 5.7b). Four hours later at 02 UTC 23 October, the convective bands started to grow around the CDO (Fig. 5.8b). But the strong convective bands, which developed from the NE quadrant in the observations (Fig. 5.8a), are still significantly weaker and smaller in the NoDA forecast. After

24 hours of model integration, the storm size in NoDA is still significantly larger than the observations at all levels (Fig. 5.9b and Fig. 5.10b). Although the wind speed at the 3-km height in NoDA seems to be greater than the observations at hour 24, the Vmax is weaker. Again, this mismatch of the vertical wind profile could be attributed to the HWRF model bias (Tong et al., 2018).

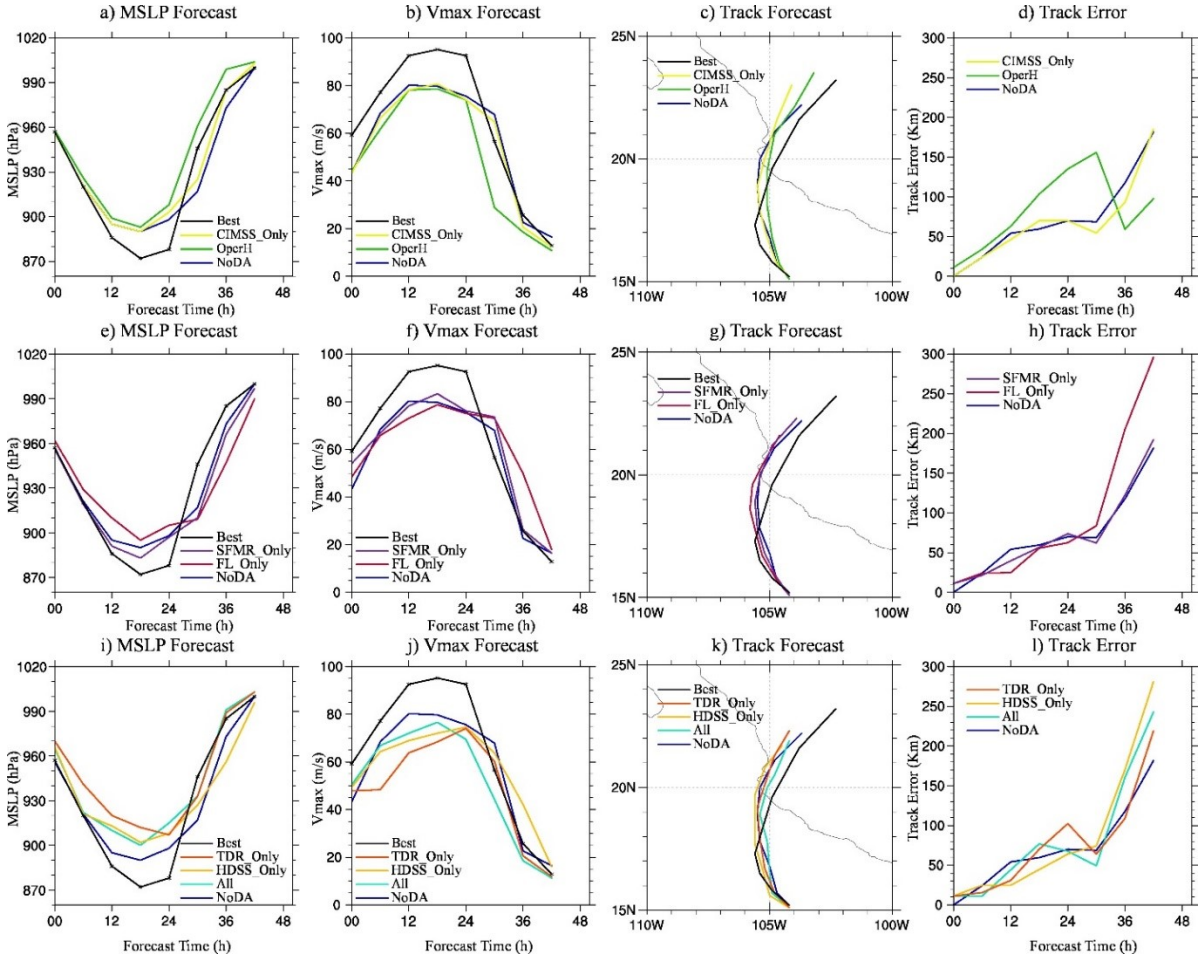

Figure 5.11 (a), (e), (i) MSLP forecast, (b), (f), (j) Vmax forecast, (c), (g), (k) track forecast and (d), (h), (l) track forecast errors for NoDA (blue), OperH (green), CIMSS_Only (yellow), SFMR_Only (purple), FL_Only (red), TDR_Only (orange), HDSS_Only (gold), All (cyan) and best track (black) initialized from 1800 UTC 22 Oct 2015 during Patricia.

In addition to evaluating the TC evolution in the forecasts, the traditional Minimum Sea Level Pressure (MSLP), Vmax and track forecasts produced by NoDA are also shown in Figure 5.11 and compared against the best track. Fig. 5.11 shows that although the initial MSLP in

NoDA is almost comparable with the best track, the initial Vmax is weaker. Fig. 5.11b also indicates that the RI rate in NoDA is roughly comparable to the best track, which is likely a result of the modified model physics as discussed in Chapter 4. The peak intensity is however weaker than the best track, and the time of peak Vmax is about 6 hours earlier. Overall, without any DA, NoDA produces a large and weak storm in both the analysis and the subsequent forecast.

5.3.3 Impact of the operational HWRF observations

Assimilating observations from the operational HWRF data stream, experiment OperH shows slight corrections in the vortex structure upon NoDA. For example, the west side of the vortex is weakened in OperH at both the surface and 3-km height as compared to NoDA (Fig. 5.2c and Fig. 5.3c). As indicated in Section 5.2.3, these low-level inner-core modifications in OperH primarily come from the assimilation of limited dropsondes and TCVital information. But Fig. 5.4c shows that OperH does not significantly modify the spurious low-level inflow in the NW section from NoDA. In the upper-levels, OperH reduces the strong outflow bias in the NW region of the storm as compared to NoDA (Fig. 5.4c and Fig. 5.5c). Such corrections are primarily due to the operational AMVs assimilated in OperH. To help better visualize the improvements, co-located radial wind increments from the DA analyses relative to NoDA are shown in Figure 5.12. Fig. 5.12a clearly shows the outflow reduction in the W to NW side of the storm upon NoDA. However, OperH also spuriously enhances the near-core inflow in the NW side of Patricia (around 16° N, 104.5° W). Additionally, an erroneous correction happens in the due south of TC, which resulted in the weakening of the southward outflow (e.g. between 12~13° N and 104~105.5° W). In the thermodynamic field, OperH slightly reduces the MWC in both size and strength upon NoDA (Fig. 5.6c), which is more consistent with the observations.

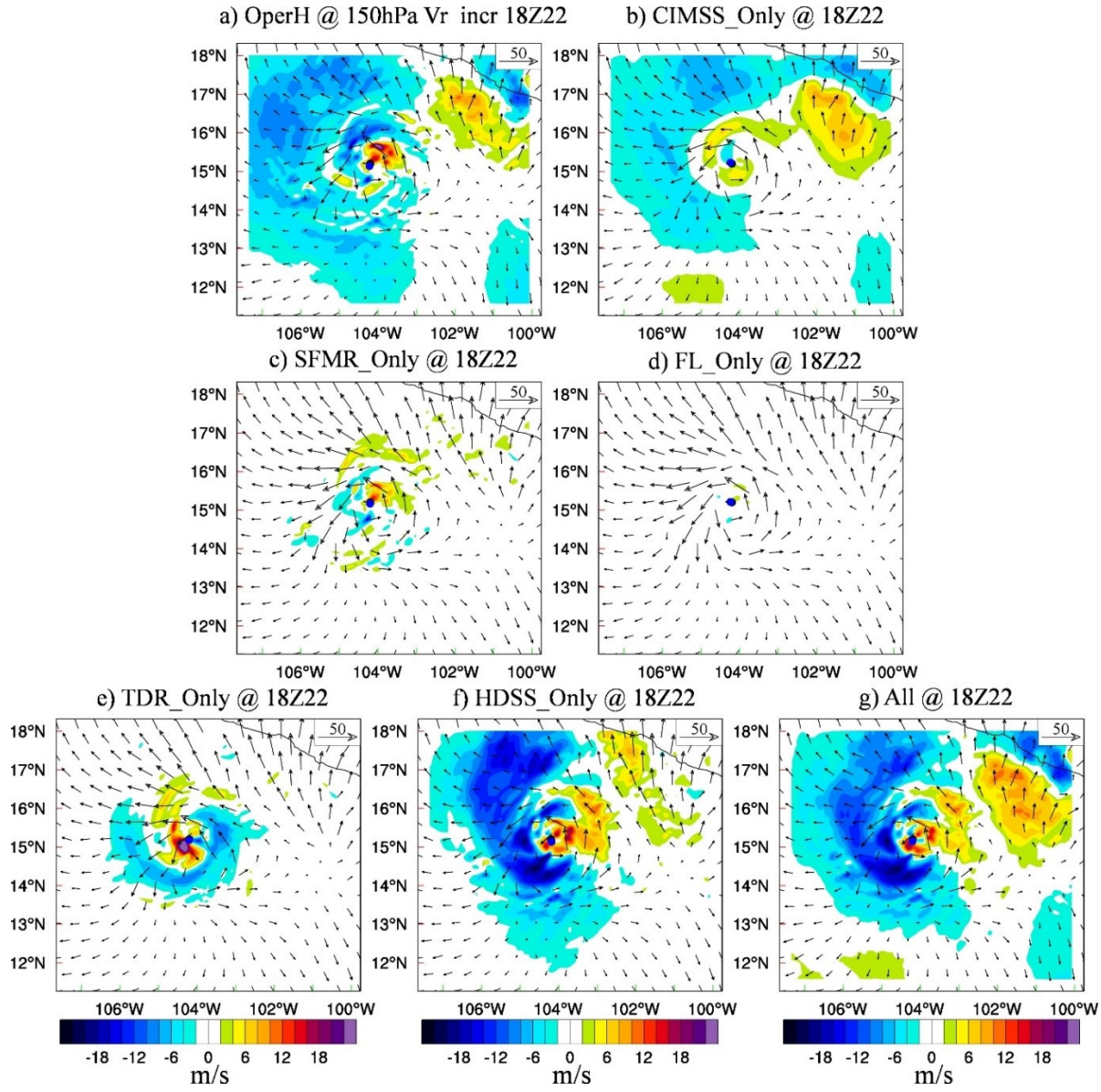

Figure 5.12 The co-located 150 hPa radial wind increment (shading, m s^{-1}) by subtracting NoDA from (a) OperH analysis, (b) CIMSS_Only analysis, (c) SFMR_Only analysis, (d) FL_Only analysis, (e) TDR_Only analysis, (f) HDSS_Only analysis and (g) All analysis valid at 1800 UTC 22 Oct 2015 during Patricia. The vectors are the 150 hPa horizontal wind from NoDA as a reference.

To further quantitively evaluate the analysis, the root-mean-square-fit (RMSF) of the analysis against the SFMR, FL, TDR, HDSS dropsondes and CIMSS AMV observations is calculated (Figure 5.13). The corresponding RMSF from the NoDA analysis is also given as a reference. For example, the RMSF to the SFMR, TDR and FL observations can measure the impact of assimilating the operational observations over NoDA in the inner-core region. The

corresponding RMSFs in Fig. 5.13 show that OperH improves the inner-core dynamic structures upon NoDA. Similarly, the RMSF calculated against the HDSS dropsonde observations can measure the 3D improvements of the DA analysis over NoDA in the inner-core and outflow regions, and the RMSF calculated against the CIMSS AMV observations can indicate that the corresponding improvements in the upper-level environment wind field. Fig. 5.13 shows that OperH overall slightly improves both the dynamic and thermodynamic fields relative to NoDA in almost all aspects.

Experiment / Verification Data Type	OperH	CIMSS_Only	SFMR_Only	FL_Only	TDR_Only	HDSS_Only	All	NoDA
OperH-q (g/kg)		2.50	3.49	2.20	2.48	2.42	2.00	2.50
OperH-t (K)		5.10	4.87	4.95	4.82	4.89	2.53	5.13
OperH-uv (m/s)		4.01	5.84	5.81	5.69	4.54	3.45	5.84
CIMSS-uv (m/s)	4.14		5.01	5.02	4.91	4.28	3.99	5.01
SFMR-spd (m/s)	6.10	6.73		6.06	6.21	6.04	4.65	6.73
FL-q (g/kg)	1.19	1.17	1.49		1.30	1.40	1.16	1.17
FL-t (K)	1.16	1.02	1.14		1.22	0.97	0.93	1.02
FL-uv (m/s)	4.49	4.98	5.43		3.42	3.75	3.12	4.98
TDR-rw (m/s)	6.17	7.03	6.19	4.87		4.42	3.58	7.09
HDSS-q (g/kg)	1.75	1.91	1.96	1.48	1.56		1.37	1.91
HDSS-t (K)	2.18	2.31	2.29	1.98	1.93		1.07	2.32
HDSS-uv (m/s)	9.62	10.77	9.74	8.21	7.98		7.37	10.89

<-20%	-20~-10%	-10~-1%	-1~+1%	+1~+10%	+10~+20%	>+20%

Figure 5.13 Root-Mean-Square-Fit (RMSF) of different types of observation verifications for each experiment. The colors denote the percentage of RMSF changes relative to NoDA for the independent verifications. The warmer the colors, the larger the relative RMSF.

Due to these improvements in the OperH analysis upon NoDA, the structural forecasts produced by OperH are also moderately better than NoDA. For example, both Fig. 5.7c and Fig. 5.8c show that the forecasted CDO region in OperH is always smaller than NoDA. However, these slightly reduced CDO regions are still much larger than the observations. Additionally, the eye in OperH is not well organized after 5 hours of model integration (e.g. Fig. 5.7c) and the simulated eye size is about twice the observed size (e.g. Fig. 5.8c). Moreover, OperH over-

predicts the storm speed, which pushes the predicted storm much closer to the Mexican coast than NoDA (e.g. Fig. 5.9c, Fig. 5.10c and Fig. 5.11c). The over-predicted storm movement is likely to be associated with the weaker but still large size of the storm, which is pushed by the northward steering environmental flow more than NoDA. The over-prediction of the storm speed therefore results in an early RW in the BT evolution after 1400 UTC October 23 (not shown). Such an early RW is also reflected by the Vmax and MSLP predictions (Fig. 5.11a, b). As a result of the early RW and the influence by land, the storm size produced by OperH becomes smaller than NoDA after 24 hours at 1800 UTC 23 October (Fig. 5.9c and Fig. 5.10c). Although such a contracted storm size in OperH seems to be more consistent with the observations, the 3D correlation coefficient calculated against the co-located HRD radar composite indicates that the wind patterns produced by OperH is actually worse than NoDA due to the early RW (Table 5.2)[11].

Table 5.2 Correlation coefficients calculated against the 3D HRD radar composite for the 24-hour forecasted storm structure from each experiment.

Experiment	NoDA	OperH	CIMSS_ Only	SFMR_ Only	FL_Only	TDR_On ly	HDSS_O nly	All
Correlation Coefficient	0.792248	0.790339	0.807257	0.788751	0.817344	0.805085	0.825169	0.834651

Overall, with rather limited inner-core observations, OperH is only able to slightly improve the structural analysis and prediction of Patricia at early lead times. Such benefits cannot be well maintained during the model integration, and storm movement becomes biased and degrades the predictions at later lead times.

[11] Table 5.2 is not to draw a statistically significant conclusion but to aid subjective interpretation of the difference between the predicted structure and the observations.

5.3.4 Impacts of CIMSS AMV observations

Since the number of CIMSS AMVs peaks around 150hPa in the innermost domain (Fig. 5.1c), the surface and low-level wind patterns in CIMSS_Only are almost identical to NoDA through subjective evaluation (Fig. 5.2b, d and Fig. 5.3b, d). This similarity is also reflected by the RMSF calculated against the SFMR and FL observations (Fig. 5.13). Because the thermodynamic observations in OperH are only available at the lower troposphere below 700 hPa from several WP-3D dropsondes, the RMSF against OperH thermodynamic observations indicates that there is almost no improvement in CIMSS_Only in those low levels. Likely due to that the CIMSS AMVs primarily sampled the environment wind outside 150-km radius (Fig. 5.1b), CIMSS_Only also does not show significant corrections in the near-core inflow and outflow wind patterns in the SE-NW cross-section as compared to NoDA (Fig.5. 4d). The inner-core thermodynamic structures like the warm-core in CIMSS_Only are also almost identical with NoDA (Fig. 5.6d). But the RMSFs against the 3D TDR radial velocity observations and the HDSS wind observations show that CIMSS_Only still improves the middle- to upper-level inner-core dynamic structure to some extent. Additionally, the RMSF against the OperH wind observations (primarily the operational AMVs, not shown) suggests that the CIMSS_Only produces more realistic upper-level environmental wind field than NoDA (Fig. 5.13). The major adjustment by CIMSS_Only is in the NW quadrant where the overly strong outflow is corrected (e.g. Fig. 5.12b).

The forecasted BT structures in CIMSS_Only are not significantly improved upon NoDA during the next 24 hours. CIMSS_Only is almost comparable with NoDA with only slight size contraction in the BT evolution (e.g. Fig. 5.7d and Fig. 5.8d). At 1800 UTC 23 October, the storm size predicted by CIMSS_Only is only slightly smaller than that produced by NoDA (e.g.

Fig. 5.9d and Fig. 5.10d). The 3D correlation coefficient against the co-located HRD radar composite also suggests only a slight improvement in the 3D inner-core structure in CIMSS_Only over NoDA (Table 5.2). This lack of improvements in the predicted structures in CIMSS_Only suggests that purely modifying the upper-level environment wind has limited impact on the prediction of short-term TC inner-core structure evolution. As a result, the Vmax, MSLP and track forecasts of CIMSS_Only are almost comparable with NoDA except that the peak Vmax time and the RI rate are now slightly more consistent with the best track (Fig. 5.11a~d).

5.3.5 Impact of SFMR observations

Assimilating the surface wind observations in the inner-core region, SFMR_Only shows more significant modifications in the surface vortex structure upon NoDA as compared to OperH and CIMSS_Only (Fig. 5.2e). For example, the surface RMW is now reduced to about 31-km, and the Vmax is significantly increased as compared to NoDA. However, the wind speed at 3-km height is also spuriously strengthened (Fig. 5.3e). This spurious correction is reflected by the increased RMSF against FL observations (Fig. 5.13), and it can be attributed to the biased vertical wind profile in the HWRF model (Tong et al. 2018). But the RMSFs against the TDR and HDSS wind observations show that the overall 3D inner-core structure produced by SFMR is still improved upon NoDA (e.g. contracted TC size). The improvement is reflected by the radial wind pattern in the middle- to low-levels (Fig. 5.4e). E.g., SFMR_Only reduces the inaccurate middle-level inflow (between 250 to 800 hPa) in the SE of NoDA. Also, the inflow between 600 hPa to 800 hPa in the NW of NoDA is enhanced in SFMR_Only, although this feature is only partially found and is much weaker in the observations. In the upper-level,

SFMR_Only shows little corrections upon NoDA in the radial wind pattern (Fig. 5.5e, Fig. 5.12c and Fig. 5.13).

In contrast to the aforementioned modifications in the kinematic fields, the RMSFs against the FL, HDSS and OperH thermodynamic observations suggest that the overall thermodynamic structures analyzed in SFMR_Only are degraded, especially in the moisture field (Fig. 5.13). But the size of the MWC is slightly reduced (Fig. 5.6e), somewhat more consistent with the observed as reflected by the RMSF against the HDSS temperature observations.

The forecasted eye and CDO sizes in SFMR_Only are reduced in comparison with NoDA at the early lead times (Fig. 5.7e and Fig. 5.8e). Nevertheless, the convections within and around the CDO are weaker than both NoDA and the observations. Moreover, the size improvement in the BT evolution is gradually lost as the model integrates (not shown). Consistently, the 24-hour vortex predicted by SFMR_Only is almost comparable with NoDA in both size and wind pattern, except the stronger wind maxima at both surface and 3-km height (Fig. 5.9e and Fig. 5.10e). Although the Vmax is closer to the best track (Fig. 5.11f), the 3-km height wind maximum is stronger than the observations. This can still be attributed to the HWRF model bias and it leads to a slightly degraded 3D structural forecast (Table 5.2).

Altogether, these results suggest that the assimilation of purely 2D surface wind observations in SFMR_Only is primarily helpful for the short-term inner-core structural prediction for Patricia. When verified against the best track, SFMR_Only produces the best Vmax forecasts among all the experiments (Fig. 5.11f). This result is as expected since the assimilation of SFMR observations should primarily modify the surface wind. With the strongest initial Vmax, SFMR_Only produces the highest peak intensity forecast among all the

experiments although its RI rate is slightly reduced as compared to NoDA. Finally, the track forecast seems to be almost comparable with the NoDA experiment (Fig. 5.11g, h).

5.3.6 Impact of FL observations

Like SFMR_Only, assimilating the 2D inner-core observations in FL_Only also produces significant modifications in the wind patterns from the surface to the middle-levels. For example, the surface RMW is now contracted to about 33-km and the Vmax is increased about 5 ms^{-1}, in more agreement with the observations than NoDA (Fig. 5.2f and Fig. 5.11f). Additionally, FL_only reduces the 3-km height wind speed in the SW region of the storm (Fig. 5.3f). Fig. 5.4f shows that FL_Only also produces corrections to the middle-level outflow and inflow in the SE and NW sections, respectively. These improvements in the inner-core dynamics are also reflected by the RMSF against the SFMR, TDR and HDSS wind observations (Fig. 5.13). However, like SFMR_Only, FL_Only barely changes the upper-level wind patterns when verified against the AMVs (Fig. 5.5f, Fig. 5.12d, and Fig. 5.13). Likely due to the assimilation of additional thermodynamic observations, the RMSFs against the OperH and HDSS temperature and moisture observations suggest that the inner-core thermodynamic structure produced by FL_Only is improved relative to NoDA. Such an improvement can be consistently found in Fig. 5.6f where FL_Only slightly reduces the MWC, and slightly elevates the UWC upon NoDA.

Overall, although both SFMR and FL data sample the TC's inner-core in the horizontal direction, the additional thermodynamic information in the FL observations produces a better analysis of the TC structure in FL_Only compared to SFMR_Only. Consequently, while the improvements from SFMR_Only over NoDA gradually diminish over time, the improvements from FL_Only last for the next 24 hours of model integration. For example, FL_Only continuously produces small eye (about 45-km in average) and small CDO regions after hours of

spin-up (e.g. Fig. 5.7f and Fig. 5.8f). The contracted storm produces a better fit to the observations than any NoDA, OperH, CIMSS_Only or SFMR_Only experiments. At 1800 UTC 23 October, the 24-hour forecasted vortex in FL_Only is still smaller and fits the observations better than the aforementioned experiments (Fig. 5.9f, Fig. 5.10f, and Table 5.2). However, the size contraction is still not sufficient when compared to the observations. Moreover, since the corrections from FL_Only are primarily in the inner-core region, the convections away from the core region evolve freely as the CDO region contracts. For instance, there are stronger and larger convective bands between the TC and the coast of Mexico generated around 0200 UTC 23 October (Fig. 5.8f), which lasts several hours longer than the observations (not shown).

Verification against the best track indicates that the intensity forecast in FL_Only is only improved relative to NoDA within the first 6 hours of model integration, in addition to the better timing of the Vmax peak (Fig. 5.11f). The track forecast at early lead times in FL_Only is slightly improved upon NoDA. However, such an improvement is lost at later lead times due to the slower movement after landfall (Fig. 5.11g). Overall, the improvements in the TC structural forecast produced by FL_Only upon NoDA do not lead to apparent improvement in Vmax, MSLP or track forecast. Although sampled at different levels, the results between FL_Only and SFMR_Only suggest the benefits of additional thermal observations upon the pure wind observations in maintaining the structural improvements from the DA analysis during forecast.

5.3.7 Impacts of TDR observations

As compared to FL_Only and SFMR_Only, assimilating 3D wind observations in TDR_Only leads to more contraction in the storm inner-core structures (Fig. 5.2g and Fig. 5.3g). The RMW in TDR_Only (28-km) is even smaller than SFMR_Only (31-km). In addition to the vortex size corrections, TDR_Only also modifies radial wind flow in the SE-NW cross-section

upon NoDA (Fig. 5.4g). For example, the middle-level inflow in the SE cross-section is corrected to be an outflow, and the low-level inflow in the NW cross-section (outside the 30-km radius) is corrected to be an outflow. These middle-level to surface improvements are reflected by the RMSFs against the SFMR and FL wind observations (Fig. 5.13). But in the upper-level, compared to NoDA, the NW outflow in TDR_Only is even more unrealistically strong (Fig. 5.4g, Fig. 5.12e). Even with these degradations in the upper-level outflow, the RMSF against the HDSS wind observations still indicates better analysis of the 3D inner-core dynamic structures than any other aforementioned DA experiment.

Other than improvements in the TC dynamics, positive data impacts are also apparent in the thermodynamic fields. For example, the two warm-cores in TDR_Only are reduced in both size and strength, and the center of the UWC is elevated to be between 200~250 hPa, in better agreement with the observations than NoDA. The only exception concerns the smaller depth of the UWC (Fig. 5.6g). Subsequently, the RMSF against the corresponding HDSS thermodynamic observations is smaller in Fig. 5.13. However, although the RMSFs against the OperH and HDSS thermodynamic observations indicate improvements, the RMSFs against the FL moisture and temperature observations still suggest some degradations in the TC thermodynamic structure as compared to NoDA. Note that the thermodynamic modifications in TDR_Only are purely from the cross-variable covariances due to the absence of thermodynamic observations. Such cross-variable corrections may not be accurate in the regions with highly nonlinear processes like the eyewall and rainbands.

Consequently, the early-lead time BT forecasts produced by TDR_Only are worse than NoDA. For example, there is no clear eye formed, and the convective bands are less organized as compared to either the observations or NoDA during the 4-hour BT forecast evolution (Fig.

5.7g). Such a BT evolution reflects the imbalances between the dynamic and the thermodynamic fields in the early lead times. However, once the balance is re-established 6 or 7 hours later, TDR_Only produces a storm structure more consistent with the observations than NoDA. For example, the eye size of TDR_Only is almost comparable with the observations at hour 8 although the CDO size is slightly smaller (Fig. 5.8g). The modification in the storm size in TDR_Only can be consistently found in the next 24 hours (Fig. 5.9g and Fig. 5.10g). But outside the CDO, when TDR_Only "cuts off" the connection between the CDO and those convective bands due to size contraction, the convections inherited from the spuriously large background in the data void regions become freely-developed. For instance, the spiral rainbands in the SW section are incorrectly larger (Fig. 5.8g) and the NE convective bands exist much longer (not shown) than the observations.

Verification against the best track data suggests that the intensity forecast in TDR_Only is not improved compared to NoDA. For example, the intensification in Vmax forecast is lagged and the peak intensity is lowered in TDR_Only in Fig. 5.11j. The track forecast at the early times is improved in TDR_Only as compared to NoDA but is slightly degraded after hour 15 (Fig. 5.11k, l). Overall, the improved structural analysis and forecast produced by TDR_Only upon NoDA do not lead to apparent improvements in the Vmax, MSLP or track forecast. In comparison to the 2D wind observations sampled by CIMSS AMV and SFMR, TDR has a 3D sampling of the TC inner-core structure with a broader spatial coverage. Therefore, the results between CIMSS_Only, SFMR_Only and TDR_Only suggest the benefits of 3D over 2D observations in maintaining the TC structural analysis improvements during the forecasts.

5.3.8 Impact of HDSS dropsonde observations

Similar to TDR_Only, assimilating the 3D HDSS dropsonde observations produces a significantly contracted storm that is more consistent with the observations than NoDA (Fig. 5.2h and Fig. 5.3h). For example, the initial Vmax is stronger (Fig. 5.11j), and the storm size in HDSS_Only is even smaller than TDR_Only (RMW 24-km v.s. 28-km). Additionally, HDSS_Only better captures the wind speed reduction in the SW quadrant of the storm than both NoDA and TDR_Only at 3-km height, although the wind maximum is stronger (Fig. 5.3h). As expected, the inner-core dynamic and thermodynamic structures produced by HDSS_Only fits the HDSS dropsondes the best among all the single-type observation DA experiments (Fig. 5.4h and Fig. 5.6h). For example, the size and the height of both warm-cores are simulated better than all the aforementioned DA experiments. Moreover, the unique sampling of the near-storm outflow in HDSS dropsondes ameliorates the upper-level outflow of the HDSS_Only analysis. For instance, the overly strong upper-level outflow in NoDA is now reduced to be comparable with CIMSS AMVs (Fig. 5.5h and Fig. 5.12f). Such corrections made by HDSS_Only are even better than CIMSS_Only and OperH in the NW regions. These corrections are reflected by the corresponding RMSFs against the CIMSS and OperH wind observations (Fig. 5.13). Also, the RMSFs against the SFMR, FL and TDR observations show that the HDSS_Only analysis produces the largest improvement in the inner-core structure amongst all single-type observation DA experiments, except the degradation in the RMSF against the FL moisture observations. The RMSF against OperH thermodynamic observations indicates that HDSS_Only improves the overall analyzed thermodynamic structure over NoDA.

As a result of simultaneous improvements in the TC thermodynamics and dynamics, HDSS_Only produces better BT forecasts than NoDA. For example, both the eye and CDO

region sizes are consistently smaller during the 24 hours of model integration (Fig. 5.7h and Fig. 5.8h). Unlike TDR_Only, the contracted CDO region and a clear eye can be quickly found in HDSS_Only within 4 hours of model integration (Fig. 5.7h). Furthermore, the spurious convective bands found in the NW of TDR_Only dissipated in HDSS_Only at hour 4 due to the distribution of HDSS observations at the analysis time. The remaining spurious convective bands primarily originated from the HDSS data sparse regions such as the SE quadrant of the storm. After 8 hours of model integration, the BT forecasts produced by HDSS_Only can capture the major features from observations (Fig. 5.8h). In addition to the comparably small eye and CDO sizes, a line of spotted convective bands in the SW quadrant and the relatively large NE convective bands can be consistently found in both HDSS_Only and GOES-13 observations. Although these convective bands are generally larger in size, stronger in strength and have longer lifetime as compared to the observations, the overall BT evolution in HDSS_Only outperforms all the other single-type observation DA experiments in the next 16 hours (not shown). At forecast hour 24, HDSS_Only continues to produce small storm size that is comparable with TDR_Only (Fig. 5.9h and Fig. 5.10h). The 3D inner-core structure forecasted by HDSS_Only fits the TDR observations even better than TDR_Only (Table 5.2). This result suggests that HDSS_Only produces not only the best structural analysis but also the best structural prediction up to 24 hours among all the single-type observation DA experiments. However, like TDR_Only and FL_Only, such an improvement in the structural predication does not lead to apparently improved Vmax, MSLP or track forecast. For example, although the RI of HDSS_Only is not delayed, the overall Vmax forecast improvement in HDSS_Only compared to NoDA is reflected primarily at the early lead-time and by the corrected timing of peak Vmax (Fig. 5.11i, j). Similar to the differences between CIMSS_Only, SFMR_Only and TDR_Only,

the difference between FL_Only and HDSS_Only also suggests the benefits of 3D over 2D observations in maintaining the TC structure improvements during the forecasts. Additionally, comparison between TDR_Only and HDSS_Only also suggests the benefits of additional thermal observations upon the wind observations in efficiently spinning up a storm from the DA analysis.

5.3.9 Impacts of all observations

Assimilating all observations together produces the most optimal dynamic structures among all experiments. For example, the surface wind pattern in All is comparable with HDSS_Only (Fig. 5.2i). They are both more consistent with the observations than other experiments. But All outperforms HDSS_Only in several aspects. For instance, the wind field like the maximum at 3-km height in All is more comparable with the observations than HDSS_only (Fig. 5.3i). Additionally, below 400 hPa and within 30-km radius, All produces slightly weaker inflow in the NW cross-section that fits the HDSS dropsondes even better than HDSS_Only (Fig. 5.4i). Such improvements are likely come from the assimilation of additional FL and TDR observations in All (Fig. 5.4f and Fig. 5.4g). The upper-level radial wind fields produced by All also fit the observations better than any other experiment (Fig. 5.5i). This better upper-level wind analysis in All can be attributed to the complementary sampling from the HDSS dropsondes and the CIMSS AMVs, where HDSS dropsondes sample more in the inner-core and outflow region, and CIMSS AMVs sample more over the near storm environment (Fig. 5.5i and Fig. 5.11g). The analyzed thermodynamic field in All seems to be dominated by the assimilation of the HDSS dropsonde observations, where both warm-cores are more consistent with the observations in size, height and strength than any other experiment except HDSS_Only (Fig. 5.6i). These results suggest that assimilating all observations produce the most realistic analysis among all

experiments. Such benefits are reflected in Fig. 5.13, where All shows the smallest RMSF to all observation types although this RMSF verification is no longer using independent observations.

Consistent with the superior analysis, the corresponding forecasts produced by All outperform all other experiments in several aspects as well. For example, like HDSS_Only, both the eye size and storm size in All are more comparable with the observations than other experiments (Fig. 5.7i and Fig. 5.8i). With the near storm environmental information from the CIMSS AMVs, All also produces further improved BT fields as compared to HDSS_Only in addition to the size contraction. Such an improvement is reflected in the less spurious convection in the E and NE portions of storm in the early hours (e.g. Fig. 5.7i), although the well-organized eye is formed about one hour later in All than HDSS_Only. Consistently, after hour 8, the spiral rainbands in the NE and SW side of the storm in All are weaker and more realistic than HDSS_Only (Fig. 5.8i). Overall, All produces the best BT evolution during the first 24 hours among all experiments. At 1800 UTC 23 October, the 3-km wind maxima in All is now reduced to be in agreement with the HRD radar composite (Fig. 5.10i) and the storm size is the smallest among all the experiments (Fig. 5.9i and Fig. 5.10i). Consistently, the All forecast produces the highest 3D correlation coefficients (Table 5.2). In general, assimilating all the observations leads to analysis and forecast of the TC structure that are superior to the individual data addition experiments.

Verification against the best track data suggests the improvement on intensity forecast are more limited than the structural forecast improvement. For example, the Vmax forecasts are improved for the first several hours and the timing of the peak Vmax is also corrected (Fig 5.11). These results suggest that commonly used intensity verification metrics like surface Vmax and MSLP may not be sufficient for a TC forecast evaluation. The size, the 3D structure and the

near-surface wind speed are important variables that need to be considered for future TC forecast evaluation.

5.4 Summary and Discussion

Using the upgraded GSI-based, continuously cycled, dual-resolution hybrid EnKF-Var DA system for HWRF, this chapter investigates the data impacts of various types of observations including those collected from the recent field campaigns from NOAA IFEX and ONR TCI programs and CIMSS AMVs on the analysis and prediction for hurricane Patricia (2015). Since this is a single-case study with one DA cycle, generalization of the impact results requires some cautions. This study does not aim to draw any statistically robust conclusion for the data impacts. Instead, the primary goal is to improve the physical understanding of the relative importance of these various types of observations on the analysis and prediction of different aspects of the storm.

While the background produced through the continuously cycled hybrid DA system produces a weak and large hurricane in NoDA, assimilating different types of observations impacts different aspects of the TC analysis and prediction: (1) OperH primarily improves the upper-level environment wind upon NoDA in the analysis, but produces early RW and early landfall; (2) CIMSS_Only shows further improved upper-level environmental analysis upon OperH, however, these improvements are short-lived; (3) SFMR_Only significantly modifies the surface wind structure in the analysis. Although these surface structure improvements cannot be maintained during the forecast, SFMR_Only produces the best Vmax forecast among all experiments; (4) FL_Only considerably modifies the inner-core structures in the lower troposphere, and these inner-core structure modifications can be consistently found in the model forecasts up to hour 24; (5) TDR_Only has more significant corrections in the 3D TC inner-core

dynamic structures than SFMR_Only and FL_Only. But given the lack of adequate thermodynamic corrections, TDR_Only degrades the early lead-time thermodynamic structure prediction and delays the RI; (6) HDSS_Only produces comparable 3D dynamic structures as TDR_Only in the inner-core region. In addition, HDSS_only further modifies the inner-core thermodynamic structures as well as the upper-level outflow. Consequently, HDSS_Only produces the best structure analysis and forecast among all the single-type observation experiments; (7) All further outperforms HDSS_Only in both structure analysis and forecast due to the complementary effects from combining all observations in consideration; (8) Although lots of these aforementioned experiments show apparent improvements of the structure in both the analysis and forecast, such structural improvements are not necessarily directly translated into the Vmax and MSLP forecast improvements. In fact, most of the experiments do not show much of improvement on the peak intensity value although some experiments demonstrate intensity improvements for the first several hours and some demonstrate corrections in the timing of peak intensity.

Overall, this study hints that (1) Assimilating observations that only sample the 2D structures of the storm can improve the TC structure analysis, but the improvement is not as large as that produced by assimilating 3D observations (e.g. CIMSS_Only & SFMR_Only v.s. TDR_Only, FL_Only v.s. HDSS_Only); (2) Assimilating observations that purely samples the momentum field can correct the inner-core thermodynamic structure to some extent through the cross-variable covariance. However, compared to assimilating observations that sample both the momentum and thermodynamic fields, such corrections can be shorter-lived (e.g. SFMR_Only v.s. FL_Only) or be associated with slow spin-up (e.g. TDR_Only v.s. HDSS_Only); (3) The

inconsistency of the data impact on the intensity and structural forecast implies that future TC forecast evaluation would need to consider multiple verification metrics at once.

Additionally, Chapter 4 suggests that the model resolution can be a critical factor to influence the predicted peak intensity for small hurricanes like Patricia. Therefore, additional experiments are also conducted in this study and the results show that increasing model resolution significantly improves the intensity forecasts for all experiments (Not shown). But the relative data impacts remain nearly the same except for TDR_Only, HDSS_Only and All. Further extensive experiments regarding the impact of high-resolution configurations are still needed. In addition, a further study on how different combinations of each type of observations can help improve the TC analysis and prediction are planned in future papers.

Chapter 6: Summary and Future Plans

6.1 General Summary

A GSI-based, continuously cycled, dual-resolution hybrid EnVar DA system is developed for HWRF with multiple capabilities. The multi-capabilities allow the system to (i) produce a continuously cycled, self-consistent HWRF EnKF ensemble, (ii) apply the newly developed directed moving nest strategy, (iii) perform either 3DEnVar or 4DEnVar DA, (iv) integrate with the VM and VR strategies, and (v) assimilate various kinds of vortex-scale observations in addition to the operational observations. The details of this DA system are first described in Chapter 2 of this dissertation. Using the advanced DA system, a few scientific questions discussed in Chapter 1.2 are addressed in this dissertation.

To understand if using a more advance data assimilation system to assimilate vortex-scale observations can help improve the TC analysis and intensity prediction, experiments are first conducted with hurricane Edouard (2014) in Chapter 3. It was found that:

i) The dual-resolution DA experiment, in which a high-resolution control background at 3-km grid spacing is combined with a coarse-resolution ensemble at 9-km grid spacing, produces more realistic storm structures and better subsequent intensity predictions than the single low-resolution DA, in which both control and ensemble background are at 9-km grid spacing.

ii) Applying VR to the control background for all DA cycles and applying VM to the control background for only the DA cycles without TDR observations are important for a cycling DA system to improve the TC analysis and forecast. Additional VR on the ensemble background can further improve the TC structure analysis and subsequent short-term intensity forecast with reduced error bias.

iii) The 4DEnVar can produce a more realistic analysis and a better intensity forecast than the 6-hourly 3DEnVar when the error structures are fast-evolving.

iv) The cycling 4DEnVar DA system improves the intensity forecast upon the operational HWRF by producing a more realistic inner-core structure during the intensification period of hurricane Edouard (2014).

However, as shown in Chapter 4, the more realistic DA analysis from the advanced HWRF DA system is not always enough to improve the intensity prediction of TCs. Experiments with hurricane Patricia (2015) indicate that although the assimilation of inner-core observations produces a realistic 3D analysis of the storm, a serious spin-down issue (e.g. Vmax drop greater than 10 ms^{-1} within the first 6 hours) can occur with this realistic analysis but not with the unrealistic VM analysis.

Further investigations in Chapter 4 show that the spin-down is likely to be attributed to the incompatibility between the realistic DA analysis and the unrealistic model physics. A modified parameterization with reduced horizontal diffusion and a modified PBL scheme accounting for the in-cloud turbulent are found to be alleviating the spin-down issue. The reduced horizontal diffusion can better maintain the vertical oscillation of sub-/super-gradient flows from the DA analysis and the in-cloud turbulent can improve the vertical diffusion profile, which is crucial for the intensification rate of the HWRF model forecast. In general, these results suggest that the realistic DA analysis requires a compatible, realistic model physics to maintain the benefits of inner-core DA and improve the TC intensity forecast. Additional investigations in Chapter 4 show that the model resolution can be important in improving the RI rate and peak intensity of TC forecast.

Based on the optimal DA and system configuration from Chapter 3 and the modified model physics from Chapter 4, the last part of this dissertation focuses on the relative impact of various vortex-scale observations on TC prediction. Detailed investigations are performed on the structure analysis and forecast evolution for each data type assimilated during Patricia (2015) in Chapter 5. The comparisons suggest that:

i) During the assimilation of vortex-scale observations, the inner-core structure analysis of TCs would benefit more from the 3D observations than the 2D observations;

ii) During the forecast after assimilating vortex-scale observations, the structure and intensity forecast would benefit more from the assimilation of observations that sample both momentum and thermal fields than from the assimilation of observations that only sample momentum field;

iii) During the forecast after assimilating vortex-scale observations, the structure forecast tends to benefit more than the corresponding intensity forecast. Such an inconsistency suggests that better verification metrics (e.g. considering size and structure) are needed for future TC forecast evaluation.

Since this is only a preliminary work with a single case, the results and hints from this Chapter 5 are not to draw any statistical conclusions for the data impacts, but to lay the foundation for additional DA methodology and sensitivity impact studies in the future.

6.2 Future Plans

The development of the GSI-based, cycling hybrid DA system for HWRF provides a great platform to investigate all kinds of scientific questions to improve the TC forecast. While series of experiments have been carried out in this dissertation, follow-up studies are still needed. Our

future work will include but not limited to further investigations in (1) methods to treat the incompatibility between DA and model; (2) methods to treat the nonlinearity and non-Gaussianity issues during the DA; and (3) the effective assimilation of satellite radiance together with ground-based remote sensing observations.

References

Abarca, S. F., M. T. Montgomery, S. A. Braun, and J. Dunion, 2016: On the secondary eyewall formation of Hurricane Edouard (2014). *Mon. Wea. Rev.*, MWR-D-15-0421.1.

Aksoy, A., S. Lorsolo, T. Vukicevic, K. J. Sellwood, S. D. Aberson, and F. Zhang, 2012: The HWRF Hurricane Ensemble Data Assimilation System (HEDAS) for High-Resolution Data: The Impact of Airborne Doppler Radar Observations in an OSSE. *Mon. Wea. Rev.*, **140**, 1843–1862.

——, S. D. Aberson, T. Vukicevic, K. J. Sellwood, S. Lorsolo, and X. J. Zhang, 2013: Assimilation of High-Resolution Tropical Cyclone Observations with an Ensemble Kalman Filter Using NOAA/AOML/HRD's HEDAS: Evaluation of the 2008-11 Vortex-Scale Analyses. *Mon. Wea. Rev.*, **141**, 1842–1865.

Barker, D. M., W. Huang, Y.-R. Guo, A. J. Bourgeois, and Q. N. Xiao, 2004: A Three-Dimensional Variational Data Assimilation System for MM5: Implementation and Initial Results. *Mon. Wea. Rev.*, **132**, 897–914.

Bauer, P., P. Lopez, A. Benedetti, D. Salmond, and E. Moreau, 2006: Implementation of 1D+4D-Var assimilation of precipitation-affected microwave radiances at ECMWF. I: 1D-Var. *Q. J. R. Meteorol. Soc.*, **132**, 2277–2306.

——, A. J. Geer, P. Lopez, and D. Salmond, 2010: Direct 4D-Var assimilation of all-sky radiances. Part I: Implementation. *Q. J. R. Meteorol. Soc.*, **136**, 1868–1885.

——, and Coauthors, 2011: Satellite cloud and precipitation assimilation at operational NWP centres. *Q. J. R. Meteorol. Soc.*, **137**, 1934–1951.

Bell, M. M., and Coauthors, 2016: ONR Tropical Cyclone Intensity 2015 NASA WB-57 HDSS dropsonde data, version 1.0. UCAR/NCAR Earth Observing Laboratory, accessed 12 April 2016, doi:https://doi.org/10.5065/D6KW5D8M.

Bender, M. A., 1993: Improvements in Tropical Cyclone Track and Intensity Forecasts Using the GFDL Initialization System. *Mon. Wea. Rev.*, **121**, 2046–2061.

Bernardet, L., V. Tallapragada, C. Holt, S. Trahan, M. Biswas, L. Carson, H. Shao, and C. Zhou, 2015: Transition of Research to the Operational Hurricane WRF model: the Role of the Developmental Testbed Center. *6th NOAA Testbeds and Proving Grounds Workshop*, 2015 Apr 14-16, Boulder, CO.

Black, P., L. Harrison, M. Beaubien, R. Bluth, R. Woods, A. Penny, R. W. Smith, and J. D. Doyle, 2017: High-Definition Sounding System (HDSS) for Atmospheric Profiling. *J. Atmos. Ocean. Technol.*, **34**, 777–796.

Braun, S. A., M. T. Montgomery, and Z. Pu, 2006: High-Resolution Simulation of Hurricane Bonnie (1998). Part I: The Organization of Eyewall Vertical Motion. *J. Atmos. Sci.*, **63**, 19–42.

——, P. A. Newman, and G. M. Heymsfield, 2016: NASA'S HURRICANE AND SEVERE STORM SENTINEL (HS3) INVESTIGATION. *Bull. Amer. Meteor. Soc.*, 2085–2102.

Bryan, G. H., 2012: Effects of Surface Exchange Coefficients and Turbulence Length Scales on the Intensity and Structure of Numerically Simulated Hurricanes. *Mon. Wea. Rev.*, **140**, 1125–1143.

Bryan, G. H., and R. Rotunno, 2009a: Evaluation of an Analytical Model for the Maximum Intensity of Tropical Cyclones. *J. Atmos. Sci.*, **66**, 3042–3060.

——, and ——, 2009b: The Maximum Intensity of Tropical Cyclones in Axisymmetric Numerical Model Simulations. *Mon. Wea. Rev.*, **137**, 1770–1789.

Buehner, M., P. L. Houtekamer, C. Charette, H. L. Mitchell, and B. He, 2010: Intercomparison of Variational Data Assimilation and the Ensemble Kalman Filter for Global Deterministic NWP. Part II: One-Month Experiments with Real Observations. *Mon. Wea. Rev.*, **138**,

1567–1586.

Chen, H., and D.-L. Zhang, 2013: On the Rapid Intensification of Hurricane Wilma (2005). Part II: Convective bursts and the upper-level warm core. *J. Atmos. Sci.*, **70**, 146–162.

——, ——, J. Carton, and R. Atlas, 2011: On the Rapid Intensification of Hurricane Wilma (2005). Part I: Model Prediction and Structural Changes. *Wea. Forecast.*, **26**, 885–901.

Chen, Y., and C. Snyder, 2007: Assimilating Vortex Position with an Ensemble Kalman Filter. *Mon. Wea. Rev.*, **135**, 1828–1845.

Clayton, a. M., a. C. Lorenc, and D. M. Barker, 2013: Operational implementation of a hybrid ensemble/4D-Var global data assimilation system at the Met Office. *Q. J. R. Meteorol. Soc.*, **139**, 1445–1461.

Cram, T. a., J. Persing, M. T. Montgomery, and S. a. Braun, 2007: A Lagrangian Trajectory View on Transport and Mixing Processes between the Eye, Eyewall, and Environment Using a High-Resolution Simulation of Hurricane Bonnie (1998). *J. Atmos. Sci.*, **64**, 1835–1856.

Davis, C., and L. F. Bosart, 2002: Numerical Simulations of the Genesis of Hurricane Diana (1984). Part II: Sensitivity of Track and Intensity Prediction. *Mon. Wea. Rev.*, **130**, 1100–1124.

——, W. Wang, J. Dudhia, and R. Torn, 2010: Does Increased Horizontal Resolution Improve Hurricane Wind Forecasts? *Wea. Forecast.*, **25**, 1826–1841.

Dong, J., and M. Xue, 2013: Assimilation of radial velocity and reflectivity data from coastal WSR-88D radars using an ensemble Kalman filter for the analysis and forecast of landfalling hurricane Ike (2008). *Q. J. R. Meteorol. Soc.*, **139**, 467–487.

Doyle, J. D., and Coauthors, 2017: A View of Tropical Cyclones from Above: The Tropical

Cyclone Intensity (TCI) Experiment. *Bull. Am. Meteorol. Soc.*, **98**, 2113–2134.

Emanuel, K. A., 1986: An Air-Sea Interaction Theory for Tropical Cyclones. Part I: Steady-State Maintenance. *J. Atmos. Sci.*, **43**, 585–605.

——, 1995: Sensitivity of Tropical Cyclones to Surface Exchange Coefficients and a Revised Steady-State Model incorporating Eye Dynamics. *J. Atmos. Sci.*, **52**, 3969–3976.

——, 1997: Some Aspects of Hurricane Inner-Core Dynamics and Energetics. *J. Atmos. Sci.*, **54**, 1014–1026.

Fels, S. B., and M. D. Schwarzkopf, 1975: The simplified exchange approximation: A new method for radiative transfer calculations. *J. Atmos. Sci.*, **32**, 1475–1488.

Ferrier, B. S., 2005: An efficient mixed-phase cloud and precipitation scheme for use in Operational NWP Models. *American Geophysical Union, Spring Meeting 2005, abstract id. A42A-02*.

Fierro, A. O., and J. M. Reisner, 2011: High-Resolution Simulation of the Electrification and Lightning of Hurricane Rita during the Period of Rapid Intensification. *J. Atmos. Sci.*, **68**, 477–494.

Friedman, H. A., 1982: Airborne research meteorological data collected by the National Hurricane Research Laboratory during the NOAA/RFC WP-3D era : inventory and availability. https://repository.library.noaa.gov/view/noaa/9448

——, 1984: Airborne research meteorological data collected by the National Hurricane Research Laboratory (Hurricane Research Division/AOML) during the 1982-1983 hurricane seasons : inventory and availability. https://catalog.hathitrust.org/Record/102347235

Gamache, J., 2005: Real-time dissemination of hurricane wind fields determined from airborne Doppler radar data real-time dissemination of hurricane wind fields determined. JHT

Project Final Rep., 38 pp., http://www.nhc.noaa.gov/jht/2003-2005reports/DOPLRgamache_JHTfinalreport.pdf.

Gamache, J. F., J. Robert A. Houze, and J. Frank D. Marks, 1993: Dual-Aircraft Investigation of the Inner Core of Hurricane Norbert. Part III: Water Budget. *J. Atmos. Sci.*, **50**, 3221–3243.

Gao, J., and M. Xue, 2008: An Efficient Dual-Resolution Approach for Ensemble Data Assimilation and Tests with Simulated Doppler Radar Data. *Mon. Wea. Rev.*, **136**, 945–963.

Gaspari, G., and S. E. Cohn, 1999: Construction of correlation functions in two and three dimensions. *Q. J. R. Meteorol. Soc.*, **125**, 723–757.

Geer, A. J., and Coauthors, 2017: All-sky satellite data assimilation at operational weather forecasting centres. *Q. J. R. Meteorol. Soc.*,.

——, and Coauthors, 2018: All-sky satellite data assimilation at operational weather forecasting centres. *Q. J. R. Meteorol. Soc.*, **144**, 1191–1217.

Gopalakrishnan, S. G., F. Marks, J. a. Zhang, X. Zhang, J.-W. Bao, and V. Tallapragada, 2013: A Study of the Impacts of Vertical Diffusion on the Structure and Intensity of the Tropical Cyclones Using the High Resolution HWRF system. *J. Atmos. Sci.*, **70**, 524–541.

Guimond, S. R., G. M. Heymsfield, P. D. Reasor, and A. C. Didlake, 2016: The Rapid Intensification of Hurricane Karl (2010): New Remote Sensing Observations of Convective Bursts from the Global Hawk Platform. *J. Atmos. Sci.*, **73**, 3617–3639.

Hack, J. J., and W. H. Schubert, 1986: Nonlinear Response of Atmospheric Vortices to Heating by Organized Cumulus Convection. *J. Atmos. Sci.*, **43**, 1559–1573.

Hamill, T. M., J. S. Whitaker, D. T. Kleist, M. Fiorino, and S. G. Benjamin, 2011: Predictions of 2010's Tropical Cyclones Using the GFS and Ensemble-Based Data Assimilation Methods. *Mon. Wea. Rev.*, **139**, 3243–3247.

Han, J., and H. Pan, 2011: Revision of Convection and Vertical Diffusion Schemes in the NCEP Global Forecast System. *Wea. Forecast.*, **26**, 520–533.

Holland, G., and R. Merrill, 1984: On the dynamics of tropical cyclone structural changes. *Q. J. R. Meteorol. Soc.*, **110**, 723–745.

Hong, S.-Y., and H.-L. Pan, 1996: Nonlocal Boundary Layer Vertical Diffusion in a Medium-Range Forecast Model. *Mon. Wea. Rev.*, **124**, 2322–2339.

Houze, R. a, S. S. Chen, B. F. Smull, W.-C. Lee, and M. M. Bell, 2007: Hurricane intensity and eyewall replacement. *Science*, **315**, 1235–1239.

HRD, 2015: Hurricane Research Division dataset during Hurricane Patricia. NOAA, accessed 19 November 2017, http://www.aoml.noaa.gov/hrd/Storm_pages/patricia2015/.

Kenul, P., J. Coffey, J. Walker, A. Roberts, and J. Huning, 2018: NOAA Technical Memorandum OAR GSD-61. NOAA Technical Memorandum OAR UAS-003,.

Kimberlain, T. B., E. S. Blake, and J. P. Cangialosi, 2016: NATIONAL HURRICANE CENTER TROPICAL CYCLONE REPORT Hurricane Patricia.

Kleist, D., and K. Ide, 2015a: An OSSE-Based Evaluation of Hybrid Variational – Ensemble Data Assimilation for the NCEP GFS . Part I : System Description and 3D-Hybrid Results. 433–451.

——, and K. Ide, 2015b: An OSSE-Based Evaluation of Hybrid Variational–Ensemble Data Assimilation for the NCEP GFS. Part II: 4DEnVar and Hybrid Variants. *Mon. Wea. Rev.*, **143**, 452–470.

Kuhl, D. D., T. E. Rosmond, C. H. Bishop, J. Mclay, and N. L. Baker, 2013: Comparison of Hybrid Ensemble/4DVar and 4DVar within the NAVDAS-AR Data Assimilation Framework. *Mon. Wea. Rev.*, **141**, 2740–2758.

Kurihara, Y., and M. Bender, 1990: Prediction experiments of Hurricane Gloria (1985) using a multiply nested movable mesh model. *Mon. Weather …*,.

——, M. A. Bender, and R. J. Ross, 1993: An initialization scheme of hurricane models by vortex specification. *Mon. Wea. Rev.*, **121**, 2030–2045.

——, M. a. Bender, R. E. Tuleya, and R. J. Ross, 1995: Improvements in the GFDL Hurricane Prediction System. *Mon. Wea. Rev.*, **123**, 2791–2801.

——, R. E. Tuleya, and M. A. Bender, 1998: The GFDL Hurricane Prediction System and Its Performance in the 1995 Hurricane Season. *Mon. Wea. Rev.*, **126**, 1306–1322.

Lacis, A. A., and J. E. Hansen, 1974: A parameterization for the absorption of solar radiation in the earth's atmosphere. *J. Atmos. Sci.*, **31**, 118–133.

Li, Y., 2015: ASSIMILATION OF RADAR OBSERVATIONS WITH ENSEMBLE VARIATIONAL HYBRID DATA ASSIMILATION METHOD FOR THE INITIALIZATION AND PREDICTION OF HURRICANES, Oklahoma University, 1–124 pp.

——, X. Wang, and M. Xue, 2012: Assimilation of Radar Radial Velocity Data with the WRF Hybrid Ensemble-3DVAR System for the Prediction of Hurricane Ike (2008). *Mon. Wea. Rev.*, **140**, 3507–3524.

Liu, Q., T. Marchok, H. Pan, M. Bender, and S. Lord, 2000: Improvements in Hurricane Initialization and Forecasting at NCEP with Global and Regional (GFDL) models. *NCEP Office Note*, 472.

——, S. Lord, N. Surgi, Y. Zhu, R. Wobus, Z. Toth, and T. Marchok, 2006: Hurricane Relocation in Global Ensemble Forecast System. *27th Conference on Hurricanes and Tropical Meteorology*.

Liu, Y., D.-L. Zhang, and M. K. Yau, 1997: A Multiscale Numerical Study of Hurricane Andrew (1992). Part I: Explicit Simulation and Verification. *Mon. Wea. Rev.*, **125**, 3073–3093.

Lu, X., and X. Wang, 2019a: Improving Hurricane Analyses and Predictions with TCI, IFEX Field Campaign Observations and CIMSS AMVs Using the Advanced Hybrid Data Assimilation system for HWRF . Part I : What is missing to capture the rapid intensification of Hurricane Patricia (2015) when HWRF is already Initialized with a More Realistic Analysis?. *Mon. Wea. Rev.,* **147**, 1351–1373.

——, and ——, 2019b: Improving Hurricane Analyses and Predictions with TCI, IFEX Field Campaign Observations and CIMSS AMVs Using the Advanced Hybrid Data Assimilation system for HWRF . Part II : Observations Impact on Analyses and Predictions of Patricia (2015). *Mon. Wea. Rev.*, submitted in revision.

——, ——, Y. Li, M. Tong, and X. Ma, 2017a: GSI-based ensemble-variational hybrid data assimilation for HWRF for hurricane initialization and prediction: impact of various error covariances for airborne radar observation assimilation. *Q. J. R. Meteorol. Soc.*, **143**, 223–239.

——, ——, M. Tong, and V. Tallapragada, 2017b: GSI-based, Continuously Cycled, Dual-Resolution Hybrid Ensemble-Variational Data Assimilation System for HWRF: System Description and Experiments with. *Mon. Wea. Rev.*, **145**, 4877–4898.

Marks, F. G., and R. A. Houze, 1984: Airborne Doppler Radar Observations in Hurricane Debby. *Bull. Am. Meteorol. Soc.*, **65**, 569–582.

——, and ——, 1987: Inner Core Structure of Hurricane Alicia from Airborne Doppler Radar Observations. *J. Atmos. Sci.*, **44**, 1296–1317.

Montgomery, M. T., V. A. Vladimirov, and P. V Denissenko, 2002: An experimental study on hurricane mesovortices. *J. Fluid Mech*, **471**, 1–32.

——, M. E. Nicholls, T. a. Cram, and a. B. Saunders, 2006: A Vortical Hot Tower Route to Tropical Cyclogenesis. *J. Atmos. Sci.*, **63**, 355–386.

——, and R. K. Smith, 2014: Paradigms for tropical-cyclone intensification. *Aust. Meteor. Ocean. J.*, **64**, 37–66.

Nguyen, M. C., M. J. Reeder, N. E. Davidson, R. K. Smith, and M. T. Montgomery, 2011: Inner-core vacillation cycles during the intensification of Hurricane Katrina. *Q. J. R. Meteorol. Soc.*, **137**, 829–844.

Pan, Y., K. Zhu, M. Xue, X. Wang, M. Hu, S. G. Benjamin, S. S. Weygandt, and J. S. Whitaker, 2014: A GSI-Based Coupled EnSRF–En3DVar Hybrid Data Assimilation System for the Operational Rapid Refresh Model: Tests at a Reduced Resolution. *Mon. Wea. Rev.*, **142**, 3756–3780.

Persing, J., and M. T. Montgomery, 2003: Hurricane Superintensity. *J. Atmos. Sci.*, **60**, 2349–2371.

——, M. T. Montgomery, J. C. McWilliams, and R. K. Smith, 2013: Asymmetric and axisymmetric dynamics of tropical cyclones. *Atmos. Chem. Phys.*, **13**, 12299–12341.

Pielke, R. A., J. Gratz, C. W. Landsea, D. Collins, M. A. Saunders, and R. Musulin, 2008: Normalized Hurricane Damage in the United States: 1900-2005. *Nat. hazards Rev.*, 29–42.

Poterjoy, J., and F. Zhang, 2014a: Predictability and Genesis of Hurricane Karl (2010) Examined through the EnKF Assimilation of Field Observations Collected during PREDICT. *J. Atmos. Sci.*, **71**, 1260–1275.

——, and ——, 2014b: Intercomparison and Coupling of Ensemble and Four-Dimensional Variational Data Assimilation Methods for the Analysis and Forecasting of Hurricane Karl (2010). *Mon. Wea. Rev.*, **142**, 3347–3364.

——, ——, and Y. Weng, 2014: The Effects of Sampling Errors on the EnKF Assimilation of Inner-Core Hurricane Observations. *Mon. Wea. Rev.*, **142**, 1609–1630.

Powell, M. D., E. W. Uhlhorn, and J. D. Kepert, 2009: Estimating Maximum Surface Winds from Hurricane Reconnaissance Measurements. *Wea. Forecast.*, **24**, 868–883.

Pu, Z., and S. A. Braun, 2001: Evaluation of Bogus Vortex Techniques Using Four-Dimensional Variational Data Assimilation. *Mon. Wea. Rev.*, **129**, 2023–2039.

——, X. Li, and J. Sun, 2009: Impact of Airborne Doppler Radar Data Assimilation on the Numerical Simulation of Intensity Changes of Hurricane Dennis near a Landfall. *J. Atmos. Sci.*, **66**, 3351–3365.

——, S. Zhang, M. Tong, and V. Tallapragada, 2016: Influence of the Self-Consistent Regional Ensemble Background Error Covariance on Hurricane Inner-Core Data Assimilation with the GSI-Based Hybrid System for HWRF. *J. Atmos. Sci.*, **73**, 4911–4925.

Reasor, P. D., M. T. Montgomery, F. D. Marks, and J. F. Gamache, 2000: Low-Wavenumber Structure and Evolution of the Hurricane Inner Core Observed by Airborne Dual-Doppler Radar. *Mon. Wea. Rev.*, **128**, 1653–1680.

——, ——, and L. D. Grasso, 2004: A New Look at the Problem of Tropical Cyclones in Vertical Shear Flow: Vortex Resiliency. *J. Atmos. Sci.*, **61**, 3–22.

Rogers, R., and E. Uhlhorn, 2008a: Observations of the structure and evolution of surface and flight-level wind asymmetries in Hurricane Rita (2005). *Geophys. Res. Lett.*, **35**, 1–6.

——, and ——, 2008b: Observations of the structure and evolution of surface and flight-level wind asymmetries in Hurricane Rita (2005). *Geophys. Res. Lett.*, **35**, L22811.

——, and Coauthors, 2006: The intensity forecasting experiment: A NOAA multiyear field program for improving tropical cyclone intensity forecasts. *Bull. Am. Meteorol. Soc.*, **87**,

1523–1537.

——, and Coauthors, 2013a: NOAA'S hurricane intensity forecasting experiment: A progress report. *Bull. Am. Meteorol. Soc.*, **94**, 859–882.

——, P. Reasor, and S. Lorsolo, 2013b: Airborne Doppler Observations of the Inner-Core Structural Differences between Intensifying and Steady-State Tropical Cyclones. *Mon. Wea. Rev.*, **141**, 2970–2991.

——, P. D. Reasor, and J. a. Zhang, 2015: Multiscale Structure and Evolution of Hurricane Earl (2010) during Rapid Intensification. *Mon. Wea. Rev.*, **143**, 536–562.

Rotunno, R., and G. H. Bryan, 2012: Effects of Parameterized Diffusion on Simulated Hurricanes. *J. Atmos. Sci.*, **69**, 2284–2299.

Sang, N. Van, R. K. Smith, and M. T. Montgomery, 2008: Tropical-cyclone intensification and predictability in three dimensions. *Q. J. R. Meteorol. Soc.*, **134**, 563–582.

Schubert, W. H., and J. J. Hack, 1982: Inertial Stability and Tropical Cyclone Development. *J. Atmos. Sci.*, **39**, 1687–1697.

——, M. T. Montgomery, R. K. Taft, T. A. Guinn, S. R. Fulton, J. P. Kossin, and J. P. Edwards, 1999: Polygonal Eyewalls, Asymmetric Eye Contraction, and Potential Vorticity Mixing in Hurricanes. *J. Atmos. Sci.*, **56**, 1197–1223.

Schwartz, C. S., 2016: Improving large-domain convection-allowing forecasts with high-resolution analyses and ensemble data assimilation. *Mon. Wea. Rev.*, **144**, 1777-1803.

——, Z. Liu, X.-Y. Huang, Y.-H. Kuo, and C.-T. Fong, 2013: Comparing Limited-Area 3DVAR and Hybrid Variational-Ensemble Data Assimilation Methods for Typhoon Track Forecasts: Sensitivity to Outer Loops and Vortex Relocation. *Mon. Wea. Rev.*, **141**, 4350–4372.

——, ——, and ——, 2015: Sensitivity of Limited-Area Hybrid Variational-Ensemble Analyses and Forecasts to Ensemble Perturbation Resolution. *Mon. Wea. Rev.*, **143**, 3454–3477.

Schwarzkopf, M. D., and S. B. Fels, 1991: The simplified exchange method revisited: An accurate, rapid method for computation of infrared cooling rates and fluxes. *J. Geophys. Res.*, **96**, 9075–9096.

Smith, R. K., M. T. Montgomery, and S. Vogl, 2008: A critique of Emanuel's hurricane model and potential intensity theory. *Q. J. R. Meteorol. Soc.*, **134**, 1–11.

——, M. T. Montgomeryb, and N. Van Sang, 2009: Tropical cyclone spin-up revisited. *Q. J. R. Meteorol. Soc.*, **135**, 1321–1335.

Stern, D. P., and D. S. Nolan, 2011: On the Vertical Decay Rate of the Maximum Tangential Winds in Tropical Cyclones. *J. Atmos. Sci.*, **68**, 2073–2094.

——, J. R. Brisbois, and D. S. Nolan, 2014: An Expanded Dataset of Hurricane Eyewall Sizes and Slopes. *J. Atmos. Sci.*, **71**, 2747–2762.

——, J. D. Doyle, G. H. Bryan, and J. D. Jepert, 2017: Understanding Atypical Mid-Level Wind Speed Maxima in Hurricane Eyewalls. *97th American Meteorological Society Annual Meeting*. 2017 Jan 22-26, Seattle, WA.

Stewart, S. R., 2014: National Hurricane Center Tropical Cyclone Report: HURRICANE EDOUARD. Tropical Cyclone Rep. AL062014, National Hurricane Center, available online at https://www.nhc.noaa.gov/data/tcr/AL062014_Edouard.pdf. Accessed Oct. 3, 2019

Susca-Lopata, G., J. Zawislak, E. J. Zipser, and R. F. Rogers, 2015: The Role of Observed Environmental Conditions and Precipitation Evolution in the Rapid Intensification of Hurricane Earl (2010). *Mon. Wea. Rev.*, **143**, 2207–2223.

Tallapragada, V., and Coauthors, 2014: Hurricane Weather Research and Forecasting (HWRF) model: 2014 scientific documentation. Developmental Testbed Center, 1–81 pp. Available online at https://dtcenter.org/HurrWRF/users/docs/scientific_documents/HWRFv3.6a_ScientificDoc.pdf. Accessed Oct. 3, 2019.

——, and Coauthors, 2015: Hurricane Weather Research and Forecasting (HWRF) model: 2015 scientific documentation. Developmental Testbed Center, 1–81 pp. Available online at https://dtcenter.org/HurrWRF/users/docs/scientific_documents/HWRF_v3.7a_SD.pdf. Accessed Oct. 3, 2019.

Thu, T. Van, and T. N. Krishnamurti, 1992: Vortex Initialization for Typhoon Track Prediction. *Meteorol. Atmos. Phys.*, **47**, 117–126.

Tong, M., V. Tallapragada, E. Liu, W. Wang, C. Kieu, Q. Liu, and B. Zhan, 2014: Impact of Assimilating Aircraft Reconnaissance Observations in Operational HWRF. *2014 HFIP annual meeting*. 2014 Nov 18-20, Miami, FL.

——, and Coauthors, 2018: Impact of Assimilating Aircraft Reconnaissance Observations on Tropical Cyclone Initialization and Prediction using Operational HWRF and GSI Ensemble-Variational Hybrid Data Assimilation. *Mon. Wea. Rev*, **146**, 4155–4177,.

Torn, R. D., and G. J. Hakim, 2009a: Ensemble Data Assimilation Applied to RAINEX Observations of Hurricane Katrina (2005). *Mon. Wea. Rev.*, **137**, 2817–2829.

——, and G. J. Hakim, 2009b: Ensemble Data Assimilation Applied to RAINEX Observations of Hurricane Katrina (2005). *Mon. Wea. Rev.*, **137**, 2817–2829.

——, 2010: Performance of a Mesoscale Ensemble Kalman Filter (EnKF) during the NOAA High-Resolution Hurricane Test. *Mon. Wea. Rev.* , **138**, 4375–4392.

Trahan, S., and L. Sparling, 2012: An Analysis of NCEP Tropical Cyclone Vitals and Potential

Effects on Forecasting Models. *Wea. Forecast.*, **27**, 744–756.

Tuleya, R. E., 1994: Tropical storm development and decay: Sensitivity to surface boundary conditions. *Mon. Wea. Rev.*, **122**, 291–304.

Uhlhorn, E. W., and P. G. Black, 2003: Verification of Remotely Sensed Sea Surface Winds in Hurricanes. *J. Atmos. Ocean. Technol.*, **20**, 99–116.

——, ——, J. L. Franklin, M. Goodberlet, J. Carswell, and A. S. Goldstein, 2007: Hurricane Surface Wind Measurements from an Operational Stepped Frequency Microwave Radiometer. *Mon. Wea. Rev.*, **135**, 3070–3085.

Velden, C., W. E. Lewis, W. Bresky, D. Stettner, J. Daniels, and S. Wanzong, 2017: Assimilation of High-Resolution Satellite-Derived Atmospheric Motion Vectors: Impact on HWRF Forecasts of Tropical Cyclone Track and Intensity. *Mon. Wea. Rev.*, **145**, 1107–1125.

Vukicevic, T., P. Reasor, S. D. Aberson, and K. J. Sellwood, 2013: Joint Impact of Forecast Tendency and State Error Biases in Ensemble Kalman Filter Data Assimilation of Inner-Core Tropical Cyclone Observations. *Mon. Wea. Rev.*, **141**, 2992–3006.

Wang, X., 2010: Incorporating Ensemble Covariance in the Gridpoint Statistical Interpolation Variational Minimization: A Mathematical Framework. *Mon. Wea. Rev.*, **138**, 2990–2995.

——, and T. Lei, 2014: GSI-Based Four-Dimensional Ensemble–Variational (4DEnsVar) Data Assimilation: Formulation and Single-Resolution Experiments with Real Data for NCEP Global Forecast System. *Mon. Wea. Rev.*, **142**, 3303–3325.

——, D. M. Barker, C. Snyder, and T. M. Hamill, 2008: A Hybrid ETKF–3DVAR Data Assimilation Scheme for the WRF Model. Part II: Real Observation Experiments. *Mon. Wea. Rev.*, **136**, 5132–5147.

——, D. Parrish, D. Kleist, and J. Whitaker, 2013: GSI 3DVar-Based Ensemble–Variational Hybrid Data Assimilation for NCEP Global Forecast System: Single-Resolution Experiments. *Mon. Wea. Rev.*, **141**, 4098–4117.

Wang, Y., and Coauthors, 2011: The Central European limited-area ensemble forecasting system: ALADIN-LAEF. *Q. J. R. Meteorol. Soc.*, **137**, 483–502.

Weng, Y., and F. Zhang, 2012: Assimilating Airborne Doppler Radar Observations with an Ensemble Kalman Filter for Convection-Permitting Hurricane Initialization and Prediction: Katrina (2005). *Mon. Wea. Rev.*, **140**, 841–859.

Whitaker, J. S., and T. M. Hamill, 2002: Ensemble Data Assimilation without Perturbed Observations. *Mon. Wea. Rev.*, **136**, 463-482.

——, and ——, 2012: Evaluating Methods to Account for System Errors in Ensemble Data Assimilation. *Mon. Wea. Rev.*, **140**, 3078–3089.

Willoughby, H. E., and M. B. Chelmow, 1982: Objective Determination of Hurricane Tracks from Aircraft Observations. *Mon. Wea. Rev.*, **110**, 1298–1305.

——, and M. E. Rahn, 2004: Parametric Representation of the Primary Hurricane Vortex. Part I: Observations and Evaluation of the Holland (1980) Model. *Mon. Wea. Rev.*, **132**, 3033–3048.

Willoughby, H. E., H.-L. Jin, S. J. Lord, and J. M. Piotrowicz, 1984: Hurricane Structure and Evolution as Simulated by an Axisymmetric, Nonhydrostatic Numerical Model. *J. Atmos. Sci.*, **41**, 1169–1186.

Wu, T.-C., H. Liu, S. J. Majumdar, C. S. Velden, and J. L. Anderson, 2014: Influence of Assimilating Satellite-Derived Atmospheric Motion Vector Observations on Numerical Analyses and Forecasts of Tropical Cyclone Track and Intensity. *Mon. Wea. Rev.*, **142**, 49–71.

——, C. S. Velden, S. J. Majumdar, H. Liu, and J. L. Anderson, 2015: Understanding the Influence of Assimilating Subsets of Enhanced Atmospheric Motion Vectors on Numerical Analyses and Forecasts of Tropical Cyclone Track and Intensity with an Ensemble Kalman Filter. *Mon. Wea. Rev.*, **143**, 2506–2530.

——, M. Zupanski, L. D. Grasso, C. D. Kummerow, and S.-A. Boukabara, 2019: All-Sky Radiance Assimilation of ATMS in HWRF: A Demonstration Study. *Mon. Wea. Rev.*, **147**, 85–106.

Xiao, Q., X. Zhang, C. Davis, J. Tuttle, G. Holland, and P. J. Fitzpatrick, 2009: Experiments of Hurricane Initialization with Airborne Doppler Radar Data for the Advanced Research Hurricane WRF (AHW) Model. *Mon. Wea. Rev.*, **137**, 2758–2777.

Yang, C., Z. Liu, J. Bresch, S. R. H. Rizvi, X.-Y. Huang, and J. Min, 2016: AMSR2 all-sky radiance assimilation and its impact on the analysis and forecast of Hurricane Sandy with a limited-area data assimilation system. *Tellus A*, **68**, 1–19.

Yang, S.-C., K.-J. Lin, T. Miyoshi, and E. Kalnay, 2013: Improving the spin-up of regional EnKF for typhoon assimilation and forecasting with Typhoon Sinlaku (2008). *Tellus A*, **65**, 1–21.

Zhang, F., and Y. Weng, 2015: Predicting Hurricane Intensity and Associated Hazards: A Five-Year Real-Time Forecast Experiment with Assimilation of Airborne Doppler Radar Observations. *Bull. Am. Meteorol. Soc.*, **96**, 25–33.

——, ——, J. a. Sippel, Z. Meng, and C. H. Bishop, 2009a: Cloud-Resolving Hurricane Initialization and Prediction through Assimilation of Doppler Radar Observations with an Ensemble Kalman Filter. *Mon. Wea. Rev.*, **137**, 2105–2125.

——, ——, J. A. Sippel, Z. Meng, and C. H. Bishop, 2009b: Cloud-Resolving Hurricane Initialization and Prediction through Assimilation of Doppler Radar Observations with an Ensemble Kalman Filter. *Mon. Wea. Rev.*, **137**, 2105–2125.

——, ——, J. F. Gamache, and F. D. Marks, 2011: Performance of convection-permitting hurricane initialization and prediction during 2008-2010 with ensemble data assimilation of inner-core airborne Doppler radar observations. *Geophys. Res. Lett.*, **38**, 2–7.

——, M. Minamide, and E. E. Clothiaux, 2016: Potential impacts of assimilating all-sky infrared satellite radiances from GOES-R on convection-permitting analysis and prediction of tropical cyclones. *Geophys. Res. Lett.*, **43**, 2954–2963.

Zhang, J. A., and M. T. Montgomery, 2012: Observational Estimates of the Horizontal Eddy Diffusivity and Mixing Length in the Low-Level Region of Intense Hurricanes. *J. Atmos. Sci.*, **69**, 1306–1316.

——, D. S. Nolan, R. F. Rogers, and V. Tallapragada, 2015: Evaluating the impact of improvements in the boundary layer parameterization on hurricane intensity and structure forecasts in HWRF. *Mon. Wea. Rev.*, **143**, 3136–3155.

——, and F. D. Marks, 2015: Effects of Horizontal Diffusion on Tropical Cyclone Intensity Change and Structure in Idealized Three-Dimensional Numerical Simulations. *Mon. Wea. Rev.*, **143**, 3981–3995.

Zhou, C., H. Shao, and L. Bernardet, 2015a: Applications of the GSI-Hybrid Data Assimilation for High-Resolution Tropical Storm Forecasts: tackling the intensity spin--down issue in 2014 HWRF. *16th WRF users Workshop*, 2016 Jun 27 - Jul 1, Boulder, CO.

——, H. Shao, L. R. Bernardet, M. Tong, and V. Tallapragada, 2015b: Regional Applications of the GSI-Hybrid Data Assimilation for High-Resolution Tropical Storm Forecasts (95th American Meteorological Society Annual Meeting). *95th AMS Annual Meeting*, 2015 Jan 4-8, Phoenix, AZ.

Zhu, P., K. Menelaou, and Z. Zhu, 2014: Impact of subgrid-scale vertical turbulent mixing on eyewall asymmetric structures and mesovortices of hurricanes. *Q. J. R. Meteorol. Soc.*, **140**, 416–438.

——, B. Tyner, J. A. Zhang, E. Aligo, S. Gopalakrishnan, and D. Frank, 2018: Role of eyewall and rainband eddy forcing in tropical cyclone intensification. *Atmos. Chem. Phys. Discuss.*, 1–33.

Zhu, T., D. L. Zhang, and F. H. Weng, 2004: Numerical simulation of Hurricane Bonnie (1998). Part I: Eyewall evolution and intensity changes. *Mon. Wea. Rev.*, **132**, 225–241.

Zhu, Y., and Coauthors, 2016b: All-Sky Microwave Radiance Assimilation in NCEP's GSI Analysis System. *Mon. Wea. Rev.*, **144**, 4709–4735.